ANTENNA ARRAY DESIGNS FOR DIRECTIONAL WIRELESS COMMUNICATOIN NETWORKS

A DISSERTATION SUBMITTED TO THE GRADUATE DIVISION OF THE
UNIVERSITY OF HAWAIʻI AT MĀNOA IN PARTIAL FULFILLMENT OF THE
REQUIREMENTS FOR THE DEGREE OF

DOCTOR OF PHILOSOPHY

IN

ELECTRICAL ENGINEERING

MAY 2018

By

Gui Chao Huang

Dissertation Committee:

Dr. Magdy F. Iskander, Chairperson
Dr. Zhengqing Yun
Dr. Galen Sasaki
Dr. Yuanzhang Xiao
Dr. Marcelo H. Kobayashi

Acknowledgments

I would like to thank Dr. Magdy Iskander for giving me the opportunity to obtain my Ph.D. and for all the support, encouragement and guidance. Dr. Iskander introduced me to the world of electromagnetic, without him, I would never go this far. I would also like to thank Dr. Zhengqing Yun for his support and guidance at HCAC.

I would also like to thank Ruthsenne Perron, Darcy Bibb, Asutosh Das, Scott Clemens and all that I failed to mention for the help and fun we had in the HCAC labs. Finally, I would like to thank my family for the support and encouragement.

Abstract

Forty percent of people living in rural areas do not have broadband Internet access. Availability of affordable broadband access to the Internet would have a significant impact on enabling the economic development in these areas and in providing improved quality of life. However, large-scale deployment of broadband wireless technologies hinges on the development of reliable, low cost, and energy efficient networking solutions. To overcome wireless networking challenges in rural areas, a novel advanced directional networking technology has been proposed. The approach is based on enhancing intelligence and logic capabilities in the physical layer in the OSI Model and without causing changes in the other layers of the communication networking model. A critical component in implementing the proposed system is the development of a low-cost and low-profile circularly polarized antenna array with beam-switching/beam-steering capabilities. In this dissertation, a broadband long-slot antenna array fed by simplified microstrip structures was designed, fabricated and a prototype was tested in the HCAC indoor antenna range. For system components requiring extremely low-profile antenna installations, a narrower-band high-gain stacked patch antenna array with annular gap was also developed. Both antenna arrays were tested for beam-steering capabilities using a new design of a broadband microstrip-based 8×8 Butler matrix with compact crossovers. The antenna arrays and the Butler matrix were fabricated and experimentally characterized. Simulation results were verified with measured data. The long-slot antenna array has 40% bandwidth with an average gain of 17 dBic and an axial ratio of < 1.8 dB. The stacked patch antenna array has 16.7% bandwidth with an average gain of 23 dBic and an axial ratio of < 1.6 dB. Stable radiation patterns and a scanning range of ±30° were obtained when the antenna arrays were fed by the Butler matrix.

Table of Contents

List of Tables

List of Figures

CHAPTER 1

INTRODUCTION

1.1 Background and Current Technology

The establishment of a cost-effective, reliable, and broadband wireless communication system in rural areas remains a significant technology challenge that requires a fresh look and innovative solutions. The vast coverage areas, rough terrain, and low user density in these areas often prohibit a cost-effective implementation of a standard wireless network system based on available technologies. The U.S. has tremendous wireless coverage from a variety of carriers, but the Federal Communications Commission in its 2015 report acknowledged that 55 million Americans – 17 percent of the population – lack access to an advanced broadband network. Moreover, a significant digital divide remains between urban and rural America: Over half of all rural Americans lack access to broadband service [1]. This has a negative impact on the inhabitants of rural communities and hinders economic developments in these areas. Affordable wireless communication and connectivity technology will have significant educational, health care and economic development impact on rural communities in the US and throughout the world.

Current technologies for internet access are available in two basic forms, wired and wireless connections. In wired connection, several technologies have been developed, such as, DSL, cable internet and fiber optic internet. In wireless connection, satellite and cellular network are the commonly used technologies that support large area coverage and long distant communication. In wired internet connection, a wire or cable needs to be deployed to connect the access point to the internet. DSL and cable internet services are widely available in urban areas, however, the deployment of wired internet connection in rural area is relatively difficult due to the vast area and low user density which dramatically increased the cost of the network infrastructure deployment.

When cable or DSL is not an option, satellite internet is one of the top options in rural areas as satellite internet coverage is available for most part of the U.S. In satellite internet, direct line of sight is required, which the dish antenna on the ground needs to point to the direction of the satellite that it is going to communicate with and there should be no obstacle in between the communication path. Heavy rain or snow can interfere the satellite communication channel, which can result in reduction in internet speed or loss of internet connection. The long distance between the dish antenna on the ground and the satellite, typically twenty thousand miles, also introduces latency in the communication channel, which typically about 700 ms. This latency is relatively large when compared to other forms of Internet access and it is large enough to affect some internet applications that require small latency, such as real-time online gaming. Due to the large latency, majority of real-time, multi-player games are not playable on any satellite Internet service. In addition, the cost of satellite internet is higher than the DSL and cable internet.

The other option for internet access is cellular network. Current 4G technology allows mobile users have broadband internet access in the cellular network [2]. In cellular network, the network is composed of a number of circular or hexagonal cells (base station coverage area), with the adjacent cells slightly overlapping with each other, to cover large area. Each cell is served by a wireless base station and the base station is connected to the core network through a wired or wireless backhaul. The radius of the cell is usually determined based on the user density and typically within the range of couple miles [2], [3]. In order to provide the wireless coverage, omnidirectional antenna is often used in the base station for omnidirectional coverage. Some base stations use multiple sectorial directional antennas (higher gain) to form an omnidirectional coverage to increase the range and coverage area. An example of a base station setup using sector antennas is shown in Figure 1.1. The omnidirectional coverage is beneficial in urban environment, as the high user density often require always on coverage in all the areas. On the other hand, in the rural area, most of the energy will be wasted in omnidirectional coverage due to low user density. With limited coverage range, low user density as well as the challenging terrain and the deployment cost, majority of the rural areas do not have cellular network coverage.

Figure 1.1. Cellular network base station with sector antennas [4].

1.2 Directional Networking and Earlier Approaches

Directional networking provides advantages including extended range, increased capacity, less susceptible to interference, and better power efficiency compare to communication networks using Omni-directional antennas [5]. Directional networking is also suitable to be used in environments with low user density. Therefore, directional networking is a good candidate to overcome the challenges in communication networks for rural areas. New challenges, however, are introduced in directional networking, when true energy efficient directional channels are used, rather than a routine implementation of omnidirectional approach using multiple sectoral and simultaneously radiating arrays [6]. These challenges include the deafness problem and tracking of mobile users. The deafness problem occurs when the directional node is pointing its beam toward the existing users and unaware of any user outside the coverage angle of the directional beam which wants to establish communication.

Serval researches have been proposed to address the deafness problem. However, they all focus on modifying the mac layer of the communication protocols, which can be complicated and not compatible with the existing communication protocols [7], [8], [9]. In [10], a research is proposed with changes only to the physical layer. In this research, the directional node consists of multiple sectors which equip with beam-switching antennas, a master controller is implemented in each node to determine and control the beam direction of the antenna in each sector based on the link-state information and geo-location information of remote nodes received by the sectors. This approach has successfully demonstrated the directional node to node connection. However, it is relied on sharing link-state information and geo-location information of the nodes in the network, such that the master controller in each node has the same overall picture of the network, so that the algorithm implemented in the master controllers can come up with the same network typology and control the beam direction accordingly. Thus, the research in [10] is not suitable for large number of nodes or users as a larger network require more computational resources. Moreover, it is more focus on the point to point connection between the nodes and hasn't take point to multipoint architecture into account.

1.3 Proposed Directional Networking

To overcome these challenges and fully realize the advantages of directional networking, an advanced directional networking technology is being developed by our group [6], [11]. The directional networking system is comprised of interconnected Advanced Nodes which are equipped with enhanced hardware, three sets of antenna arrays, propagation modeling, and digital signal processing (DSP) and network logic capabilities to achieve a physical-layer-based implementation (no changes to MAC and upper Open Systems Interconnection (OSI) layers) while providing a vaster coverage area than omnidirectional nodes. Figure 1.2 shows the overview of the proposed technology. The geographical coverage of the advance node is divided into six sectors. The antenna arrays equipped in the advanced node are for user discovery and communications between the users and the advanced node, as well as node to node connectivity. Geospatial resources-based propagation modeling will be used to determine the optimal number and location placement of the advanced nodes. The DSP and network logic capabilities are responsible for user tracking, antenna array beam direction controlling, and network connectivity, such as, mobile user handover.

Figure 1.3 shows the overview of the antenna arrays for the proposed advanced node. The advanced node has three types of antenna arrays for scanning, communication, and node-to-node connection. The advance node uses the scanning array for user discovery. Once a new user is discovered, based on the angle of arrival information from the scanning array, the advanced node beamform and adjust the radiation pattern of the communication array such that is can cover the new user and establish communication channel with the new user, as well as keep the coverage and communication channels for the existing users. The node-to-node array is used to provide point-to-point connections between advanced nodes as well as to the core network.

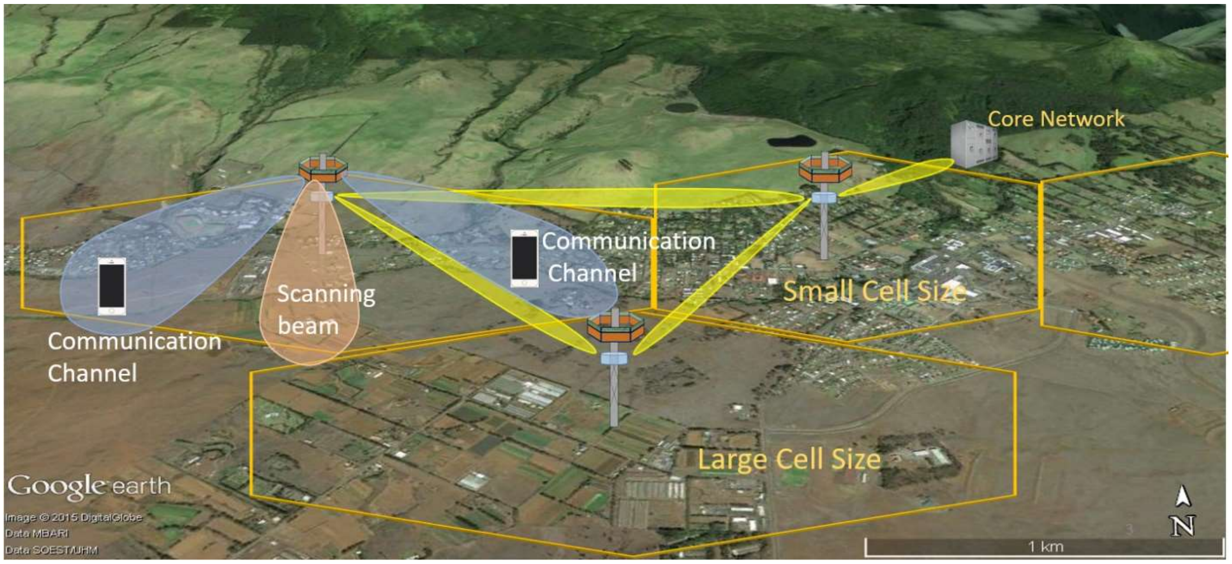

Figure 1.2. Overview of the proposed technology.

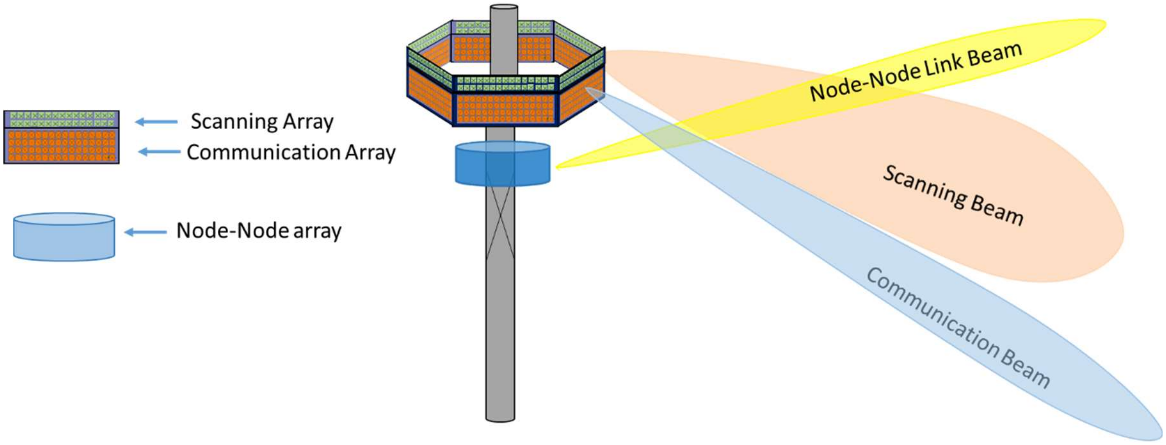

Figure 1.3. Overview of the Antenna Arrays for proposed Advanced Nodes.

This set of antenna arrays, thus, enables the advanced nodes to discover new users, communicate with connected users and maintain node-node and node-core network connectivity, all while achieving a vaster coverage area than traditional wireless base stations with omnidirectional antennas. To ensure that full-directionality is achieved, algorithms and procedures are developed that enhances logic capability and intelligence to the Physical Layer and help achieve cost effective directional networking approach that does not require complex and expensive changes in upper layer of the OSI communication models. Specifically, all the required modifications are carefully chosen to conform to the MAC layer standards of the radio used and hence, are restricted only to the Physical Layer of the OSI layer stack as illustrated in Figure 1.4.

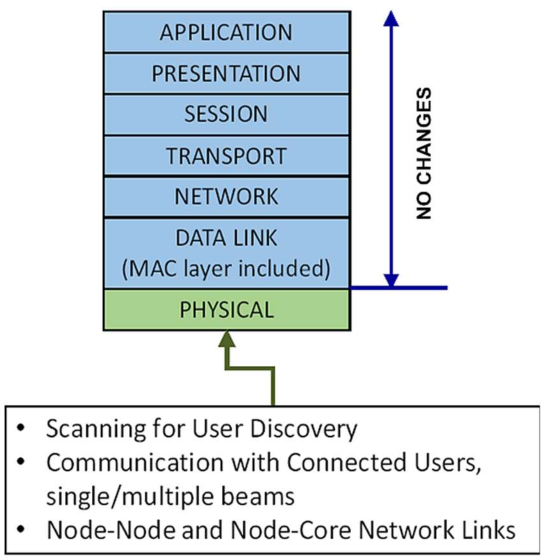

Figure 1.4. Physical-layer-based implementation.

To examine the feasibility of developing such a system, its overall performance was simulated using Matlab's WLAN Systems Toolbox for waveform generation, demodulation and analyses [6]. Simulations were performed to test the ability of advanced nodes to discover and communicate with users and analyze the performance and coverage. Eight-element scanning and communication antenna arrays were used on a communication network setup that included mobile users that communicate with the node using the WiFi standard IEEE 802.11 ac. The waveforms were designed using the Matlab's WLAN Systems toolbox occupying 80 MHz bandwidth, centered at 5.25 GHz. Figure 1.5 shows sample simulation result illustrating the multi-beam capability of the advanced nodes as a single mobile user in *sector 1* is tracked within the sector. In Figure 1.6, sector-to-sector handover is illustrated as the user moves from *sector 2* to *sector 1*.

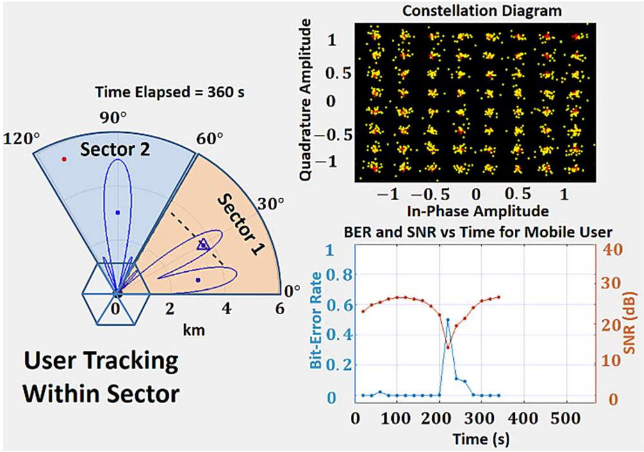

Figure 1.5. Simulation result based on IEEE 802.11 ac of the proposed system for user tracking.

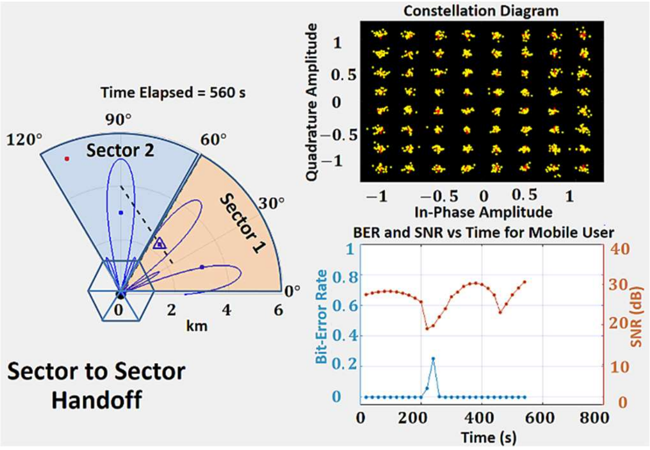

Figure 1.6. Simulation result based on IEEE 802.11 ac of the proposed system for sector-sector handover.

In realizing this new technology, antenna arrays and feeding network were developed. The main focus of this dissertation is on the development of low-cost, low-profile, broadband, high-gain and circularly polarized antenna arrays, as well as a low-cost feed system that enables beam-steering or beam-switching capabilities. Furthermore, alternative antenna designs were simulated, and some of these designs were prototyped and experimentally tested. The remaining sections of this dissertation are focused on the antenna array designs, prototyping and testing.

CHAPTER 2

ANTENNA ARRAY DESIGN

In antenna design, there are several parameters are used for quantifying and evaluating the performance and radiation characteristics of an antenna. At the beginning of this chapter, the important antenna parameters will be covered. Then, the rest of this chapter will be on the antenna array designs for directional networking application.

2.1 Antenna Parameters

2.1.1 Radiation Pattern

According to IEEE standard [12], an antenna radiation pattern is defined as “the spatial distribution of a quantity that characterizes the electromagnetic field generated by an antenna. The distribution can be expressed as a mathematical function or as a graphical representation. The quantities that are most often used to characterize the radiation from an antenna are proportional to, or equal to, power flux density, radiation intensity, directivity, phase, polarization, and field strength. In most cases, the radiation pattern is determined in the far-field region and is represented as a function of the directional coordinates.” The spatial distribution of radiated energy over a polar or spherical coordinate system is the most commonly used radiation pattern representation. Figure 2.1 shows an example of an antenna radiation pattern on spherical coordinate system.

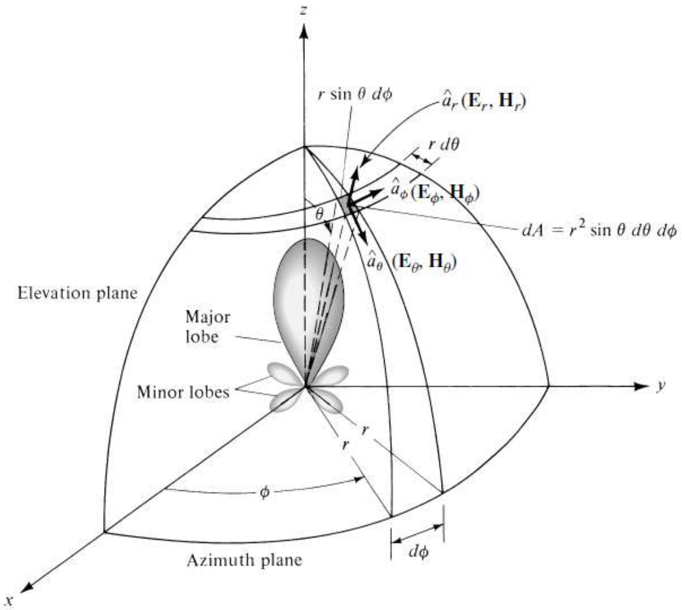

Figure 2.1. Radiation pattern on spherical system [13].

2.1.2 Half Power Beamwidth

Beamwidth is a parameter associate with radiation pattern of an antenna. In radiation pattern of an antenna, the main lobe is the main beam of the antenna where maximum energy is radiated by the antenna. Half Power Beamwidth is defined as the angular separation, in which the magnitude of the radiation intensity decreases by 50% (or 3dB) from the peak of the main beam. The other important beamwidth parameter is the First Null Beam Width, it is defined as the angular separation between the first pattern nulls adjacent to the main beam. Figure 2.2 shows an example of half power beam and first null beam of a 2-D radiation pattern on linear scale.

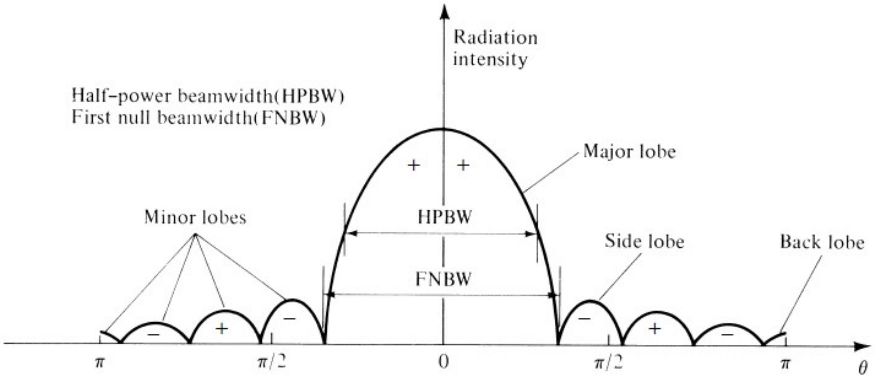

Figure 2.2. Example of half power beam and first null beam of a radiation pattern on linear scale [13].

2.1.3 Gain

Antenna gain is another useful parameter describing the performance of an antenna. It is defined as "the ratio of the intensity, in a given direction, to the radiation intensity that would be obtained if the power accepted by the antenna were radiated isotropically. The radiation intensity corresponding to the isotropically radiated power is equal to the power accepted by the antenna divided by 4π." In most case, relative gain is used, which is the ratio of the gain of an antenna in a given direction to the gain of a reference antenna. Hypothetical lossless isotropic antenna is commonly used as reference antenna. Usually this ratio is expressed in decibel scale and use "decibels-isotropic" (dBi) as unit. Other antennas, whose gain can be easily calculated or it is known, also can be used as reference antenna. When the direction is not stated, antenna gain usually refers to the maximum gain of the antenna in free space [12].

2.1.4 Polarization

Polarization of an antenna in a given direction is defined in [12] as "the polarization of the wave transmitted (radiated) by the antenna." Polarization of a radiated wave can be linear, circular or elliptical. Figure 2.3 shows the examples of linearly polarized, circularly polarized and elliptically polarized electromagnetic wave propagate in the +z direction. Linear and circular polarizations are special cases of elliptical polarization. In elliptical polarization, the electric-field vector rotates as a function of time and form a polarization ellipse on a fixed plane normal to the direction of propagation as shown in Figure 2.4. The electric-field vector rotates either clockwise or counterclockwise, depends of the direction of propagation, the electromagnetic wave can be classified as right-hand polarized or left-hand polarized. For the example in Figure 2.4, if the electric-field vector rotates counterclockwise and the wave is propagating in the +z direction, the wave is right-hand polarized. Likewise, if the electric-field vector rotates clockwise and the wave is propagating in the +z direction, the wave is left-hand polarized.

The ratio of the major axis to the minor axis of the polarization ellipse is called axial ratio as shown in Figure 2.4. In linear polarization, the axial ratio is equal to ∞, as the minor axis of the polarization ellipse is zero. In circular polarization, the axial ratio is equal to 1 (or 0 dB), as the major and minor axes of the polarization ellipse are equal. In antenna design, it is difficult to achieve perfect circular polarization (or axial ratio equal to 0 dB), thus an antenna is usually said to be circularly polarized if the axial ratio is less than 3 dB.

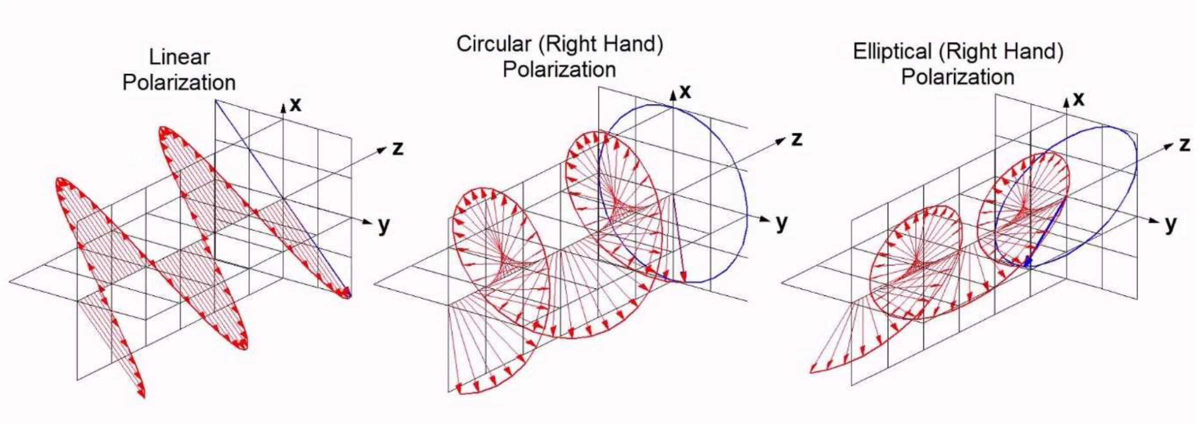

Figure 2.3. Examples of linearly polarized, circularly polarized and elliptically polarized electromagnetic wave propagate in the +z direction [14].

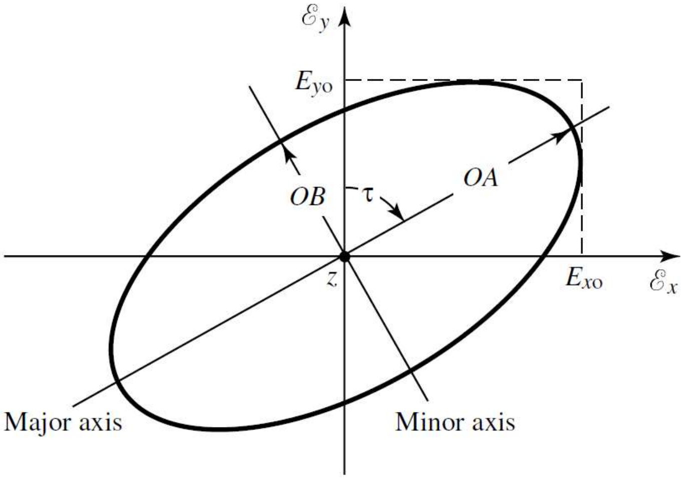

Figure 2.4. Rotation of electromagnetic wave and its polarization ellipse at z = 0 as a function of time [13].

In antenna design, co-polarization represents the polarization the antenna is intended to radiate. Cross-polarization represents the polarization orthogonal to the co-polarization. Cross polarization level measures the polarization purity of an antenna. It is the ratio of the maximum radiation intensity of the co-polarization and cross-polarizations. Polarization of antenna is an important factor in wireless communication. If the polarization of the transmitting and receiving antennas is matched, maximum power transmission between the two antenna occurs. If the polarization of the transmitting and receiving antennas is mismatched, there will be additional losses in power transmission between the two antennas or the receiving antenna will not receive any power from the transmitting antenna. For example, if the polarization of the transmitting and receiving antennas is orthogonal to each other (i.e. vertically polarized to horizontally polarized or right hand circularly polarized to left hand circularly polarized), depends on the cross polarization level of the antennas, the power received by the receiving antenna can be 20 dB (or more) lower than the case of both antennas with match polarization.

In wireless communication, multipath fading occurs when the direct-path signal is interfered by the reflected signals from the environment (such as reflections from building, hills, ground, water, etc). Depends on the phase of the signals, the interference can be constructive or destructive. Destructive interference can cause the signal to be faded out. Circularly polarized antennas can help to mitigate the multipath fading effect, as the circularly polarized signal changes its rotating direction when reflected from an object. In modern wireless communication applications, linear polarized antennas are widely used due to simplicity and low cost. Circularly polarized antennas are commonly used in satellite communications, due to their ability to mitigate the multipath effects and provide additional freedom to the orientation angle of the transmitting and receiving antennas.

2.1.5 Input Impedance

Input impedance of an antenna is the impedance presented by an antenna at its terminals. Input impedance of an antenna is usually a complex number, the real part represents the radiation and loss resistance of the antenna and the imaginary part represents the reactance of the antenna. In antenna designing, one of the goal is to design the antenna with an input impedance match to the characteristic impedance of the transmission line it is going to connect to. Most radio frequency (RF) circuits have a characteristic impedance of 50 Ω, some like TV cables have characteristic impedance of 75 Ω. When the input impedance of an antenna is not match with the characteristic impedance of the RF circuit, some of the power deliver to the antenna terminal will be reflected. The reflection coefficient ($\Gamma\ or\ S_{11}$) is calculated as:

$$\Gamma = \frac{Z_A - Z_0}{Z_A + Z_0} \tag{2.1}$$

where Z_A is the input impedance of the antenna and Z_0 is the characteristic impedance of the transmission line connecting to the antenna. The magnitude square of the reflection coefficient, $|\Gamma|^2$, represents the ratio of the reflected power to the power incident at the antenna terminal. In general, an antenna is said to have good impedance matching if the reflection coefficient is less than -10 dB at its operating frequency.

In antenna design, it is preferred to design an antenna with good impedance matching. However, in certain condition, a matching circuit is needed to match the input impedance of an antenna to the characteristic impedance of the RF circuit. Especially in electrically small antenna design, as electrically small antennas tend to have high reactance. In designing a matching circuit, lumped elements (capacitors and inductors) and open- and short-circuit stubs are commonly used.

2.1.6 Bandwidth

The radiation characteristics of an antenna can change significantly at different frequencies. The bandwidth of an antenna is defined as “the range of frequencies within which the performance of the antenna, with respect to some characteristic, conforms to a specified standard.” The characteristic can be input impedance, gain, polarization, etc. For broadband antennas, the bandwidth is usually expressed as the ratio of the upper frequency to the lower frequency of acceptable performance. A bandwidth of 2:1 indicates the upper frequency is equal to twice of the lower frequency. For narrowband antennas, the bandwidth is often expressed in percentage of the ratio of the frequency difference (upper frequency minus lower frequency) to the center frequency.

2.2 Antenna Array Designs for Directional Networking

There are wide variety of antennas, depend on the geometry and structure of the antennas, their radiation characteristics can be very different from each other. Based on the structure and radiation characteristics of the antennas, certain types of antennas are more suitable for certain applications. In wireless communication, the most commonly used antennas are dipole, monopole, Yagi-Uda and horn antennas, because of their design simplicity, favorable radiation characteristics, and easy to fabricate. Figure 2.5 and Figure 2.6 illustrate the structure and radiation patterns of an inductively-loaded monopole antenna and a horn antenna. As shown in the figure, the monopole antenna has an omni-directional radiation. Due to its omni-directional coverage, monopole antennas are widely used in communication networks support mobile devices, such as Wi-Fi, cellular network and radio network. On the other hand, the radiation pattern of horn antennas is highly directional. Due to its high directive radiation pattern, horn antennas are widely used as a feed element for dish antennas.

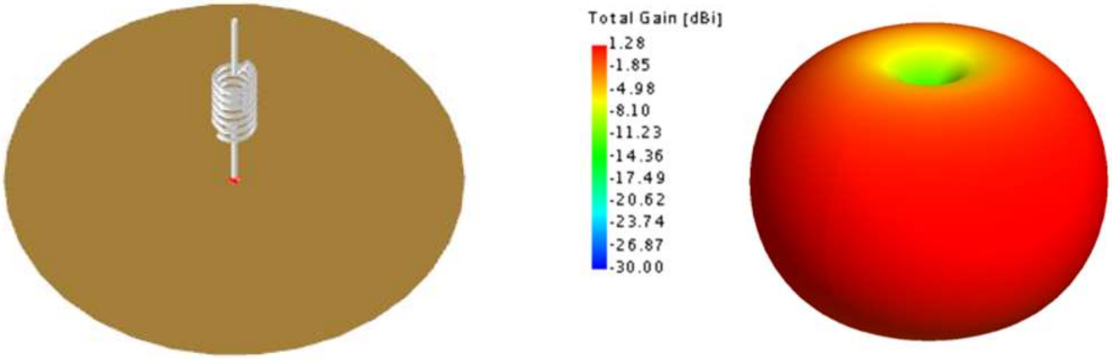

Figure 2.5. Example of an inductively-loaded monopole antenna and its radiation pattern [15].

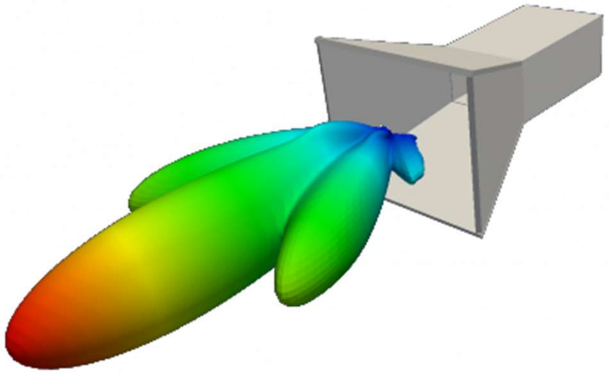

Figure 2.6. Example of a horn antenna and its radiation pattern [16].

For directional networking application, the desired requirements of the antenna array are low-cost, low-profile, broadband, circularly polarized, high-gain and with beam-steering capability. The broadband property allows the system to support faster data rate and more channels. As the multipath fading effect could significantly affect the accuracy of the mobile user tracking schemes [5], the implementation of circularly polarized antenna array can help mitigate the multipath fading effect and provide stable signal level over long distance. Furthermore, beam-steering capability allows the antenna array to steer the main beam direction without physically moving/reorienting the antenna array.

Circularly polarized antenna arrays have been widely investigated, due to their attractive properties, such as lessened multipath fading effect and insensitivity to transmitter and receiver orientations. However, majority of the published works on circularly polarized antenna array either have less than 30% bandwidth or lack of a feeding network to support beam-steering (only focus on the broadside radiation characteristics) [17]–[23]. For example, the circularly polarized patch antenna design [21] shown in Figure 2.7 has a peak gain of 18 dBic and a 3-dB gain bandwidth of 14.6%. However, the antenna array design only focuses on the radiation pattern in the broadside direction and does not support beam-steering. Wideband antennas, such as Vivaldi or Spiral antennas, either have large size or require a broadband balun and impedance transformer [24]–[27]. Figure 2.8a illustrates a dual-polarized Vivaldi array, which has a bandwidth of 9:1 and a thickness of 3.5λ_c (λ_c is the free-space wavelength at the center frequency). Figure 2.8b shows a circularly polarized spiral antenna connected to a wideband balun.

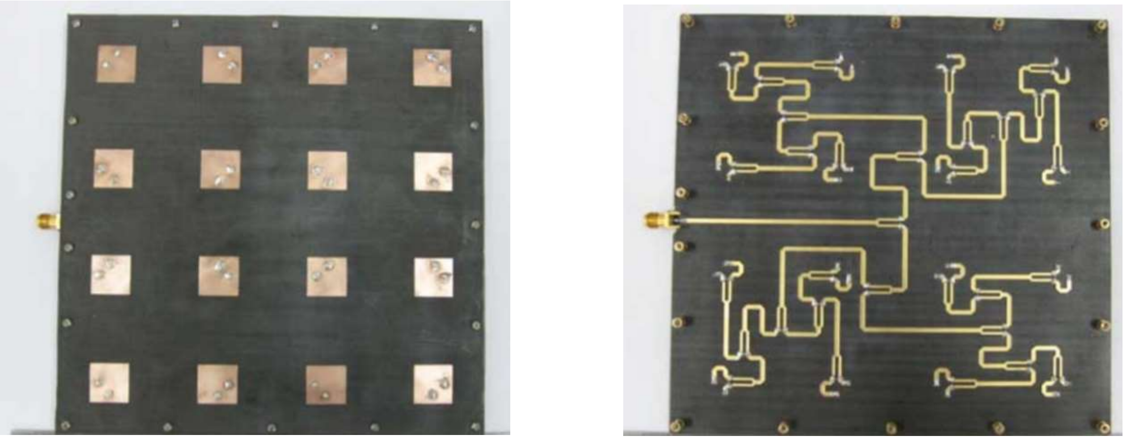

(a) (b)

Figure 2.7. Circularly polarized patch antenna array in [21] only focus on designing the antenna array with the main beam in the broadside direction. (a) Top view. (b) Back view.

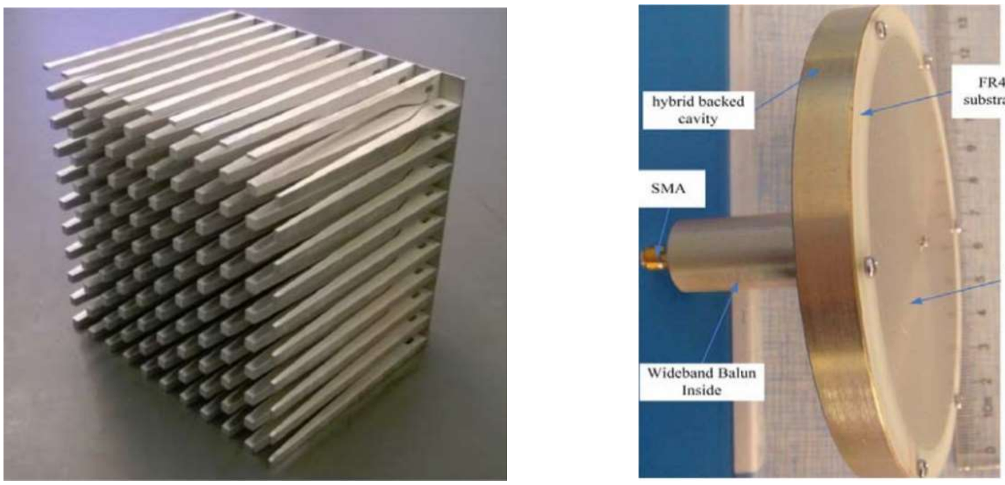

(a) (b)

Figure 2.8. (a) A dual-polarized 10×10 Vivaldi array [25]. (b) A spiral antenna with wideband balun [26].

Previously, a broadband cylindrical long slot antenna (CLSA) array with dual polarization property had been developed by our group [28], [29]. Long slot antenna array is relatively low profile compare to other wideband antenna structures and it also had been shown that the CLSA array has the capability of beam forming [30]. Thus, a dual-polarized-antenna array based on the long-slot-array concept was proposed to cover the frequency range of 4–6 GHz for directional networking application. For systems that require extremely low-profile antenna installation, two dual-fed stacked patch antenna arrays were also developed with the compromise of the wide bandwidth while providing comparable performance in circularly polarized radiation characteristics as well as improvements in beamforming and steering characteristic. The radiation characteristics of the arrays were examined and compared in terms of bandwidth, beamwidth, gain, axial ratio and beam direction. The operating frequencies of the antenna arrays and feed system were specified by the sponsor, Communications-Electronics Research, Development and Engineering Center (CERDEC).

2.2.1 Long Slot Antenna Array

The long-slot-antenna (LSA) array was originally designed by Raytheon. It is an ultra-wideband linearly polarized structure with input impedance ranging from 150 to 337 Ω [29], [31], [32]. For the LSA array to be broadband, the feeding port distance needs to be less than or equal to half of the free-space wavelength at the highest operating frequency [32]. Figure 2.9a shows a schematic of a 2-D linearly polarized LSA array. The schematic of the LSA array has three slots and the feeding port distance is labeled as d_x and d_y in the schematic. A prototype of the linearly polarized LSA array with ferrite loaded ground is shown in Figure 2.9b, which has an operating frequency of 200–2000 MHz.

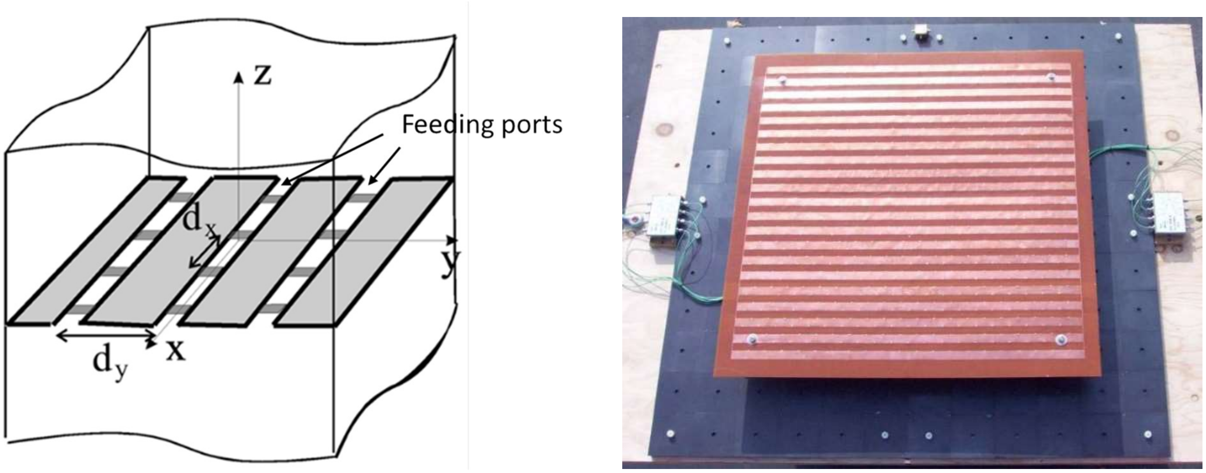

(a) (b)

Figure 2.9. (a) Schematic of a linearly polarized long slot antenna array [32]. (b) Prototype of a long slot antenna array with ferrite loaded ground plane [33].

As it may be seen in Figure 2.9, the LSA array is a linearly polarized structure. To support dual polarization and circular polarization, additional orthogonal slots are proposed between the feeding ports while keeping the feeding port spacing less than or equal to half of the free-space wavelength at the highest operating frequency. Due to the structure of the LSA array, the radiation pattern is bidirectional. To achieve unidirectional radiation, a ground plane is placed a quarter-wave apart from the antenna array. Figure 2.10 shows a proposed dual-polarized 4×4 LSA array with a ground plane in the back of the antenna array, where the vertical slots and horizontal slots are responsible for radiating the horizontally polarized and vertically polarized electric fields, respectively. The vertical slots and horizontal slots can be excited 90° out of phase to achieve circular polarization.

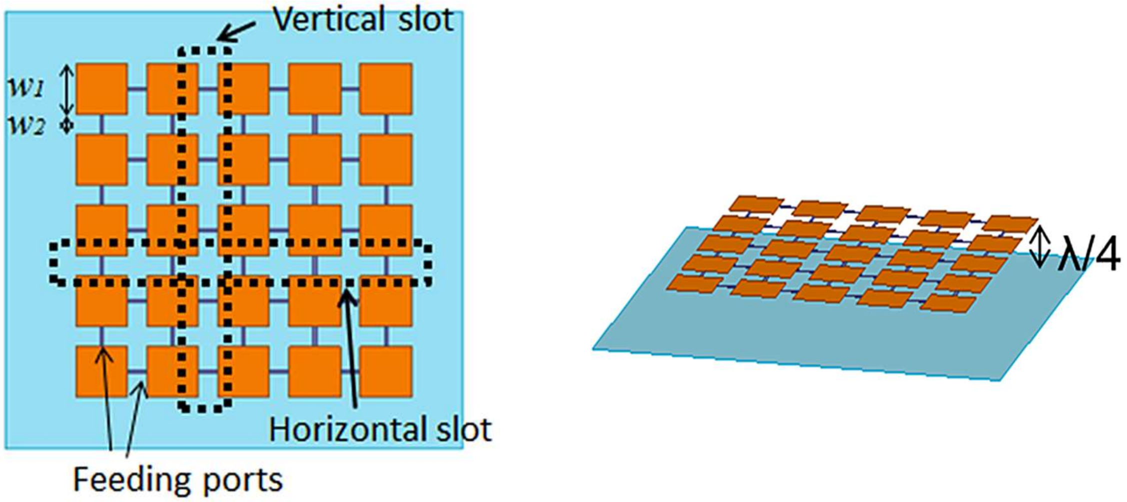

(a) (b)

Figure 2.10. 4×4 dual polarized LSA array with ground plane. (a) Top view. (b) Isometric view.

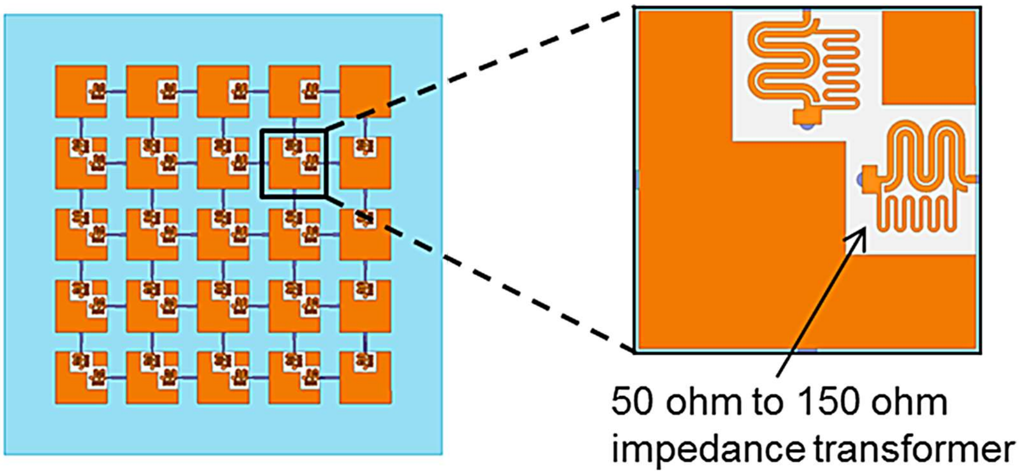

Figure 2.11. 4×4 dual polarized LSA array fed by 50 Ω to 150 Ω impedance transformers.

Since the LSA array has input impedance of 150 to 337 Ω and most wireless communication systems have characteristic impedance of 50 Ω, a wideband impedance transformer is needed such as the compact microstrip-couple-line-based impedance transformer [31] shown in Figure 2.11. However, the impedance transformer is complicated and difficult to fabricate. To simplify the feeding structure, parametric studies on the patch width (w_1) and slot width (w_2) were performed with a 3D full-wave electromagnetic field simulator (HFSS). In these studies, the patch width and slot width were changed while the feeding port spacing ($w_1 + w_2$) was kept constant and lumped ports were used to excite the LSA array. In antenna design, return loss (S_{11}) is usually used to represent the impedance bandwidth of the antenna. For the LSA array, since the antenna elements are connected, the mutual coupling can be high. It is not enough to just look at individual return loss from each port, thus overall return loss is used to represent the overall impedance matching of the antenna. The overall return loss is calculated as:

$$Overall\ Return\ Loss = 10\log(\frac{IncidentPower - Accepted\ Power}{IncidentPower}) \tag{2.1}$$

where *IncidentPower* is the time-averaged power from the source and *AcceptedPower* is the time-averaged power entering a radiation antenna structure.

Simulations were performed on a 4×4 LSA array for fast simulation speed, as larger number of slots require more computing power and simulation time. Figure 2.12 shows the simulation results of the parametric study. Based on the simulation results, larger slot width has broader bandwidth and higher impedance; larger patch width has narrower bandwidth and lower impedance. With large patch width, the capacitance between the slots increased and resulted in smaller impedance. To retain the bandwidth, instead of minimizing the slot width a new LSA design was proposed in which small diagonal slots are created on the patches to introduce additional capacitance on the patches, which results in decreased input impedance of the LSA array [34]–[36]. Figure 2.13 shows the 4×4 LSA array with small diagonal slots on the metallic patches. The LSA array is fed by 60 Ω lumped ports with small slot width, *g*, equals to 0.26mm and the patch width and slot width are adjusted to 21.5 mm and 3.5 mm, respectively. The simulated overall return loss of the 4×4 LSA array with small diagonal slots is shown in Figure 2.14. As shown in Figure 2.14, for the same feeding port impedance, the introduction of the small diagonal slots helps to increase the slot width and reduce the patch width and results in several dB improvement in overall return loss of the antenna array. The resulting overall return loss is less than -7 dB over the 4 to 6 GHz frequency band. Thus, the LSA array with small diagonal slots can be fed by transmission lines with characteristic impedance of 60 Ω directly.

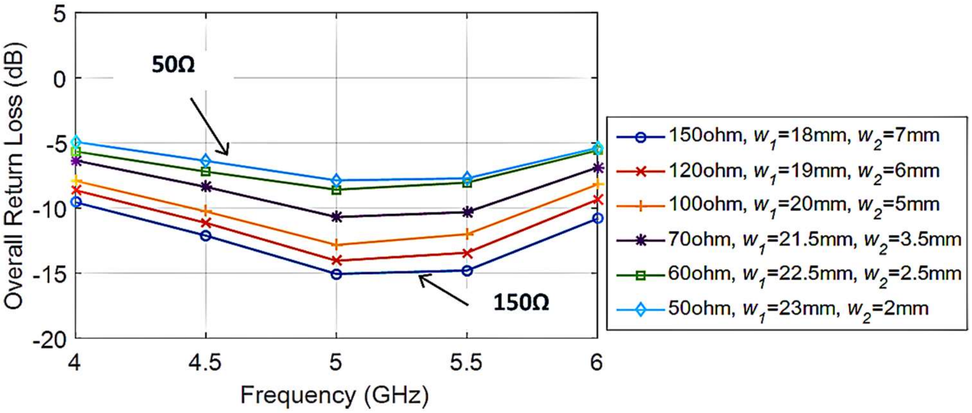

Figure 2.12. Simulated overall return loss of the 4×4 LSA array in difference slot width and patch width.

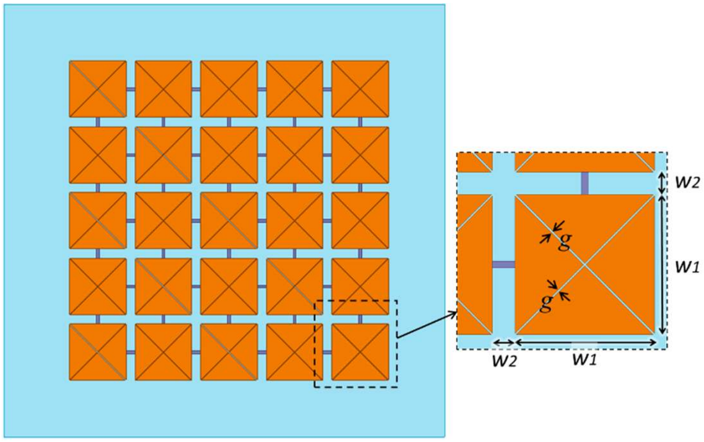

Figure 2.13. 4×4 dual polarized LSA array with small diagonal slots on the metallic patches.

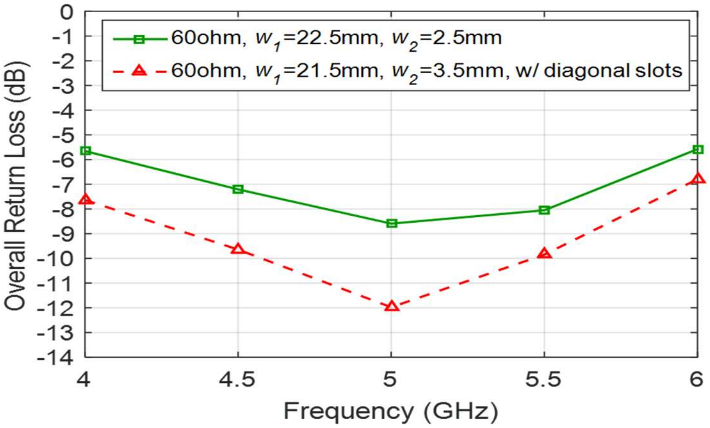

Figure 2.14. Simulated overall return loss of the 4×4 dual polarized LSA array with small diagonal slots on the metallic patches.

As the impedance value of 60 Ω is very close to 50 Ω, the impedance transformation can be easily achieved with a tapered microstrip transmission line instead of a complicated impedance transformer. Thus, a tapered microstrip was designed to feed the 4×4 dual polarized LSA array. The characteristic impedance of a microstrip can be calculated as follow [13]:

$$Z_o = \frac{87}{\sqrt{\varepsilon_r + 1.41}} \ln\left(\frac{5.98h}{0.8w + t}\right) \quad \text{for } h < 0.8w \qquad (2.2)$$

where ε_r is the dielectric constant of the dielectric substrate, h is the height of substrate, w is the width of the microstrip center conductor and t is the thickness of the microstrip center conductor. Thus, for constant values of ε_r, h, and t, the characteristic impedance of a microstrip can be changed by simply varying the width of the center conductor. Figure 2.15 shows the schematic and simulation results of the tapered microstrip. In the microstrip design, Rogers RO4350B material, with dielectric constant of 3.66 and thickness of 0.762 mm, was used as the substrate of the microstrip. The tapered microstrip transforms 50Ω to 60Ω. As illustrate in Figure 2.15a, the impedance transformation is performed by tapering the center conductor of the microstrip. The ground plane of the microstrip was also tapered to minimize its effect on the radiation pattern while feeding the LSA array. The simulated S_{11} of the tapered microstrip is below -20 dB and the S_{21} is close to 0 dB as shown in Figure 2.15c.

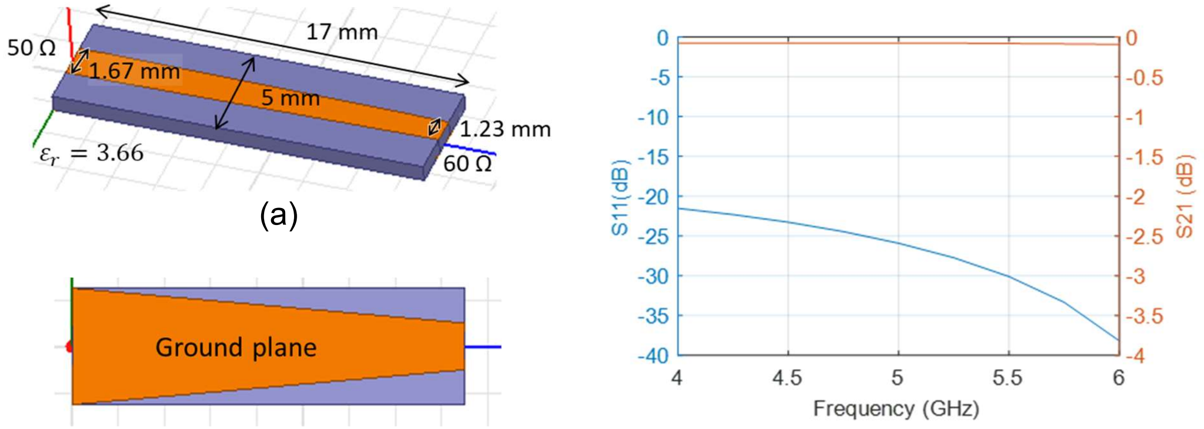

(a)

(b)

(c)

Figure 2.15. Tapered microstrip, 50 Ω to 60 Ω (a) Isometric view. (b) Bottom view. (c) Simulation results.

Figure 2.16 shows the 4×4 dual polarized LSA array fed by the tapered microstrips. As shown in Figure 2.16, the horizontal and vertical slots were fed by tapered microstrips from the back of the antenna array. In feeding the slots, the center conductors of the microstrips were connected to the metallic patches on one side of the slot, while the ground planes of the microstrips were connected to the metallic patches on the other side of the slot. A FR4 substrate with thickness of 0.4 mm and dielectric constant of 4.4 was added to the array design to support the metallic patches so that the metallic patches can be fabricated on the FR4 substrate. Due to the introduction of the FR4 substrate, which it affects the electrical length of the antenna array, the dimensions of the antenna array were adjusted. The patch width (w_1), slot width (w_2) and the diagonal slot width (g) were adjusted to 20 mm, 4 mm and 0.5 mm, respectively. Thus, the feeding port spacing is equal to 0.48λ at 6 GHz (highest frequency), where λ is the free-space wavelength. The spacing between the antenna array and the ground plane was also adjusted to 12 mm, which equals to 0.2λ at 5 GHz (center frequency).

The simulated results of the 4×4 dual polarized LSA array fed by tapered microstrips is shown in Figure 2.17. The simulated overall return loss is below -7 dB across the 4–6 GHz frequency band. Figure 2.17(b) shows the S_{11} of each microstrip feeds on the smith chart. As shown in the figure, the S_{11} curves circle around the center of the Smith Chart, which it shows that the tapered microstrips have reasonable good impedance matching to the input impedance of the antenna slots.

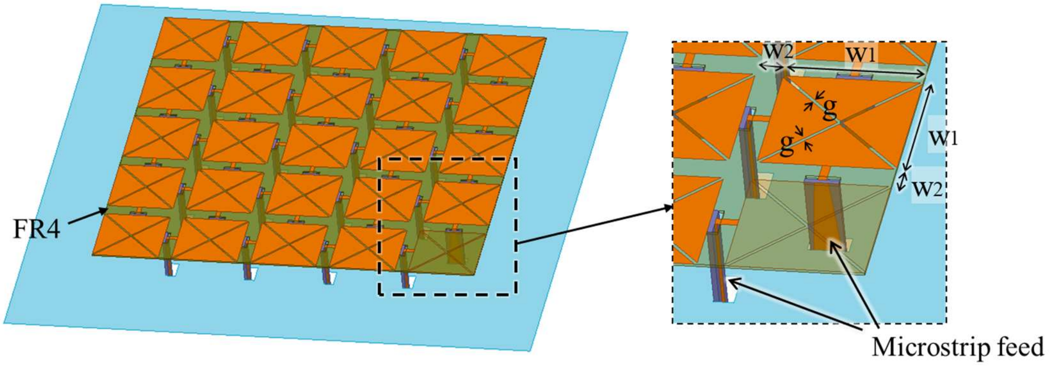

Figure 2.16. 4×4 dual polarized LSA array with small diagonal slots and microstrip feeds.

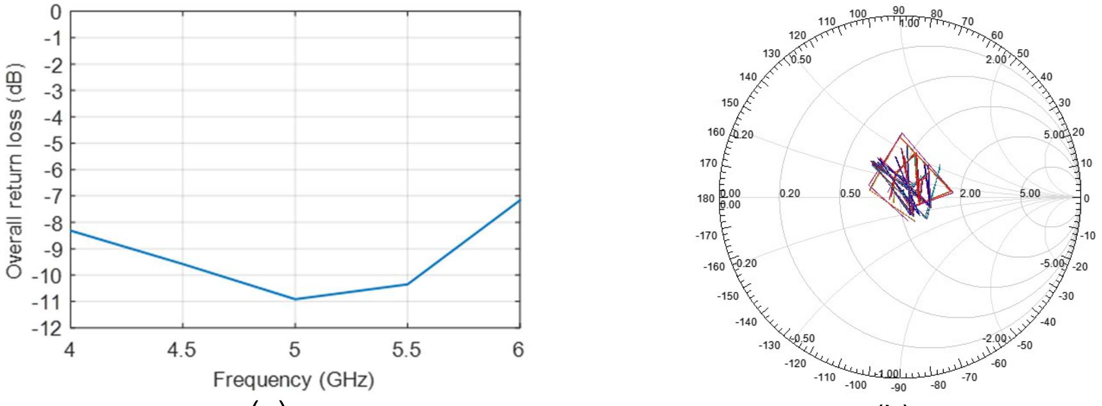

(a)

(b)

Figure 2.17. Simulated results of the 4×4 dual polarized LSA array fed by tapered microstrips. (a) Overall return loss. (b) S_{11} of microstrip feeds on a Smith Chart.

Based on the dimension parameters of the LSA array design in Figure 2.16, a 4×8 dual polarized LSA array with the microstrip feeds was modeled and simulated. In the simulation some of the microstrip feeds on the edge of the antenna array were terminated with 50 Ω loads as shown in Figure 2.18. The terminated feeds are the extra feeds when pairing the horizontal slot and vertical slot feeds to form circularly polarized subarrays, which will be discussed in the next paragraph. To support right hand circular polarization (RHCP), the microstrip feeds on the horizontal slots were excited with 90° phase delay relative to the microstrip feeds on the vertical slots. Figure 2.19 and Figure 2.20 show the simulated radiation characteristics of the 4×8 LSA array in the broadside direction. The simulated overall return loss is below -7 dB across the 4–6 GHz frequency band. Stable RHCP realized gain is obtained from the simulation, where the simulated gain ranges from 16.5 to 19 dBic. A decent axial ratio is obtained in the broadside direction, which is below 1 dB across the frequency band of interest.

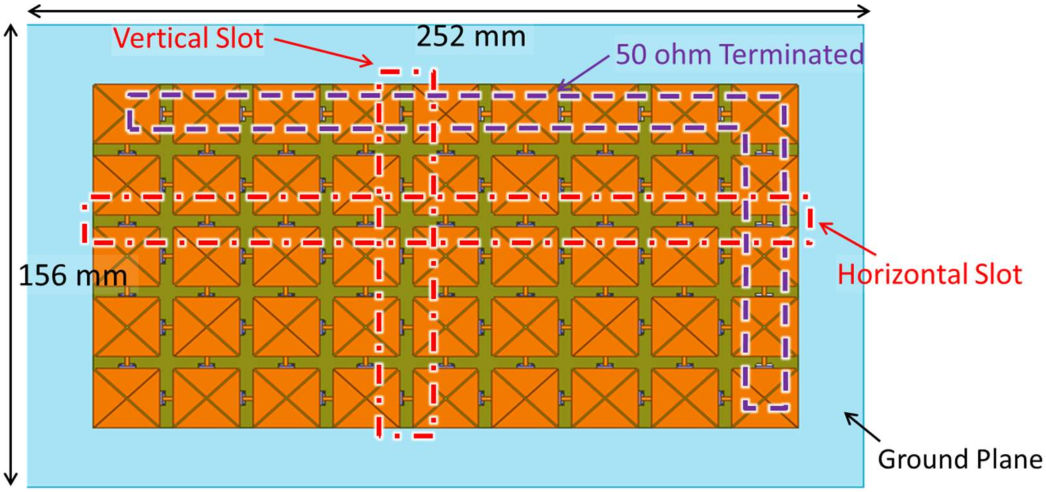

Figure 2.18. 4×8 dual polarized LSA array with small diagonal slots and microstrip feeds.

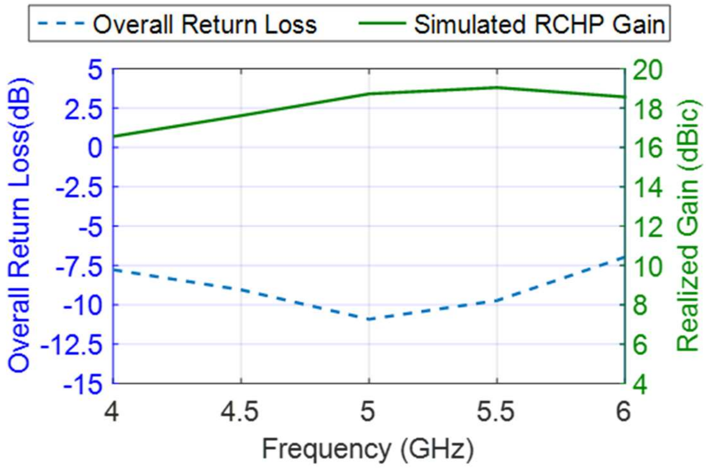

Figure 2.19. Simulated overall return loss and RHCP realized gain of the 4×8 dual polarized LSA array.

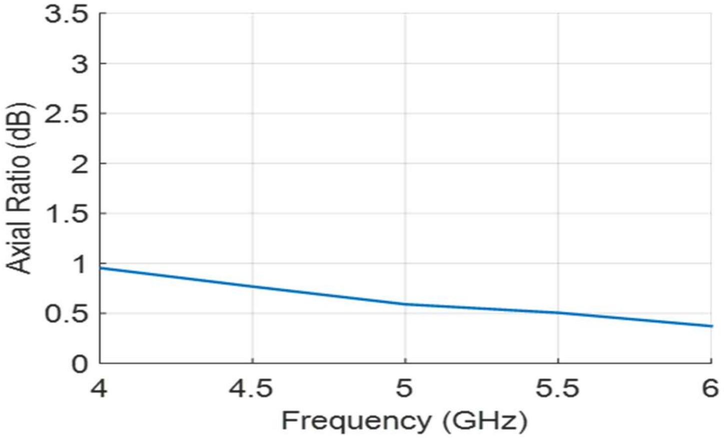

Figure 2.20. Simulated axial ratio of the 4×8 dual polarized LSA array.

As the antenna array only needs to perform beam-steering in the azimuth plane, an intermediate feeding network was designed to combine the antenna feeds, thus to reduce the number of feeds and form eight RHCP subarrays. For each subarray, a 4-way Wilkinson power divider [37] was used to combine the horizontal slot microstrip feeds to form a vertically polarized subarray and another 4-way Wilkinson power divider was used to combine the vertical slot microstrip feeds to form a horizontally polarized subarray. The vertically polarized subarray and the horizontally polarized subarray were paired up and fed by a three-stage broadband 90° hybrid coupler which provides stable 90° phase offset over the 4–6 GHz band for the vertically polarized and horizontally polarized subarrays to form a broadband RHCP subarray as shown in Figure 2.21. As a result, eight RHCP subarrays were formed. The extra feeds were terminated with 50 Ω loads to mitigate their effects on the radiation characteristics of the antenna array, as indicated in Figure 2.21a. If the extra feeds were left open, it would slightly affect the beam direction and the axial ratio of the antenna array. Figure 2.21c shows the isometric view of the 4×8 LSA array fed by the intermediate feeding network. Coaxial cables were used in the connections

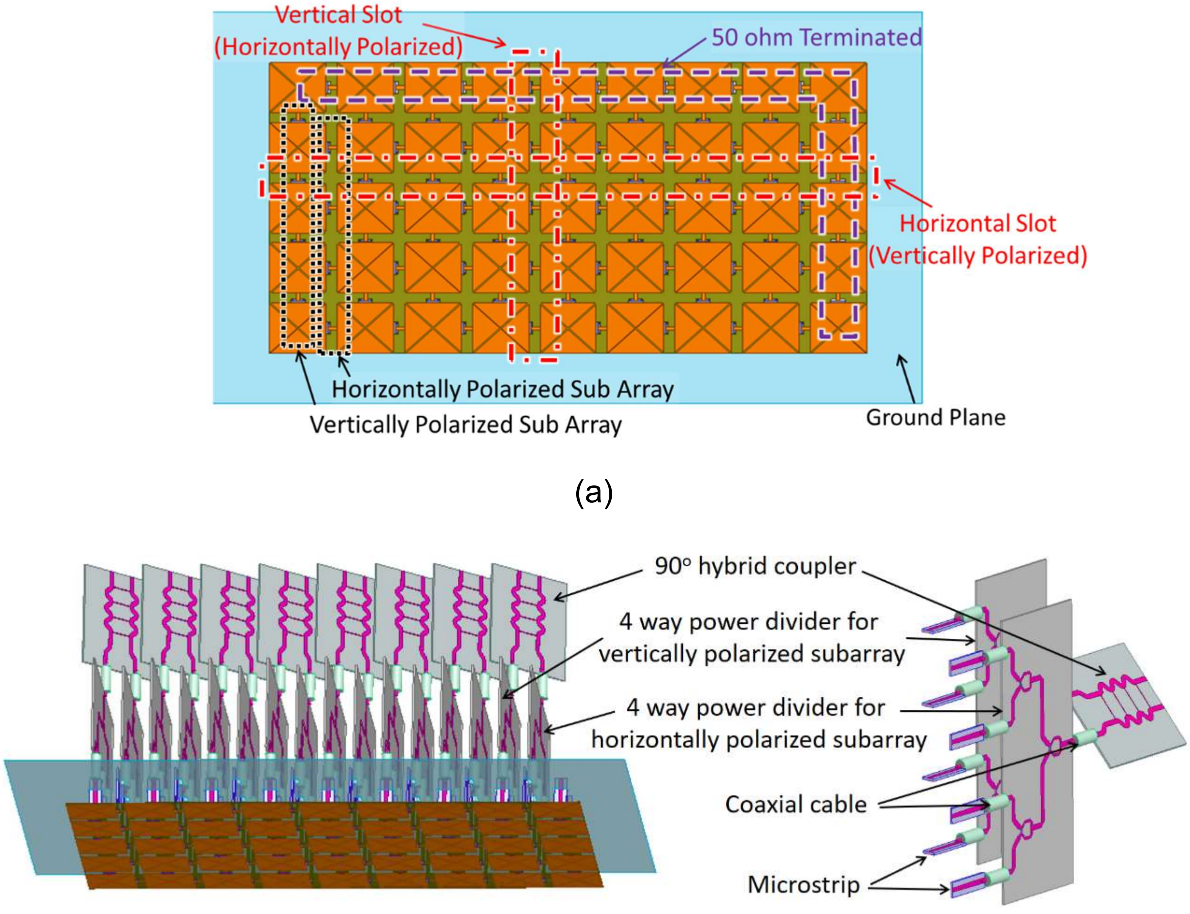

(a)

(b)

Figure 2.21. Schematic of the 4×8 LSA array with feed network: (a) Front view. (b) Isometric view.

between the microstrips and the power dividers, and the connections between the power dividers and the 90° hybrid couplers. The microstrips, power dividers and the 90° hybrid couplers were designed on Rogers RO4350B substrate which has dielectric constant of 3.66 and thickness of 0.762 mm. The detail design method about the broadband 90° hybrid coupler design will be cover in Chapter 3.

The simulated results of the overall return loss, RHCP realized gain, axial ratio and the mutual coupling between the RHCP subarrays of the 4×8 LSA array with the intermedia feed network are shown in Figure 2.22, 2.23 and 2.24. The simulated overall return loss is below -10 dB across the 4–6 GHz band. The improvement in the overall return loss is due to the 90° hybrid coupler which reflected energy from the output ports of the coupler is transmitted to the isolation port [38]. The RHCP gain is slightly decreased, which it ranges from 15.5 to 19 dBic. The decrease in gain is due to the insertion loss from the feed network. The simulated mutual coupling between the RHCP subarrays is below -13 dB. The axial ratios of the LSA array is increased slightly, however, it is below

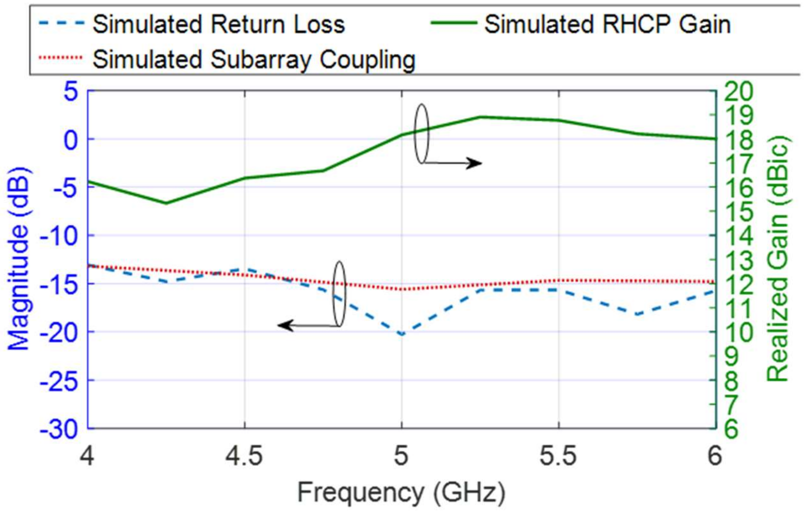

Figure 2.22. Simulated overall return loss, subarray coupling and RHCP realized gain of the 4×8 LSA array with feed network.

1.6 dB across the frequency band of interest. The simulated RHCP and the cross-polarization radiation patterns in x-z and y-z planes at different frequencies are shown in Figure 2.24. In the x-z plane, the 3-dB beamwidth ranges from 19° to 13° from 4 to 6 GHz. In the y-z plane, the 3-dB beamwidth ranges from 34° to 26°. The side lobe level of the radiation patterns is less than -13 dB. The cross-polarization level is more than 20 dB in the broadside direction.

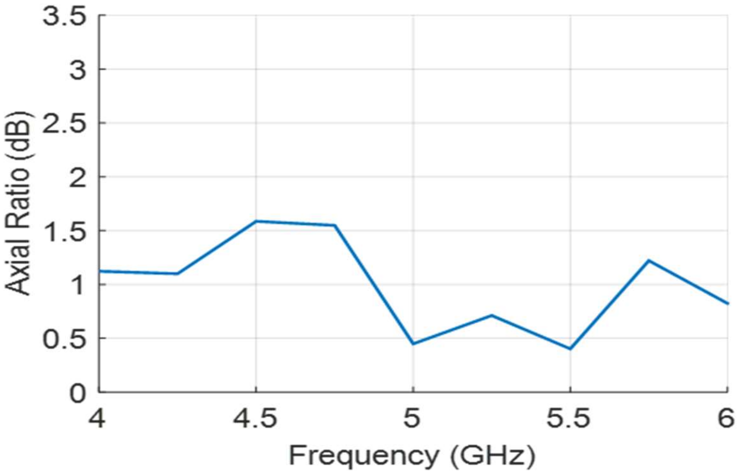

Figure 2.23. Simulated axial ratio of the 4×8 LSA array with feed network.

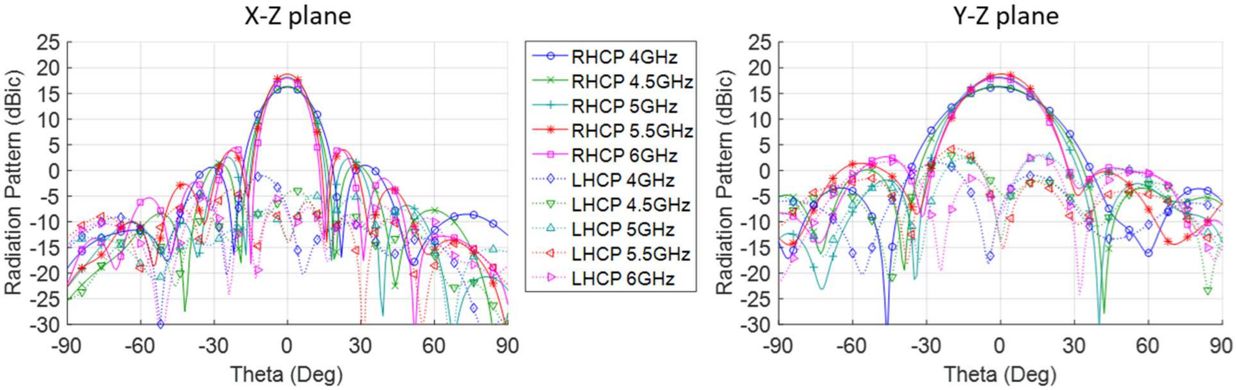

Figure 2.24. Simulated radiation pattern of the 4×8 LSA array with feed network in x-z plane and y-z plane.

2.2.2 Patch Antenna

Patch antenna is a low-profile antenna since its thickness can be less than tenth of a wavelength at the frequency of operation. For systems require extremely low-profile antenna installation, patch antenna is a suitable option, thus, antenna arrays based on patch antenna are also explored in this dissertation. The bandwidth of patch antenna is relatively narrow: a single layer patch antenna typically has a bandwidth around 5% [39]. However, several methods have been developed to widen the bandwidth of patch antenna, such as multiple stacked patches, increased substrate thickness, and use of U-slot on the patch [39].

For a single layer linear polarized patch antenna, the length of the metallic patch is around half wavelength at the resonant frequency. Standing wave is generated on the patch when the patch is excited with RF signal. The standing wave on the patch creates strong electric field on the edges (equivalent slots) of the patch as shown in Figure 2.25. Since the size of the patch is close to half wavelength, the direction of electric field on the edges of the patch are the same, this allows the electric fields to have constructive interference and radiate from the patch in the normal direction.

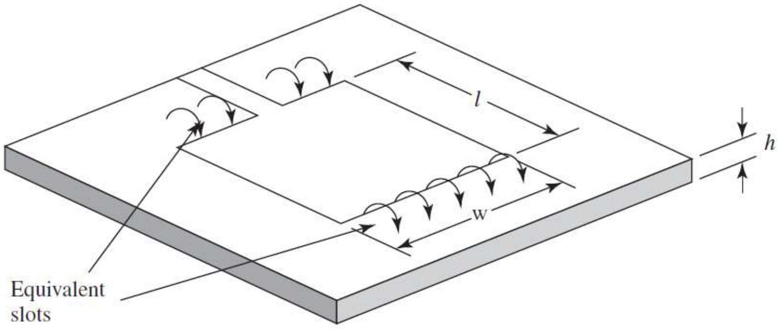

Figure 2.25. Linearly polarized patch antenna [39].

The resonant frequency of a patch antenna is highly depending on the size of the patch and the thickness of the antenna, it can be calculated as [39]:

$$f = \frac{c}{2(L+h)\sqrt{\varepsilon_e}} \tag{2.3}$$

where

$$\varepsilon_e = \frac{(\varepsilon_r + 1)}{2} + \frac{\varepsilon_r - 1}{2}\left(1 + \frac{12h}{w}\right)^{-\frac{1}{2}} \tag{2.4}$$

f is the resonant frequency, c is the speed of light, L is the length of the patch, h is the thickness of the substrate, ε_r is the relative dielectric constant of the substrate, and w is the patch width. The input impedance of a patch antenna is determined by the feed position. As shown in Figure 2.26, the magnitude of the voltage distribution on the patch has the highest value at the edges of the patch and equals to zero at the center of the

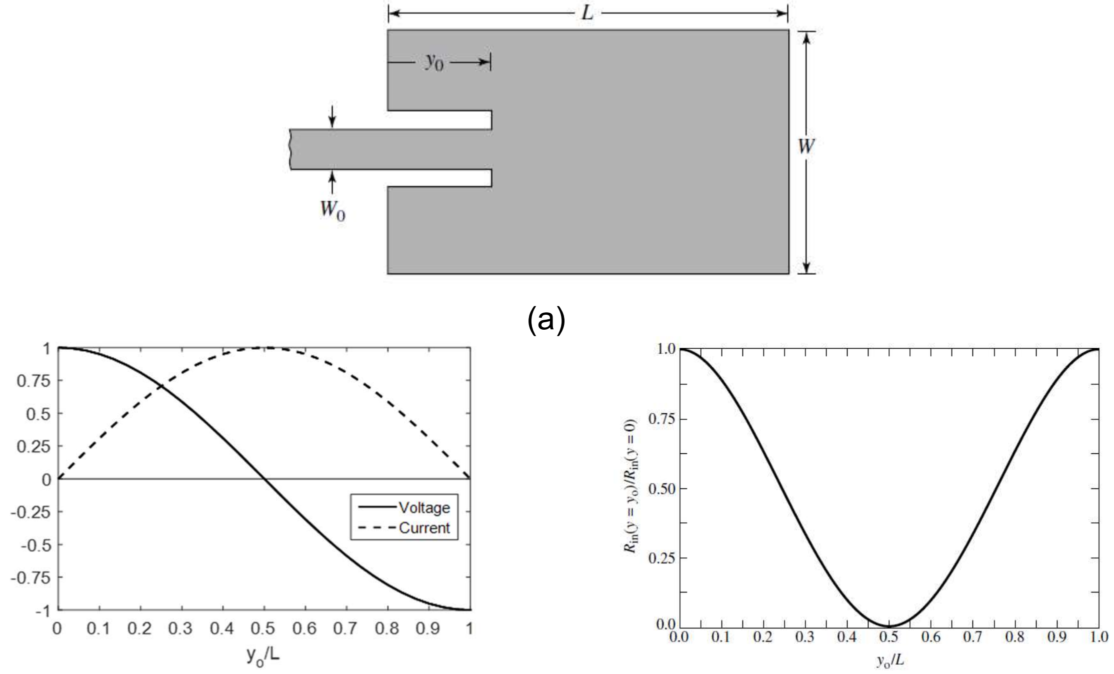

(a)

(b) (c)

Figure 2.26. (a) Schematic of a linearly polarized antenna fed by microstrip line. (b) Normalized voltage and current distribution on the patch. (c) Normalized input impedance of the patch antenna [13].

patch while the current distribution has its minimum value at the edges of the patch and reaches its maximum at the center of the patch. Thus, the input impedance of a patch antenna varies along the patch, it is maximum at the edge of the patch and it decrease as the feed position move toward the center of the patch as shown in Figure 2.26c.

There are several different methods can be used to feed a patch antenna. The commonly used methods are direct microstrip feed, probe feed, aperture-coupled feed and proximity-coupled feed as illustrated in Figure 2.27. Probe feed and aperture-coupled feed allow a feeding network to be built on the other side of the ground plane, which provide more design area and the feeding network will have less effect on the radiation pattern compare to the other two feed methods. For the antenna array design for directional networking application, probe feed was used as aperture-coupled feed tend to have high back lobe in the radiation pattern.

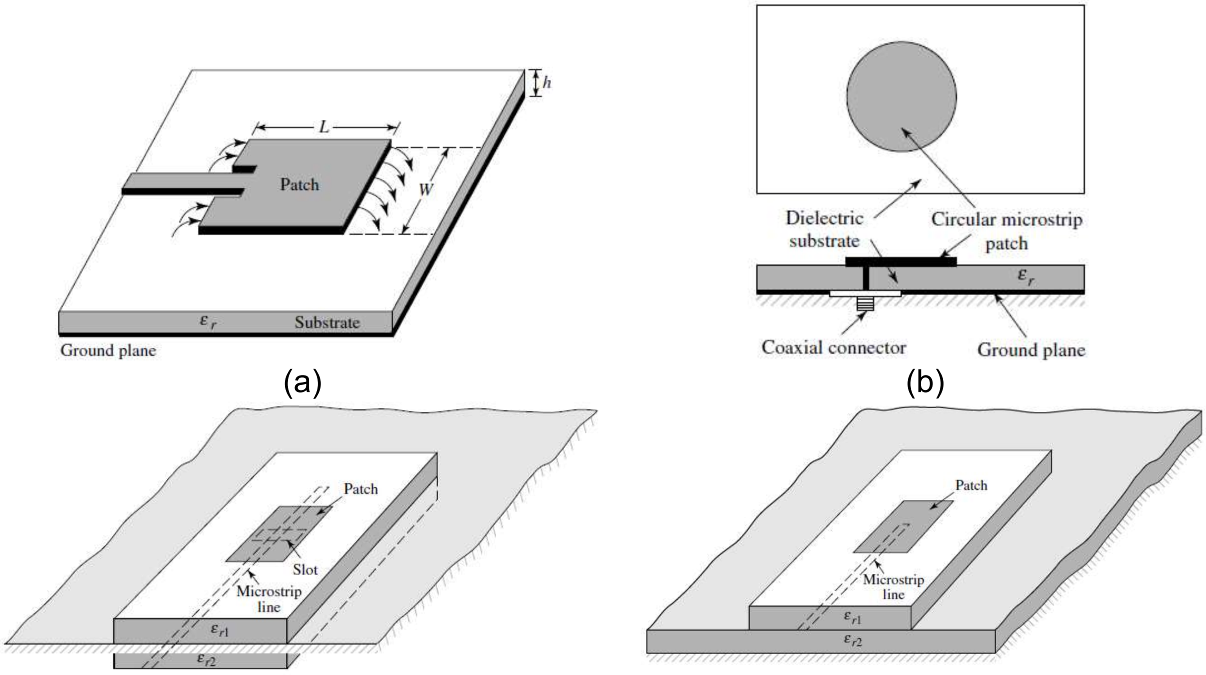

(c) (d)

Figure 2.27. Typical feeding methods for patch antenna: (a) Microstrip feed. (b) Probe feed. (c) Aperture-coupled feed. (d) Proximity-coupled feed [13].

2.2.2.1 Dual-fed Stacked Patch Antenna Array

For the patch antenna design, a narrower bandwidth was anticipated. Hence, the design operating frequency of the patch antenna was limited to 4.5–5 GHz. To fulfill the bandwidth requirement, dual-fed square-patch antenna was chosen, as dual-fed is known to provide improved axial ratio values over a broader bandwidth compared with single fed patch antenna (typical axial ratio bandwidth of a single fed patch antenna is less than 4% [40]–[44]). The single-element patch antenna design is shown in Figure 2.28. The antenna consists of three layers: parasitic patch layer, driven patch layer and feeding network layer. The square driven patch was fed by two probes from the back of the antenna to support dual polarization. The two feeding probes were fed by a 90° hybrid coupler to achieve right hand circular polarization. The 90° hybrid coupler was printed on the feeding network layer and the isolated port of the 90° hybrid coupler was terminated with a 50 Ω chip resistor. A square parasitic patch was added on top of the antenna to broaden the return loss bandwidth of the antenna [39]. The substrate used on the parasitic and driven patch layers was Rogers RO4003 which has a relative permittivity of 3.55 and thickness of 1.523 mm. The substrate used on the feeding network layer was Rogers RO4350 which has a relative permittivity of 3.66 and thickness of 0.762 mm. As a result, the total thickness of the antenna was 3.8 mm which is 0.06λ at 4.75 GHz.

The antenna was simulated in HFSS, whereby the dimensions of patch width w_1, w_2 and the feeding probe position d_1 and d_2 were tuned and determined to be 14.68 mm, 14.7 mm, 0.28 mm and 1.64 mm, respectively. The design property of the 90° hybrid coupler also helps to improve the return loss bandwidth of the patch antenna, which facilitates transmitting most of the reflected energy from the output port to the isolated port of the hybrid coupler. To clarify the intrinsic bandwidth limitation of the stacked patch antenna, a single element of this antenna was also simulated without the 90° hybrid coupler. Figure 2.29 and Figure 2.30 illustrate the simulation results of the single element patch antenna. In the frequency band of interest, the return loss is below -10 dB in both with and without the 90° hybrid coupler cases, and therefore stable RHCP realized gain around 6.4 dB with axial ratio below 1.9 dB is observed in this frequency band.

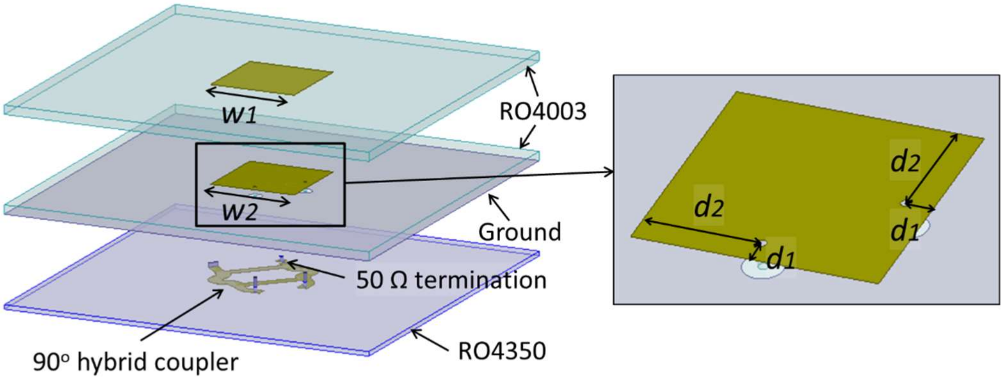

Figure 2.28. Dual-fed stacked patch antenna single element schematic.

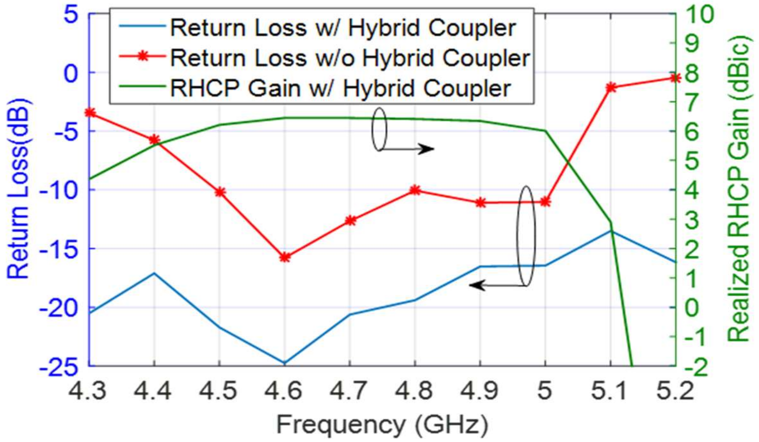

Figure 2.29. Simulated return loss and realized RHCP gain of the dual fed stacked patch antenna.

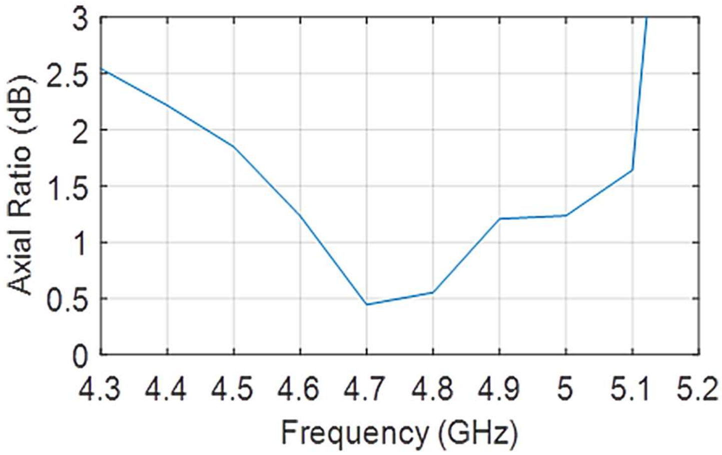

Figure 2.30. Simulated axial ratio of the dual fed stacked patch antenna.

A 4×8 patch antenna array was developed based on the single-element patch antenna in Figure 2.28, where the spacing between the antenna array elements was 0.66λ (at the center frequency of 4.75 GHz). To further improve the axial ratio of the antenna array, sequential rotation technique [21] was applied, whereby 2×2 antenna elements formed a square subarray and the elements were sequentially rotated 90° counterclockwise with respect to each other, as shown in Figure 2.31(a). As for feeding the antenna elements, these elements were combined vertically by a branch-line-based feeding network such that the feeding network form eight subarrays. The branch-line-based feeding network was designed on the same layer as the hybrid coupler and integrated with the antenna array, as shown in Figure 2.31(b). Thus, the overall size of the antenna array is 355 mm × 189 mm × 3.8 mm including the branched-line-based feeding network.

Figure 2.32 shows the schematic of the branched-line-based feeding network and its simulation results. In the feeding network design, quarter-wavelength impedance transformers [37] were used to match the impedance at the T-junctions of the feeding

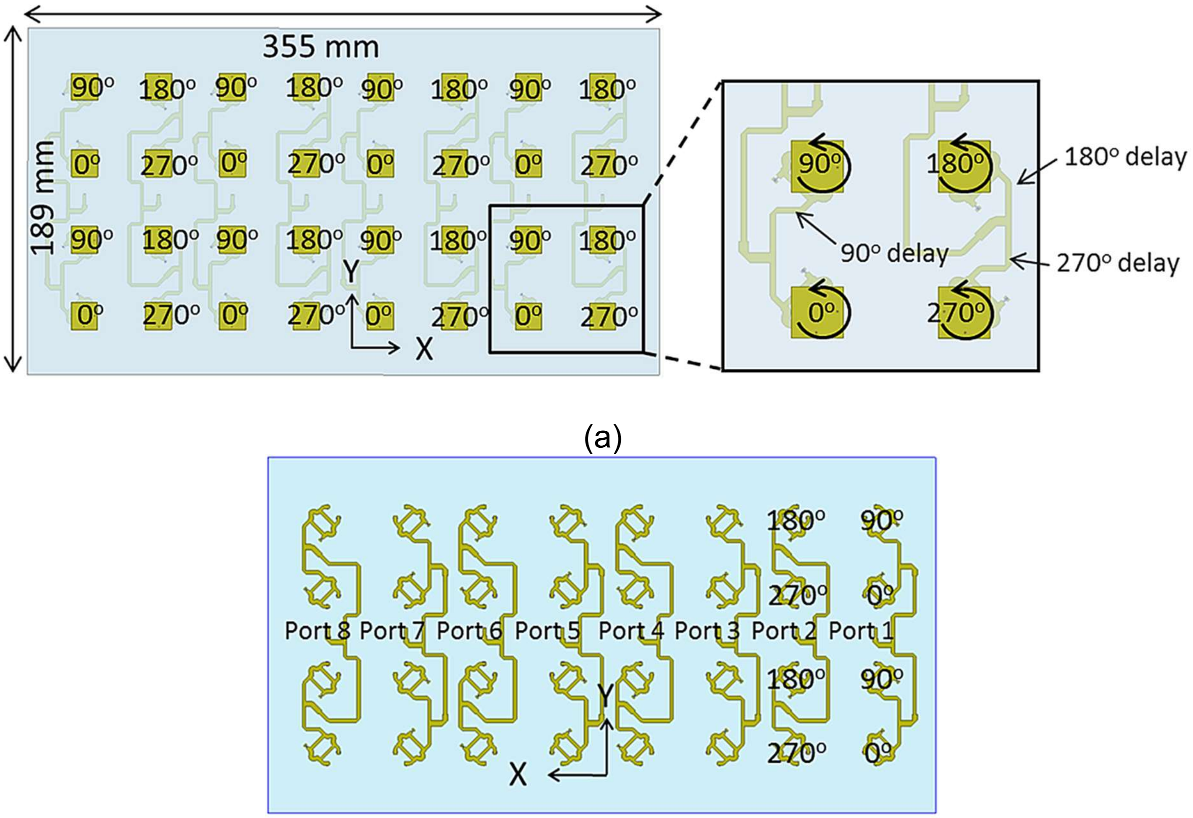

(a)

(b)

Figure 2.31. 4×8 dual-fed stacked-patch antenna array with sequential rotation. (a) Front view. (b) Back view.

network. The impedance at the T-junction of the feeding network is 25 Ω as the two 50 Ω branches are parallel to each other. Hence, the impedance transformer transforms 50 Ω to 25 Ω and its characteristic impedance was calculated to be 35 Ω. As the antenna polarization was RHCP and the elements were rotated counterclockwise, the rotation would cause a phase lead in the antenna element. To compensate for the rotation of the antenna element, the corresponding phase delays were added to the feeding network based on the angle of rotation, so that the directions of the E-field are synchronized in each element. Figure 2.32(b) illustrate the simulated return loss and transmission coefficient of the feeding network, which the return loss at ports 1 and 2 are less than -18 dB and the transmission coefficient of the branches are around -6.5 dB (-6 dB is the ideal

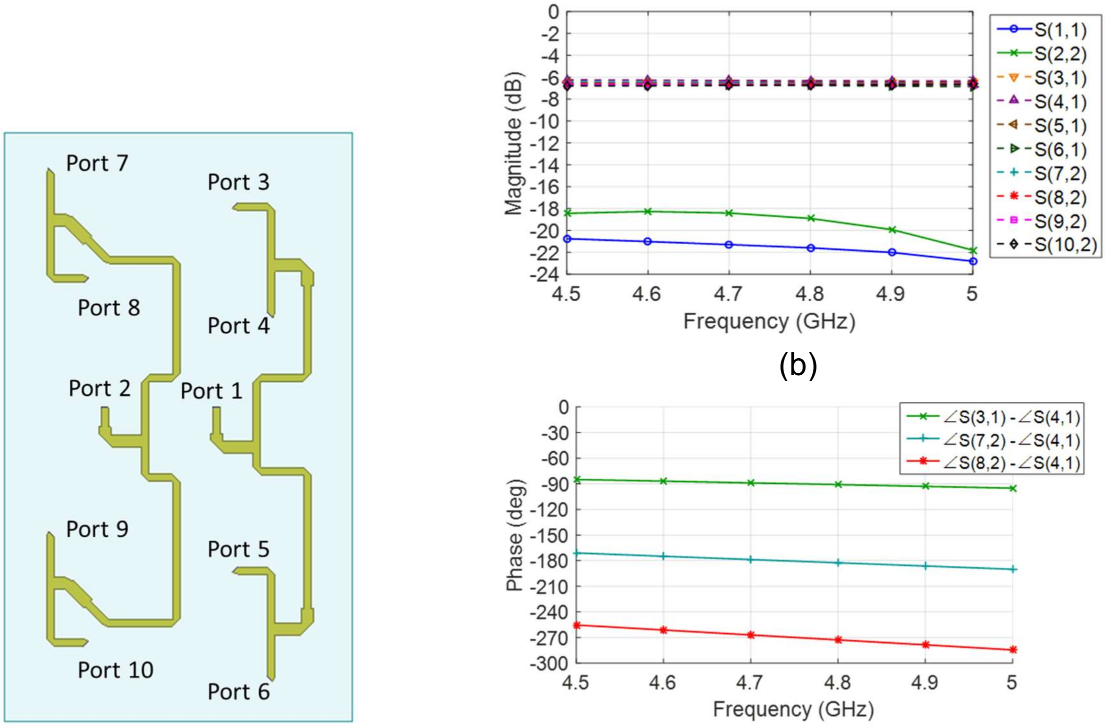

(a) (b) (c)

Figure 2.32. (a) Schematic of the branched-line-based feeding network. (b) Simulated return loss and insertion loss. (c) Simulated phase difference in between the paths.

value for a lossless two stage branch line feed network). Figure 2.32c shows the simulated phase difference in between the branch lines, and they are designed to be -90°, -180° and -270° to compensate the rotation of the antenna elements.

The 4×8 stacked patch antenna array with the feeding network were simulated in HFSS. Figure 2.33 shows the return loss and realized RHCP gain of the antenna array. The simulated return loss is less than -15 dB from 4.5 to 5 GHz. The simulated realized RHCP gain ranges from 19.8 to 21.5 dBic which is several dB higher than the 4×8 LSA array. The simulated axial ratio is below 0.5 dB as shown in Figure 2.34. The simulated radiation patterns of the patch antenna array in x-z and y-z planes are shown in Figure 2.35. In the x-z plane, the 3-dB beamwidth ranges from 10° to 9° from 4.5 to 5 GHz. In the y-z plane, the 3-dB beamwidth ranges from 20° to 18°. The side lobe level of the radiation patterns is less than -13 dB and the cross-polarization level is more than 25 dB in the broadside direction.

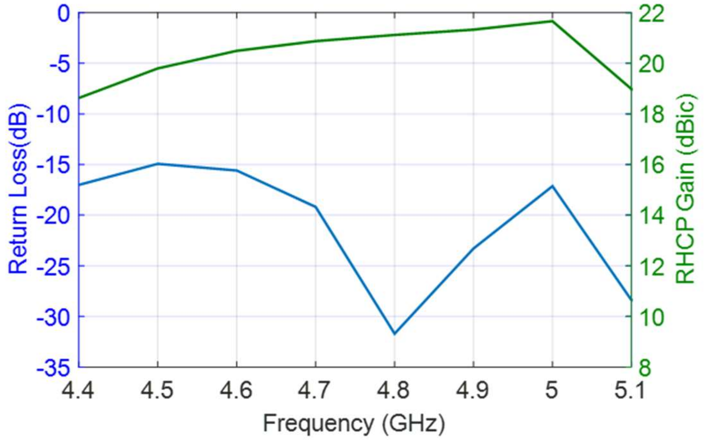

Figure 2.33. Simulated return loss and realized RHCP gain of the 4×8 stacked patch antenna array.

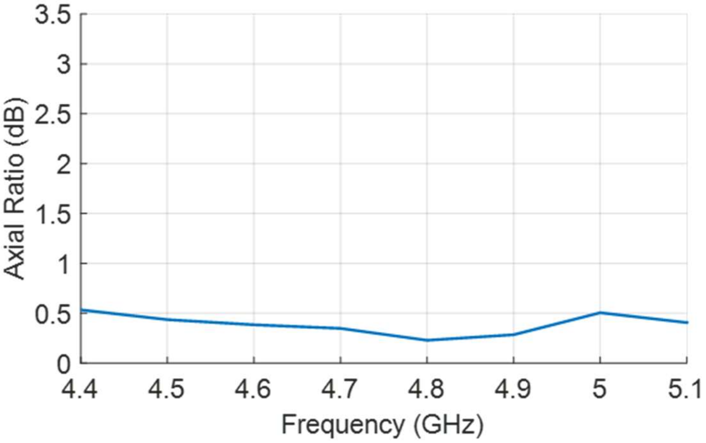

Figure 2.34. Simulated axial ratio of the 4×8 stacked patch antenna array.

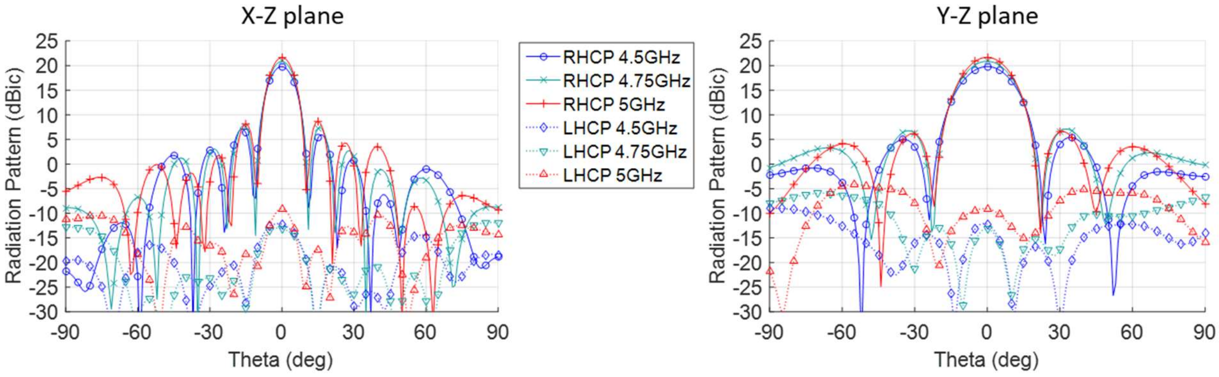

Figure 2.35. Simulated radiation pattern of the 4×8 stacked patch antenna array in x-z plane and y-z plane.

2.2.2.2 Dual-fed Stacked Patch Antenna Array with Air Gap and Annular Gaps

To further improve the gain of the stacked patch antenna array, a modified version of the antenna array was also designed [45]. In designing patch antenna, substrates with high relative permittivity can lower the gain and reduce the bandwidth of a patch antenna [46]. Several methods have been introduced to improve the gain of patch antennas, such as perforation of the surrounding substrate of the patch antenna to lower the surrounding effective relative permittivity, implementation of electromagnetic band-gap structure on the surrounding to block the propagation of the surface wave, and either use of substrate material with low relative permittivity or suspending the metallic patch over air [46]–[49].

In the modified design, a substrate with quite low relative permittivity was used and air gaps between the substrate and the ground plane were introduced to lower the effective relative permittivity. Figure 2.36a shows the initial design of the stacked patch antenna element which was similar to the patch antenna in Figure 2.28, except that air gaps were introduced between the substrate and the ground plane. The substrate used in this antenna design is Rogers RO4725JXR. It has a relative permittivity of 2.64 and thickness of 0.78 mm. The square parasitic patch size (w_1) and the square driven patch size (w_2) were 21.3 mm and 20 mm, respectively. The distance, h_1, between the parasitic patch and the driven patch was 2 mm and the distance, h_2, between the driven patch and the ground plane was 3 mm. The simulated return loss of the antenna is plotted on a smith chart in Figure 2.37. Due to the extra height from the air gap, extra inductance is introduced on the feeding probe; hence, the return loss curve is on the upper part of the smith chart, which means the input impedance of the antenna is not matched to the 50 Ω excitation ports. Thus, the dimensions of the patches were decided such that the return loss curve of the antenna lies on the matching circle of the smith chart so that the impedance of the antenna can be matched easily by introducing capacitance to the circuit.

To compensate for the inductance caused by the long feeding probe, capacitive annular gaps [45], [50] were introduced on the driver patch for each feeding probe where the center of the annular gaps were laid over the center of the feeding probes, as shown in Figure 2.36b. The capacitance of the annular gap depends on the gap width *g* and the inner radius *r*. To ensure the coupling between the feeding probe and the driver patch, the gap width was designed to be small and was equal to 0.2 mm. Thus, to change the

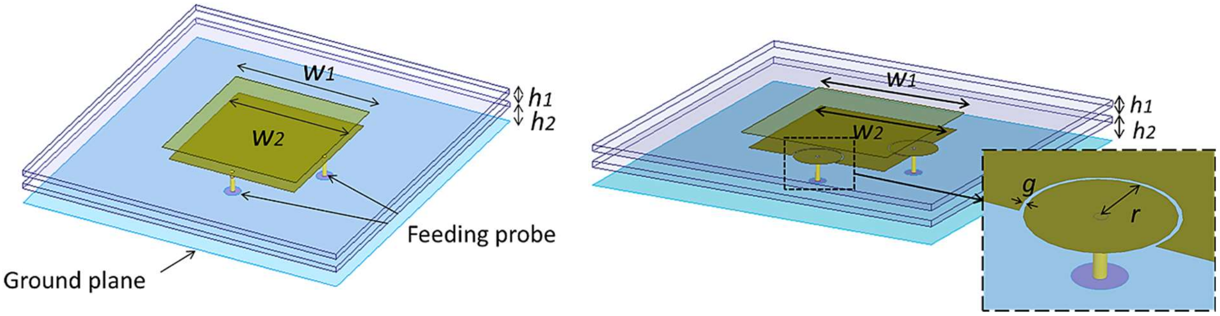

(a) (b)

Figure 2.36. (a) Dual-fed stacked patch antenna design with air gap. (b). Dual-fed stacked patch antenna design with air gap and annular gaps.

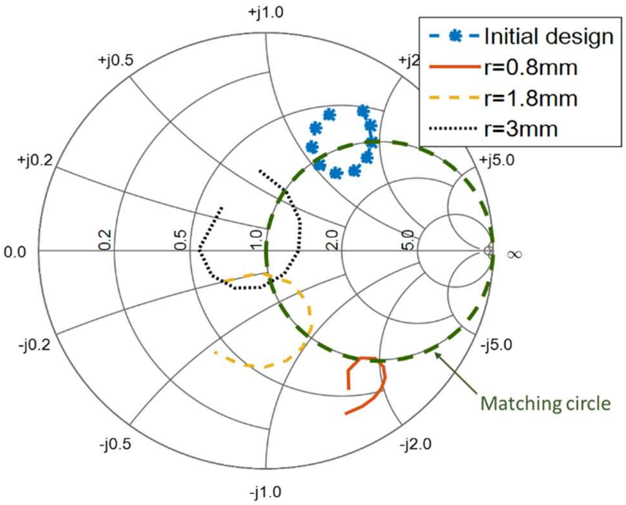

Figure 2.37. Return loss as a function inner annular gap radius on a smith chart.

capacitance of the annular gap, the inner radius of the annular gap needs to be changed so that it could generate the right capacitance and shift the return-loss curve to the center of the smith chart, as shown in Figure 2.37. The return-loss curve in the figure shifted toward the capacitance side of the smith chart and the feeding probe experienced more negative reactance for smaller *r*. This is because less capacitance is induced for smaller *r* and the capacitive reactance is inversely proportional to the capacitance, in which the impedance of a capacitor can be express as:

$$Z = \frac{1}{jwc} \tag{2.5}$$

where w is the angular frequency, c is the capacitance of the capacitor, and $j^2 = -1$. The return-loss curve shifted to the center of the smith chart when *r* = 3 mm. Thus, the annular gap produces right amount of capacitance to compensate the extra inductance when *r* = 3 mm. Figure 2.38 and Figure 2.39 illustrate the simulation results of the antenna with *r* = 3 mm. The -10 dB impedance bandwidth is about 16.7% from 4.4 to 5.2 GHz. Within this frequency band, the antenna gain on the broadside is slightly above 8 dBic (which is about 2 dB higher than of the stacked patch antenna in Figure 2.28) and the axial ratio is below 2.2 dB.

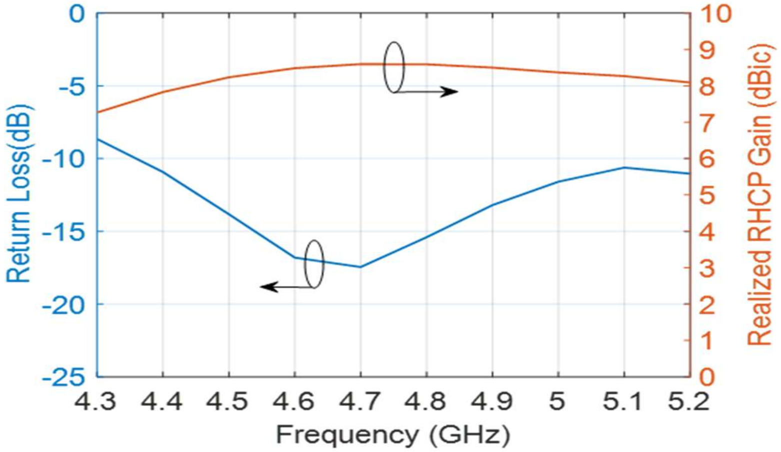

Figure 2.38. Simulated return loss and realized gain of the stacked patch antenna design with air gap and annular gaps.

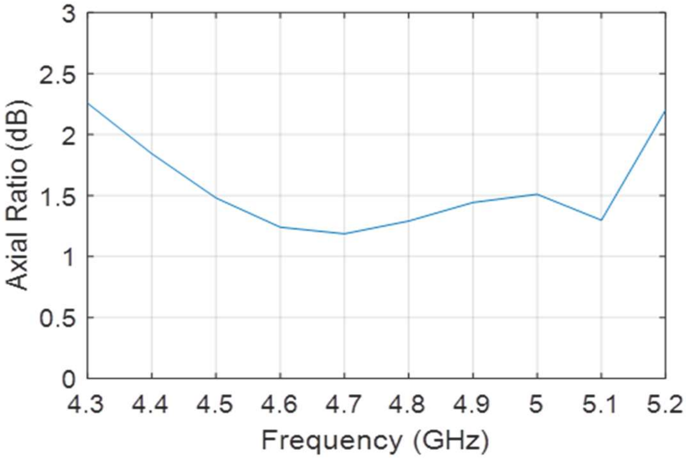

Figure 2.39. Simulated axial ratio of the stacked patch antenna design with air gap and annular gaps.

Table 2.1 shows the comparison of the stacked patch antenna design with annular gaps and the other state-of-the-art circularly polarized patch antenna designs. The antenna designs in [41] and [42] have similar gain as the proposed patch antenna design, however, they have much narrower bandwidth. For antenna designs which have similar bandwidth and gain as the proposed antenna, their size and thickness are usually larger [44], [52], [53], such as the antenna design in [53], its thickness is about twice the thickness of the proposed antenna. For patch antenna designs that have wider bandwidth, they are either have low gain [54]–[56] or have large antenna size that is not suitable for antenna array applications [57], [58]. The antenna designs in [57] and [58] have the parasitic patches placed around the driven patch to improve the bandwidth of the antenna, however, this greatly increase the size of the antenna and is not suitable for antenna array implementations. Overall, the proposed stacked patch antenna has reasonable wide bandwidth, high gain and compact in size compare to other published works on circularly polarized patch antenna.

Table 2.1. Comparison table of the stacked patch antenna design with annular gaps and other published patch antenna designs.

Antenna	Bandwidth (%)	Gain (dBic)	Dimension
Stacked patch antenna design with annular gaps [45]	16.7	8.3	$0.72\lambda_c\times0.72\lambda_c\times0.08\lambda_c$
[41]	4.6	8	$0.64\lambda_c\times0.64\lambda_c\times0.055\lambda_c$
[42]	4	8	$0.79\lambda_c\times0.79\lambda_c\times0.108\lambda_c$
[44]	16.4	8.3	$0.74\lambda_c\times0.74\lambda_c\times0.104\lambda_c$
[51]	13.5	8.6	$0.75\lambda_c\times0.75\lambda_c\times0.11\lambda_c$
[52]	16	9.2	$0.95\lambda_c\times0.95\lambda_c\times0.2\lambda_c$
[53]	16	8	$0.6\lambda_c\times0.6\lambda_c\times0.153\lambda_c$
[54]	20	4.5	$0.33\lambda_c\times0.33\lambda_c\times0.068\lambda_c$
[55]	27.5	6.2	$0.77\lambda_c\times0.7\lambda_c\times0.132\lambda_c$
[56]	20.4	7.6	$1.18\lambda_c\times1.18\lambda_c\times0.096\lambda_c$
[57]	20.7	8	$0.8\lambda_c\times0.8\lambda_c\times0.09\lambda_c$
[58]	24	8	$0.98\lambda_c\times0.98\lambda_c\times0.13\lambda_c$

An 8×8 antenna array based on the stacked patch antenna with air gap and annular gaps described above was designed and simulated. The element spacing of the antenna array is the same as the 4×8 stacked patch antenna array in Figure 2.31, which is 0.66λ at 4.75 GHz. Sequential rotation technique [21] was also implemented in the antenna array design to improve the axial ratio. A branch-line-based feeding network similar to the one for the 4×8 stacked patch antenna was designed and used to combine the antenna elements vertically to form eight subarrays. The schematic of the 8×8 stacked patch antenna array with branch line feeding network is shown in Figure 2.40. Examples of rotation angle of the antenna elements are also indicated in Figure 2.40a for sequential rotation implementation. Overall, the 8×8 antenna array has a size of 361 mm × 361 mm × 5.762 mm including the branched-line-based feeding network.

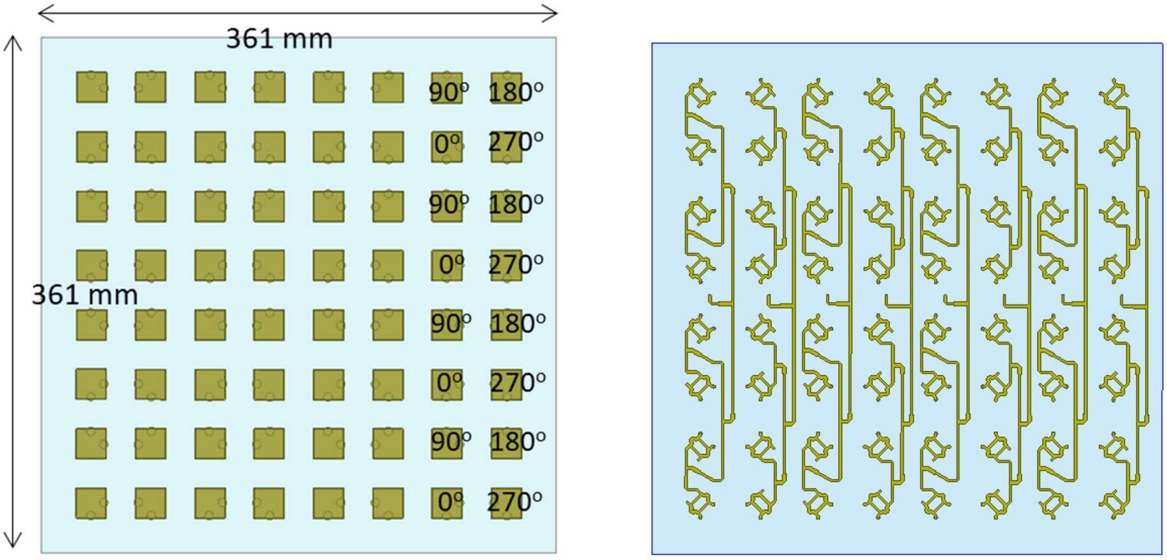

(a) (b)

Figure 2.40. Schematic of the 8×8 stacked patch antenna array with air gap and annular gaps: (a) Front view. (b) Back view.

The simulated return loss and realized RHCP gain of the 8×8 antenna array are shown in Figure 2.41. The simulated return loss is less than -14 dB from 4.4 to 5.2 GHz.

The simulated realized RHCP gain ranges from 23.5 to 25 dBic. The simulated axial ratio is below 2.3 dB as shown in Figure 2.42. The simulated radiation patterns of the patch antenna array in x-z and y-z planes are shown in Figure 2.35. The radiation patterns in both planes have the 3-dB beamwidth ranges from 10° to 9° from 4.4 to 5.2 GHz with side lobe level less than -13 dB. The cross-polarization level of the radiation pattern is more than 25 dB. In comparison to the 4×8 stacked patch antenna array, the 8×8 stack patch antenna with air gap has about 4 to 5 dB increase in gain, which 3 dB is from doubling of the antenna size and 2 dB is from the gain improvement in the antenna element. The total thickness of the 8×8 stacked-patch-antenna array is 5.8 mm, which also includes the feeding network. This is 2mm thicker than the 4×8 stacked patch antenna array.

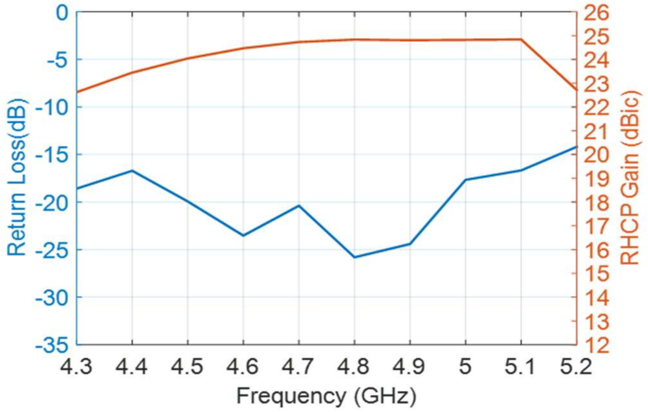

Figure 2.41. Simulated return loss and realized gain of the 8×8 stacked patch antenna design with air gap and annular gaps.

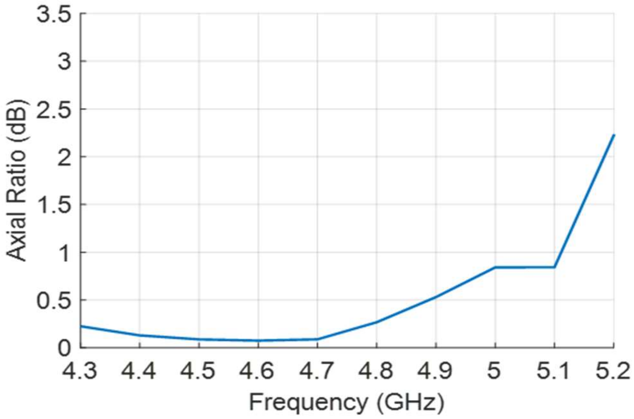

Figure 2.42. Simulated axial ratio of the 8×8 stacked patch antenna design with air gap and annular gaps.

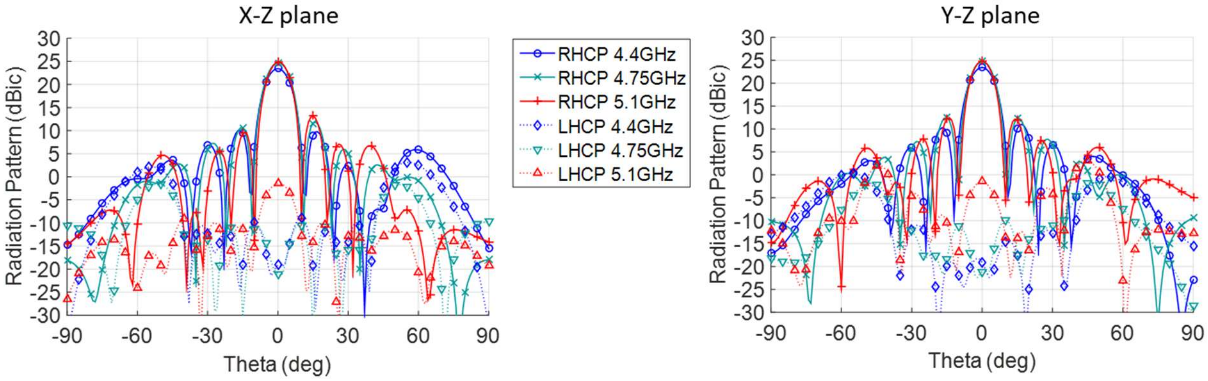

Figure 2.43. Simulated radiation pattern of the 8×8 stacked patch antenna array with air gap and annular gaps in x-z plane and y-z plane.

In summary, three RHCP antenna arrays have been designed and simulated in this chapter. The simulated radiation characteristics of the antenna arrays in the broadside direction are summarized in Table 2.2 including operating frequencies, gain, axial ratio, 3-dB beamwidth, cross-polarization level and dimensions of the antenna arrays without the feeding network. In comparison to the LSA array, the patch-antenna arrays have lower profile and higher gain but narrower operating bandwidth. Excluding the feed network, the 4×8 and the 8×8 stacked-patch-antenna arrays have thickness of $0.048\lambda_c$ and $0.08\lambda_c$, respectively. In comparison, the thickness of the LSA array is $0.2\lambda_c$.

The LSA array has intrinsically wide bandwidth. The measured return loss of the LSA array covered 4–6 GHz for return loss < -10 dB, while the patch antenna array covered 4.4–5.2 GHz. However, to achieve wideband property, the spacing between adjacent feeding ports of the LSA array needs to be less than or equal to half the wavelength corresponding to the highest operating frequency. This design requirement leads to a smaller antenna aperture and wider beamwidth, as well as it limits the gain of the antenna array. The antenna arrays have comparable circular polarization characteristics (i.e. axial ratio and cross-polarization level) over their operating frequency bands.

Table 2.2. Comparison table of the simulated radiation characteristics of the three antenna arrays in the broadside direction.

	4×8 LSA array	4×8 stacked patch antenna array	8×8 stacked patch antenna array
Frequency (GHz)	4–6	4.5–5	4.4–5.2
Bandwidth	40%	10.5%	16.7%
Gain (dBic)	15.5–19	19.8–21.5	23.5–25
Axial ratio (dB)	<1.6	<0.5	<2.3
3-dB beamwidth (x-z plane)	19°–13°	10°– 9°	10°– 9°
Cross-polarization level (dB)	>20	>25	>25
Dimensions (mm^3)	252×156×12	355×189×3	361×361×5

CHAPTER 3

BEAMFORMING AND FEED NETOWRKS

Antenna array beam-steering can be achieved mechanically or electrically. In mechanical beam-steering, a positioner is needed to physically move and rotate the directional antenna or antenna array, which is slow and susceptible to mechanical failure. In electrical beam steering, the phase of the signal going into to each antenna element is modified so that constructive interference of the electromagnetic field occurs in the desired direction. The phase of the signal can be modified in a digital or analog manner. In digital beamforming, the signals are processed digitally; there are more freedoms in controlling the phase and amplitude of the signal, which results in higher accuracy, lower side lobe level and support additional features such as calculation of angle of arrival. However, the computation power requirement and cost of the system are high. In analog beamforming, the signal phase is modified by electrically controlled phase shifters or a passive RF circuit with RF switches such as Rotman Lens, Butler matrix or Blass matrix. In this chapter both analog and digital beamforming are covered.

3.1 Array Factor

The far radiation field of an antenna array is the sum of the far radiation fields from each antenna element in the array and can be estimated using the following equation:

$$E_{(\theta,\phi)}^{Total} = E_{(\theta,\phi)} * AF \tag{3.1}$$

where $E_{(\theta,\phi)}$ is the far electric field radiated from the single antenna element and AF is the array factor of the antenna array. Hence by knowing the signal element's radiation pattern and the array factor of the antenna array, the radiation pattern of the antenna array can be estimated mathematically. The array factor of an antenna array depends on the antenna element spacing and the magnitude and phase of signal going into each antenna element, thus, the radiation pattern of an antenna array can be changed by changing any of these parameters. Consider an N-element linear array as shown in Figure 3.1. Assume the separation distance between the elements are the same and equals to d, and the amplitude of the signals going into the antenna elements are the same with progressive constant signal phase difference between the adjacent elements. The far field pattern of the antenna array in the x-z plane can be expressed as [59]:

$$E_{(\theta)}^{Total} = E_{(\theta)} * AF \tag{3.2}$$

where

$$\begin{aligned} AF &= \left(1 + e^{-j\beta_o(r_2-r_1)}e^{-j\psi} + e^{-j\beta_o(r_3-r_1)}e^{-j2\psi} + \cdots + e^{-j\beta_o(r_N-r_1)}e^{-j(N-1)\psi}\right) \\ &= (1 + e^{j(\beta_o d\, cos(\phi)-\psi)} + e^{j2(\beta_o d\, cos(\phi)-\psi)} + \cdots + e^{j(N-1)(\beta_o d\, cos(\phi)-\psi)}) \end{aligned} \tag{3.3}$$

β_o is the propagation constant, d is the element spacing, r_n is the distance to the far field observation point and ψ is the progressive constant signal phase difference between the adjacent elements.

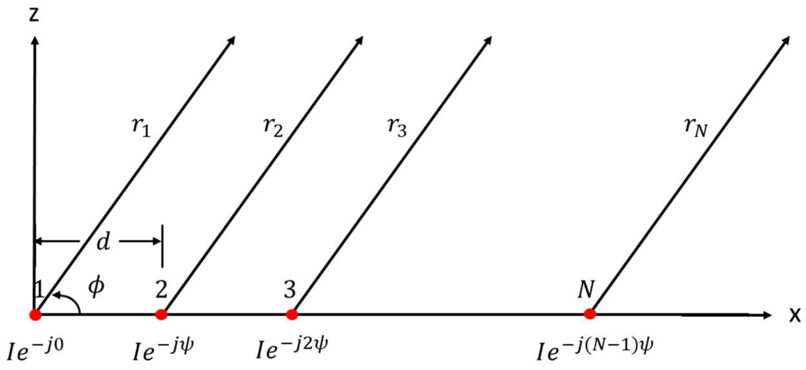

Figure 3.1. Schematic representation of N element array.

3.2 Analog Beamforming

In analog beamforming, electrically controlled phase shifters or a passive RF circuit with RF switches such as Rotman Lens, Butler matrix or Blass matrix are commonly used to modified the signal phase in each feed line [60]–[62]. Other approaches, such as reflectarray and transmitarray, also have been proposed [63], [64]. Electrically controlled phase shifters are generally costly and have high insertion loss. Rotman Lens generally has large electrical size and Blass matrix tend to have high insertion loss. Overall, it is believed that Butler matrix is the most simple and cost-effective approach. In this section, a new compact single substrate layer 8×8 Butler matrix beam-switching feed network was developed for the directional networking system [65].

3.2.1 Butler Matrix

The schematic of an 8×8 Butler matrix beam-switching feed network is shown in Figure 3.2. It consists of 22.5°, 67.5°, and 45° phase shifters, 90° hybrid coupler and crossover. Overall, the design includes twelve hybrid couplers, eight phase shifters and sixteen crossover junctions. Based on the schematic, the theoretical phase increment of the output ports for each input port of the 8×8 Butler matrix beam-switching feed network was calculated, as shown in Table 3.1. The phase increment in the output ports of the Butler matrix ranges from -157.5° to 157.5°, which results in steering angle of -60° to 60° for antenna array with element spacing of half wavelength. In realizing the 8×8 Butler matrix schematic in Figure 3.2, a microstrip-based Butler matrix feed network with new compact crossovers was designed on a Rogers RO4350B substrate which has relative permittivity of 3.66 and thickness of 0.762 mm. The components of the Butler matrix beam-switching feed network were designed separately and described in the following contents.

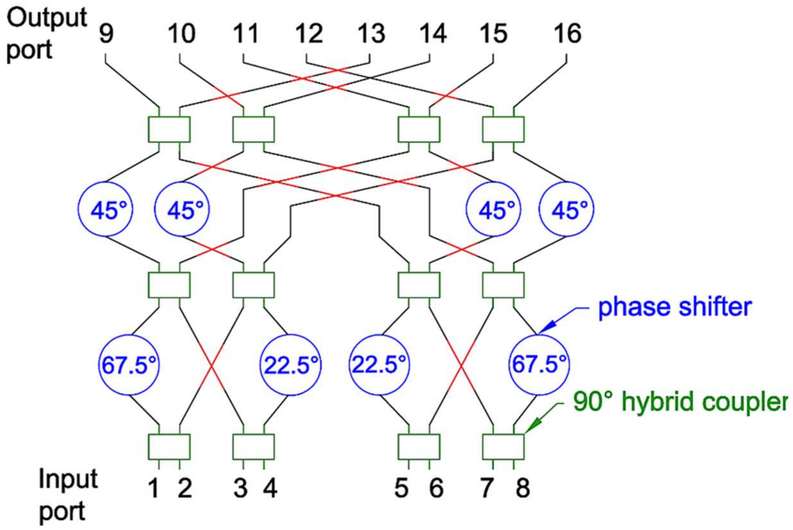

Figure 3.2. Schematic of 8x8 Butler matrix beam-switching feed network.

Table 3.1. Linear Phase Increment of the Output Ports for Each Input Port of the Butler Matrix Beam-Switching Feed Network.

Input Port	1	2	3	4	5	6	7	8
Phase increment in output ports	-22.5°	157.5°	-112.5°	67.5°	-67.5°	112.5°	-157.5°	22.5°

3.2.1.1 90° hybrid coupler

A 90° hybrid coupler equally splits the power of the input signal in the output ports with the phase of the output signals having a 90° phase difference between them. Figure 3.3 shows the schematic of a 90° hybrid coupler, where Z_0 is the characteristic impedance of the transmission lines. The branch-lines are a quarter of a wavelength long and the impedance of the horizontal branch-lines is $\frac{1}{\sqrt{2}}$ times of the characteristic impedance of the other transmission lines consisting the 90° hybrid coupler. In ideal case (perfect match and lossless), the *S* matrix of the 90° hybrid coupler can be express as follow:

$$S = -\frac{1}{\sqrt{2}}\begin{bmatrix} 0 & j & 1 & 0 \\ j & 0 & 0 & 1 \\ 1 & 0 & 0 & j \\ 0 & 1 & j & 0 \end{bmatrix} \tag{3.4}$$

where the reflection coefficient of the input and output ports equal to 0, S_{21} (see port label in Figure 3.3) equals to $-\frac{j}{\sqrt{2}}$ (half-power, -90° phase shift from port 1 to 2), and S_{31} equals to $-\frac{1}{\sqrt{2}}$ (half-power, -180° phase shift from port 1 to 3). Detailed derivation of the *S* matrix can be found in [37]. As shown in Figure 3.3, the 90° hybrid coupler is symmetry, any of the ports can be an input port. The 90° hybrid coupler is also frequency dependent, as the length of the branch-lines are equal to a quarter of a wavelength, the bandwidth of the coupler is limited to 10%–20%.

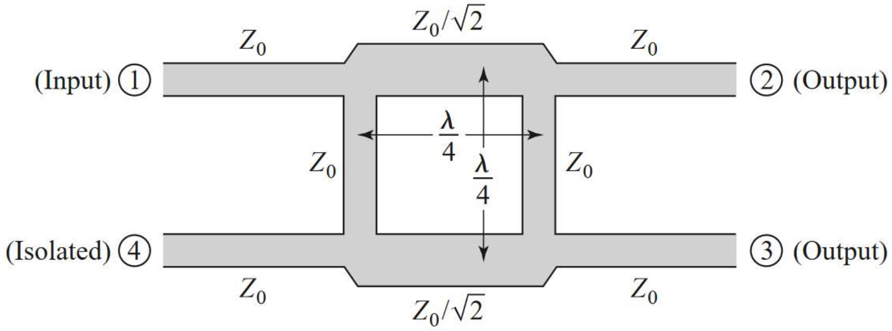

Figure 3.3. Schematic of a 90° hybrid coupler [37].

The bandwidth of a 90° hybrid coupler can be increased by cascading the branch line sections [66]. Figure 3.4a shows the three-stage 90° hybrid coupler[66] which was designed to cover the 4–6 GHz frequency band. As shown in the figure, the microstrip line of the hybrid coupler was meandered to minimize the size of the hybrid coupler. For fast modeling and tuning, the 90° hybrid coupler[66] schematic was drawn in Keysight's ADS software using microstrip transmission line components as shown in Figure 3.4b. The ADS schematic was then converted to a circuit layout and simulated in HFSS for full-wave simulation as shown in Figure 3.4a. The width of the meandered branch lines and the vertical branch lines were adjusted to 1.77 mm and 0.195 mm respectively, which correspond to characteristic impedance of 47.8 Ω and 122.7 Ω.

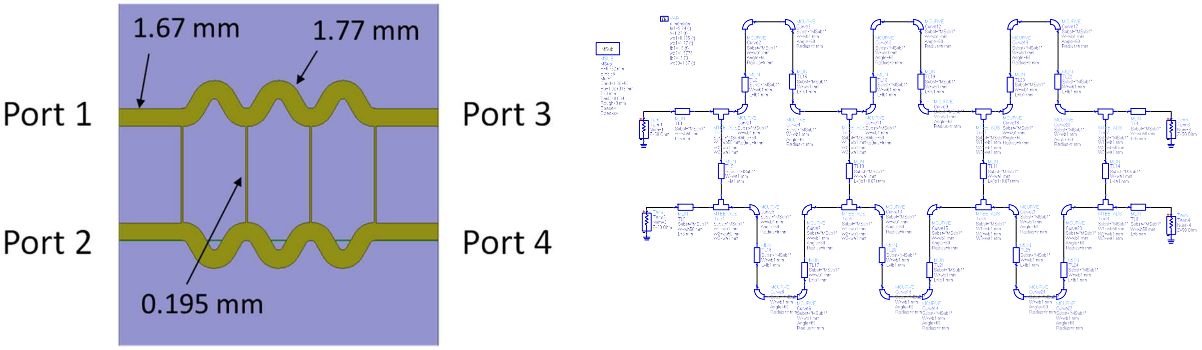

(a) (b)

Figure 3.4. (a) Schematic of the 90° hybrid coupler. (b) ADS schematic of the 90° hybrid coupler.

The simulated and measured results of the 90° hybrid coupler are shown in Figure 3.5. The measured results agree well with the simulated results. The simulated and measured return losses are less than -14 dB from 4 to 6 GHz. The transmission coefficients range from -3 to -4 dB, thus, the insertion loss of the circuit is less than 1 dB. The simulated and measured phase difference between the output ports of the 90° hybrid coupler are shown in Figure 3.5d, which are within the range of 90°±5° throughout the frequencies of interest.

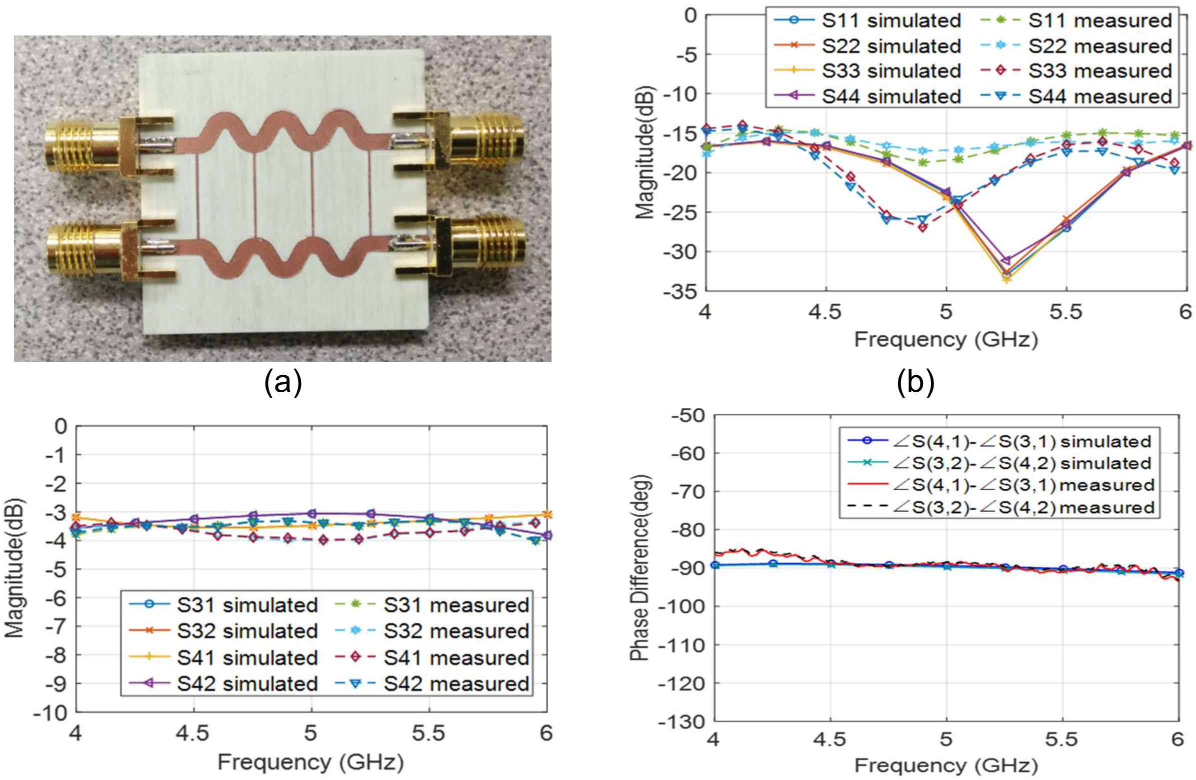

(a) (b)

(c) (d)

Figure 3.5(a) Fabricated 90° hybrid coupler. (b) Simulated and measured return loss. (c) Simulated and measured insertion loss. (d) Simulated and measured results of phase difference in the output ports of the hybrid coupler.

3.2.1.2 Crossover

The traditional way of implementing a crossover junction is to connect two 90° hybrid couplers in series [62]. However, the hybrid-coupler-based crossover dramatically increases the size of the Butler matrix as it requires 16 crossover junctions. To reduce the size of the Butler matrix, the conductor-backed coplanar waveguide crossover [67] was chosen to implement in the Butler matrix design due to its broadband characteristic and compact size. Figure 3.6 shows the original coplanar waveguide crossover design in [67]. The crossover consists of two orthogonal coplanar waveguides on top and bottom layers of the substrate, the coplanar waveguide ground planes on the top layer are grounded to the ground plane on the bottom layer through via holes. The center conductor of the coplanar waveguide on the top layer connects to 50-Ω microstrip lines directly and the center conductor of the coplanar waveguide on the bottom layer connects to 50-Ω microstrip lines on the top layer through via holes, which allows two microstrip RF paths crossing each other by using two orthogonal coplanar waveguides on top and bottom layers of the substrate.

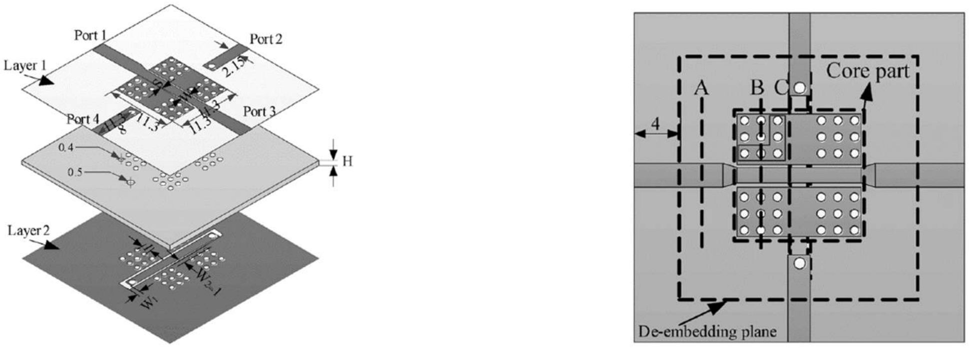

(a) (b)

Figure 3.6. 3-D Layout of the proposed microstrip crossover junction. (b) Top view (Unit: mm) [67].

The characteristic impedance of a conductor-backed coplanar waveguide can be calculated from the equations below [68]:

$$Z_0 = \frac{60\pi}{\sqrt{\varepsilon_{eff}}} * \frac{1}{\frac{K(k)}{K(k')} + \frac{K(kl)}{K(kl')}} \tag{3.5}$$

$$k = \frac{w}{w+2s} \tag{3.6}$$

$$k' = \sqrt{1-k^2} \tag{3.7}$$

$$kl' = \sqrt{1-kl^2} \tag{3.8}$$

$$kl = \frac{tanh(\frac{\pi w}{4h})}{tanh\,(\frac{\pi(w+2s)}{4h})} \tag{3.9}$$

$$\varepsilon_{eff} = \frac{1 + \varepsilon_r \frac{K(k')K(kl)}{K(k)K(kl')}}{1 + \frac{K(k')K(kl)}{K(k)K(kl')}} \tag{3.10}$$

$$K(x) = \int_0^{\frac{\pi}{2}} \frac{d\phi}{\sqrt{1 - x^2 \sin^2 \phi}} \tag{3.11}$$

where w is the center conductor width, s is the gaps between the center conductor and ground planes on both sides of the center conductor, and h is the high of the dielectric substrate, as shown in Figure 3.7. Thus, the impedance of a conductor-backed coplanar waveguide depends on the center conductor width, gaps between center conductor and ground planes and the high of the substrate layer. Equations 3.5–3.11 are for conductor-backed coplanar waveguides with large or infinite ground planes. In general RF circuit, the size of ground planes is finite and via holes are used to connect the ground planes on the top and bottom of the coplanar waveguide to avoid the leakage of the RF signal. Thus, the position of the via holes is another parameter affecting the impedance of the coplanar waveguide.

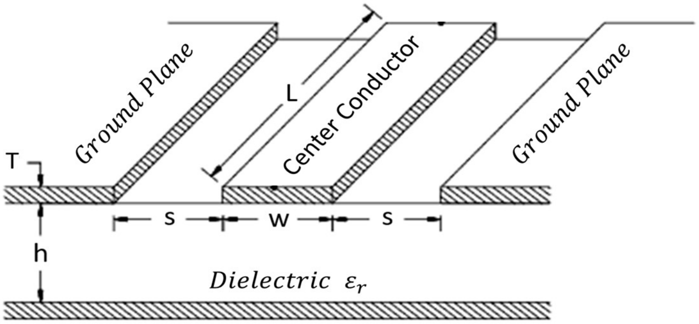

Figure 3.7. Coplanar waveguide schematic.

The electric field distribution in a conductor-backed coplanar waveguide depends on the center conductor width (w), gaps (s) between center conductor and ground planes, and the high (h) of the substrate layer. If the dimensions of w and s are relatively small compared to h, the coplanar mode is dominant, which the electric fields concentrate between the center conductor and the ground planes on the top layer. If the dimensions of w and s are comparable to h, the microstrip mode is dominant, which the electric fields concentrate between the center conductor and the ground planes on the bottom layer as shown in Figure 3.8. In the crossover design, the coplanar mode is preferred (small w and s) for minimum interference in between the coplanar waveguides on the top and bottom of the substrate. However, the width of the 50-Ω microstrip lines is another factor to be considered for smooth microstrip to coplanar waveguide transition.

Figure 3.8. Electric field distribution of a conductor-backed coplanar waveguide [69].

In the new crossover design for the Butler matrix implementation, the size of the crossover was further reduced by reducing the number of via holes as well as the center conductor width and gaps of the coplanar waveguides. Figure 3.9 shows one of the reduced-size crossovers (*Design 1*) with the coplanar waveguide portion reduced to 5×5 mm^2. The total number of via holes connecting the ground planes of the coplanar waveguides was reduced to four. The via holes were positioned at a distance of 0.8 mm (d) away from the edges of the ground planes on the top layer and the diameter of the via holes were 0.6 mm. The smallest drill bit for the milling machine in our lab is 0.15 mm, so the dimension of s was set to 0.16 mm to ensure strong coupling between the center conductor and the ground planes on the same layer as the center conductor so that the electric fields will concentrate in the gaps. The center conductor width (w) was adjusted to 1.2 mm. The simulated and measured performances of the reduced-size crossover are shown in Figure 3.10. Reasonable good performance was obtained in both simulated and measured results from 0.5 GHz to 8 GHz. The simulated and measured return loss on each port is less than -17 dB. The insertion loss in the two orthogonal paths is less than 1 dB with isolation between the two paths more than 25 dB and the phase difference of less than 3°. In the frequency band of interest (4–6 GHz), the simulated and measured return losses are less than -19 dB with insertion loss less than 0.7 dB, isolation between the two paths more than 26 dB, and the phase difference between the two paths less than 2°.

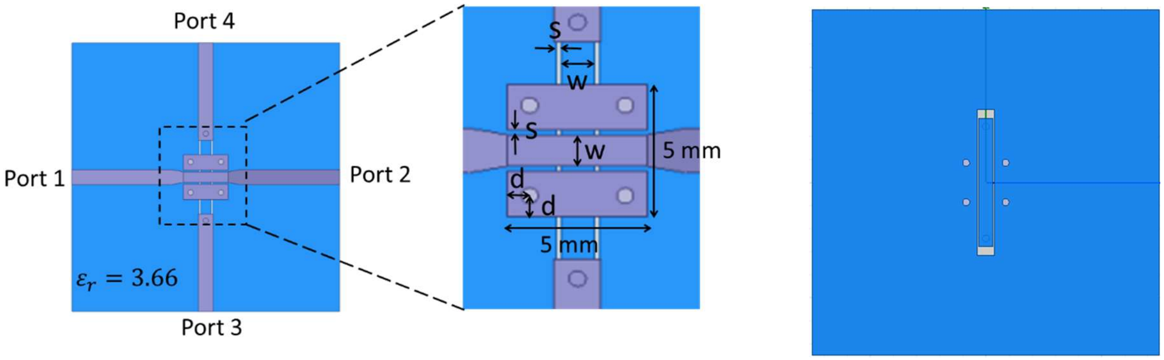

(a) (b)

Figure 3.9. Crossover Design 1: (a) Top view. (b) Bottom view.

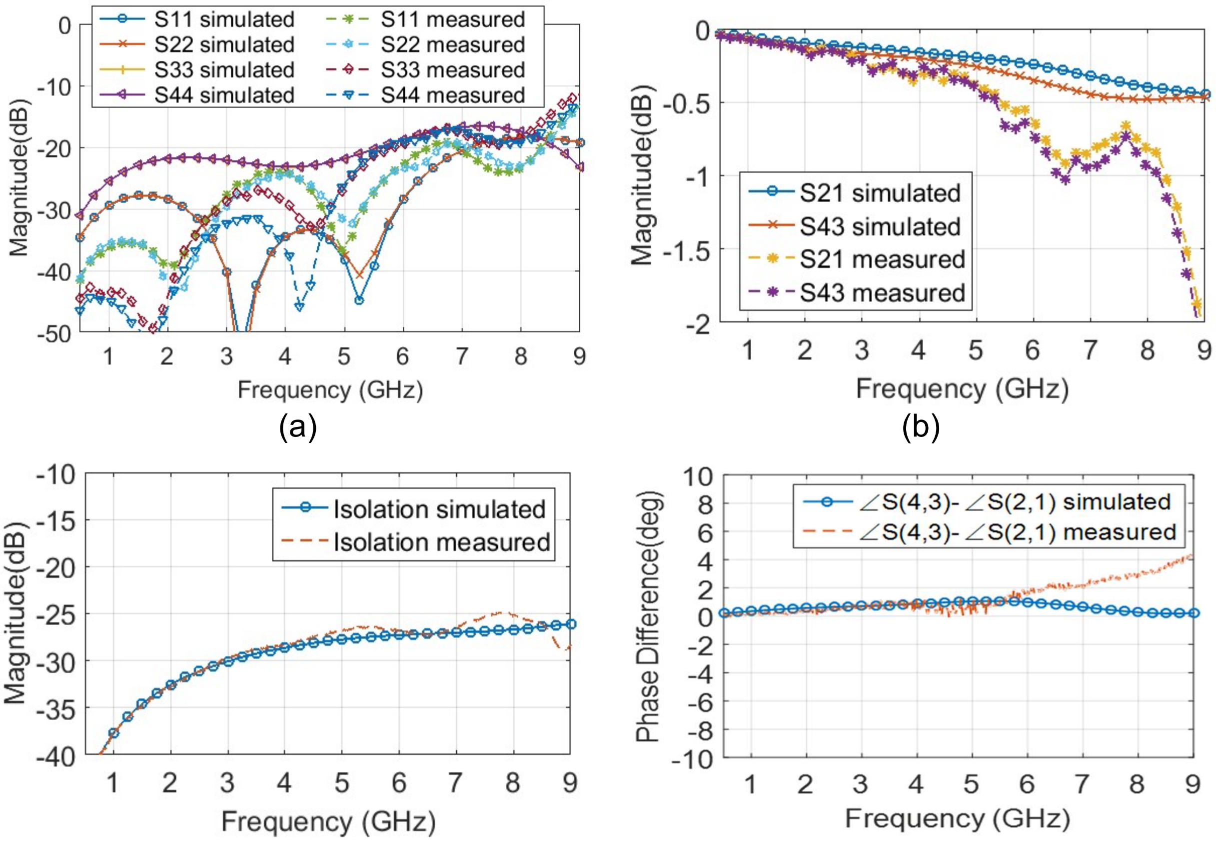

(a) (b)

(c) (d)

Figure 3.10. Simulated and measured results of crossover Design 1. (a) Return loss. (b) Insertion loss. (c) Isolation. (d) Phase difference between the two orthogonal paths.

To further improve the isolation of the crossover, the center conductor of coplanar waveguides was slightly tapered so that the middle part of the center conductor is narrower while the gap, s, was kept to be 0.16 mm, as 0.16 mm is close to the dimension limit of our milling machine. Figure 3.11 shows the schematic of the crossover design (*Design 2*) with the center conductor of the coplanar waveguides tapered, where the center conductor width, $w1$ is 0.8 mm while $w2$ is 1.2 mm. By tapering the center conductor, more electric fields would concentrate on the gaps between the center conductor and the ground planes on the layer as the center conductor, which would reduce the interference from the coplanar waveguide on the other side of the substrate and improve the isolation between the two coplanar waveguides.

The simulated and measured performances of the crossover with tapered center conductor on the coplanar waveguides are shown in Figure 3.12. The simulated return loss on each port is less than -20 dB throughout the 0.5–8 GHz frequency band. However, the measured return loss at around 4 GHz is about -15 dB. This could be due to the fabrication accuracy of the milling machine. The measured insertion loss is slightly higher at around 4 GHz correspond to the slightly higher return loss, overall the insertion loss is less than 1 dB in most cases from 0.5 to 8 GHz. The simulated and measured isolation between the two paths is improved as expected and it is improved by about 10 dB. The simulated and measured phase difference between the two paths is of less than 3°. Due to the slightly higher return loss and insertion loss at around 4 GHz in *Design 2*, crossover *Design 1* was chosen to be implemented in the Butler matrix design.

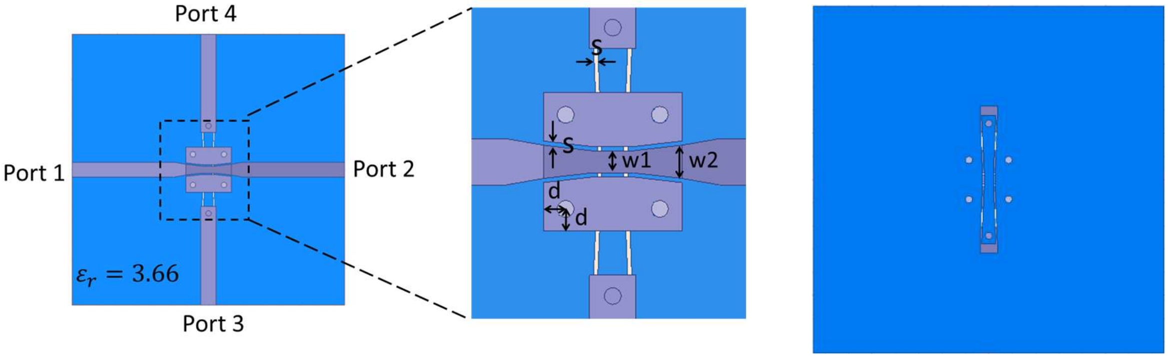

(a) (b)

Figure 3.11. Crossover Design 2: (a) Top view. (b) Bottom view.

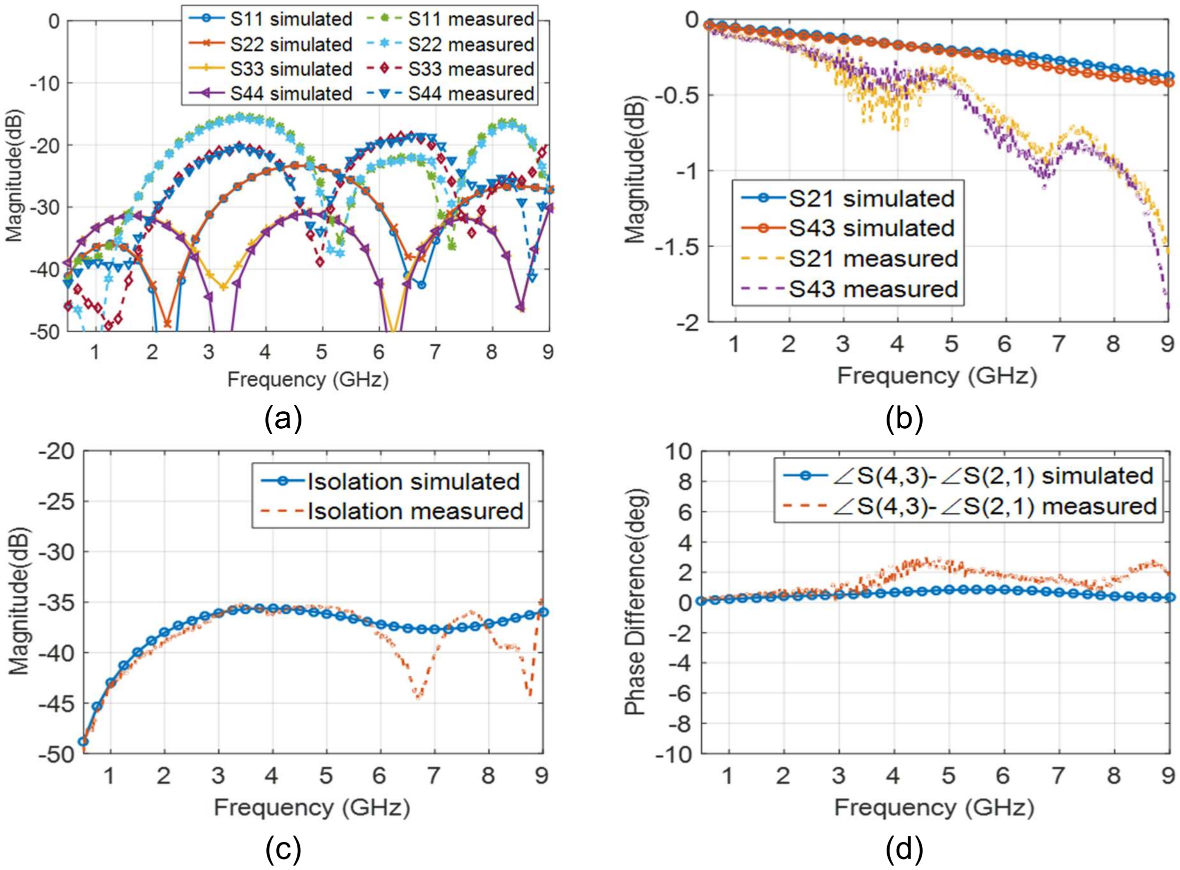

Figure 3.12. Simulated and measured results of crossover Design 2. (a) Return loss. (b) Insertion loss. (c) Isolation. (d) Phase difference between the two orthogonal paths.

3.2.1.3 Differential Phase Shifter

In the 8×8 Butler matrix design, three fixed phase shift values are required, which are 22.5°, 67.5°, and 45°. Phase shift can be easily achieved by changing the transmission line length. However, the phase shift produced by this method is frequency dependent and narrow band. To achieve wideband phase shift, Schiffman differential phase shifter was used for the Butler matrix implementation. Figure 3.13 shows the schematic of a standard Schiffman phase shifter. It consists of two transmission lines, one of them is folded and form a couple line section, the other one is the reference line.

The phase shift produced by a Schiffman phase shifter is the phase difference between the two transmission lines and it can be expressed as [70]:

$$\Delta\varphi = K\theta - \cos^{-1}\left(\frac{\rho - \tan^2\theta}{\rho + \tan^2\theta}\right) \tag{3.12}$$

where θ is the electrical length of the coupled line, K is the ratio of the electrical length of reference transmission line to the coupled line and ρ is the impedance ratio of the even and odd mode impedances of the coupled line and defined as

$$\rho = \frac{Z_{0e}}{Z_{0o}} \tag{3.13}$$

Z_{0e} and Z_{0o} are the even and odd mode impedances of the coupled lines. Z_{0e} and Z_{0o} can be calculated using commercial microwave simulation software, such as TXLINE in Microwave Office from National Instruments and LineCalc in ADS from Keysight.

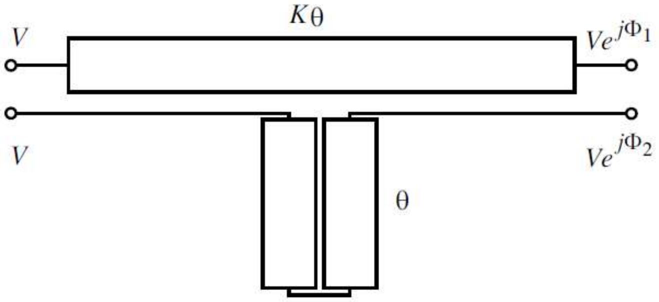

Figure 3.13. Schematic of a standard Schiffman phase shifter [70].

In Schiffman phase shifter design, the bandwidth of the phase shifter can be improved by dividing the coupled line into multiple sections with different characteristic impedance [71]. For the Butler matrix implementation, two-section Schiffman phase shifters were designed to provide 22.5°, 45°, and 67.5° phase shifts. The phase shifters were designed together with the crossovers to take into account the phase delay of the crossover. Figure 3.14a shows the simulation setup of the 22.5° and 67.5° phase shifters integrated with the crossovers. The dimensions of the transmission line length and the coupled line gap and impedance were adjusted such the phase shifters produce phase difference of the 22.5° and 67.5° corresponding to their reference transmission lines. The reference transmission line for 22.5° phase shifter is the one connecting ports 4 and 8 as illustrated in Figure 3.14a. The reference transmission line for 67.5° phase shifter is the one connecting ports 1 and 5. The simulated results of the 22.5° and 67.5° phase shifters are also shown in Figure 3.14. The simulated return loss is less than -19 in most of the ports. Ports 4 and 8 have return loss of less than -13.4 dB. The slightly higher return loss is due to the transmission line with a lot of right angle bends which introduce discontinuity in the transmission line. The simulated insertion loss of the phase shifters is less than 0.7

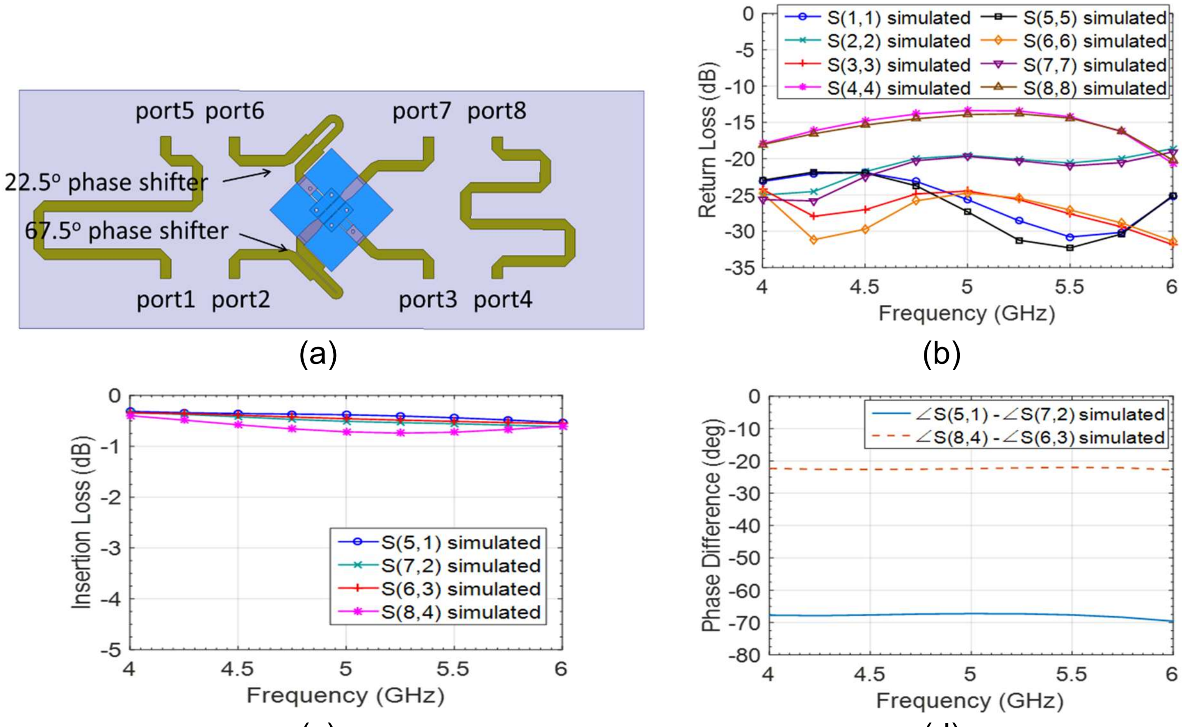

(a) (b)

(c) (d)

Figure 3.14. (a) Schematic of 22.5° and 67.5° two-section Schiffman phase shifter integrated with crossover. (b) Simulated return loss. (c) Simulated insertion loss. (d) Simulated phase shift.

dB. The degree of phase shifts is shown in Figure 3.14d, in which stable phase shifts of 22.4°±0.5° and 68.3°±1.2° are obtained across the 4–6 GHz band.

For the simulation setup of the 45° phase shifters as shown in Figure 3.15a, part of the model was cut out to reduce the simulation time as the schematic is symmetric. The simulated results of the 45° phase shifters are also shown in Figure 3.15 in which the simulated return loss and insertion loss are less than -16 dB and 1 dB respectively. The simulated phase shift is 45°±1.3° across the 4–6 GHz frequency band.

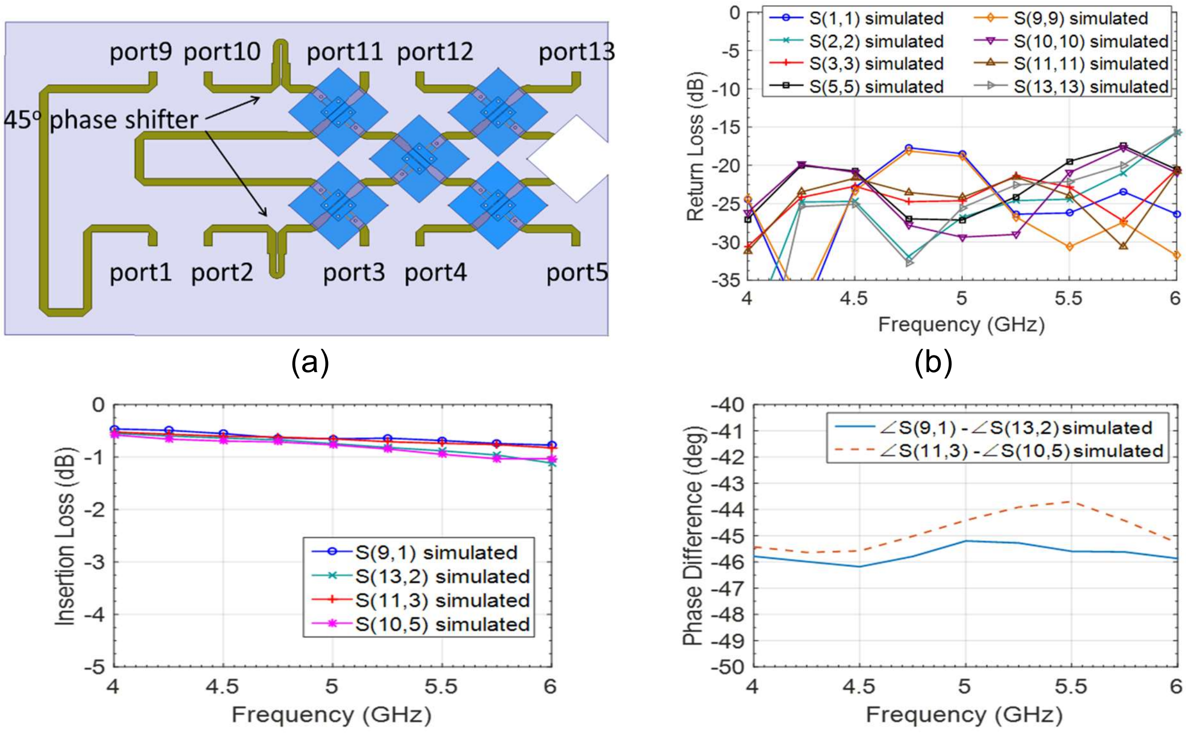

(a) (b)

(c) (d)

Figure 3.15. (a) Schematic of 45° two-section Schiffman phase shifter integrated with crossover. (b) Simulated return loss. (c) Simulated insertion loss. (d) Simulated phase shift.

The components (90° hybrid couplers, crossovers, and phase shifters) were integrated and form a microstrip-based 8×8 Butler matrix as shown in Figure 3.16. The overall size of the Butler matrix is 315 mm × 170 mm. Full-wave simulation of the 8×8

Butler matrix was performed in HFSS. The simulated return loss of the input and output ports of the Butler matrix are shown in Figure 3.17. The simulated transmission coefficients of each input port to the output ports and the phase shift on the output ports for each input port of the Butler matrix are illustrated in Figure 3.18 to Figure 3.25. The simulated return loss of the input and output ports are below -10 dB over the 4–6 GHz band. The simulated transmission coefficients of each input port to the output ports are within the range of -10 dB to -14 dB in most of the cases. In ideal case, if the 8×8 Butler matrix is lossless, the transmission coefficient from the input ports to the output ports would be -9 dB. Thus, the simulated insertion loss of the 8×8 Butler matrix is 3 dB ± 2 dB. The simulated phase shift on the output ports for each input port of the Butler matrix are also summarized in Table 3.2 and compared with the theoretical values. The simulated phase shifts on the output ports are close to the theoretical values and with variations within ±15°.

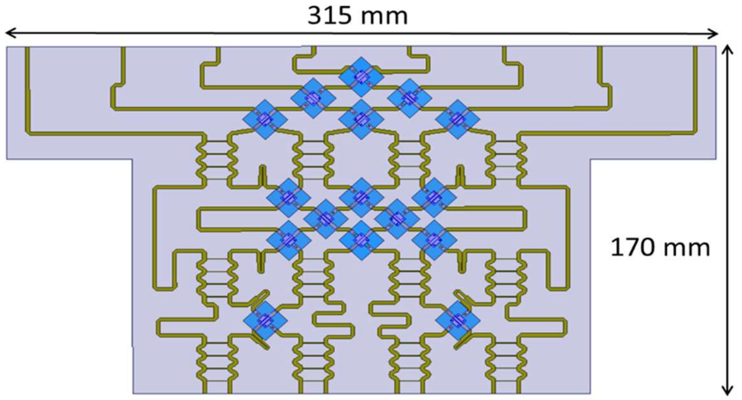

Figure 3.16. Microstrip implementation of the Butler matrix beam-switching feed network.

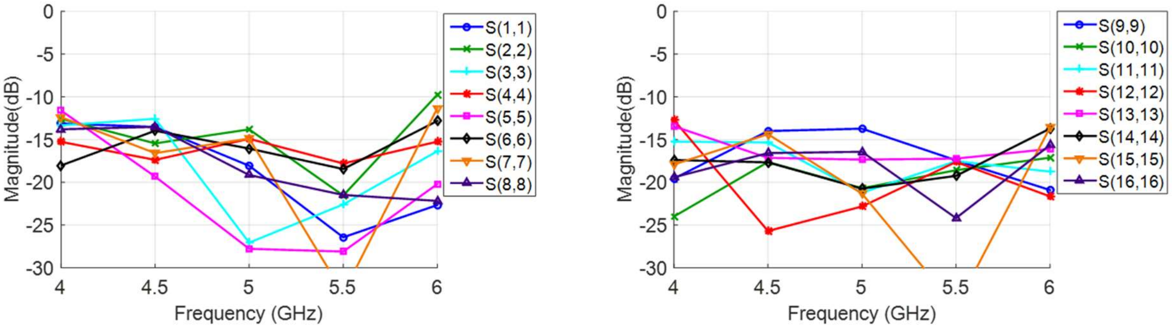

(a) (b)

Figure 3.17. 8×8 Butler matrix simulation results: (a) Return loss on the input ports. (b) Return loss on the output ports.

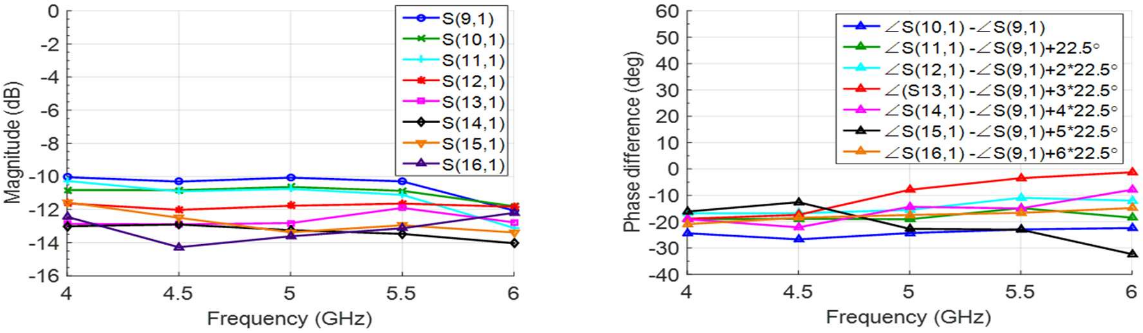

(a) (b)

Figure 3.18. 8×8 Butler matrix simulation results: (a) Insertion loss of port 1. (b) Phase shift in the output ports while exciting port 1.

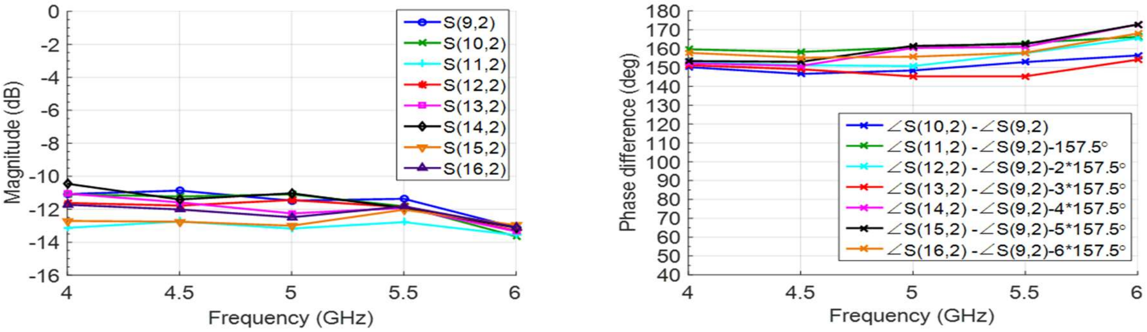

(a) (b)

Figure 3.19. 8×8 Butler matrix simulation results: (a) Insertion loss of port 2. (b) Phase shift in the output ports while exciting port 2.

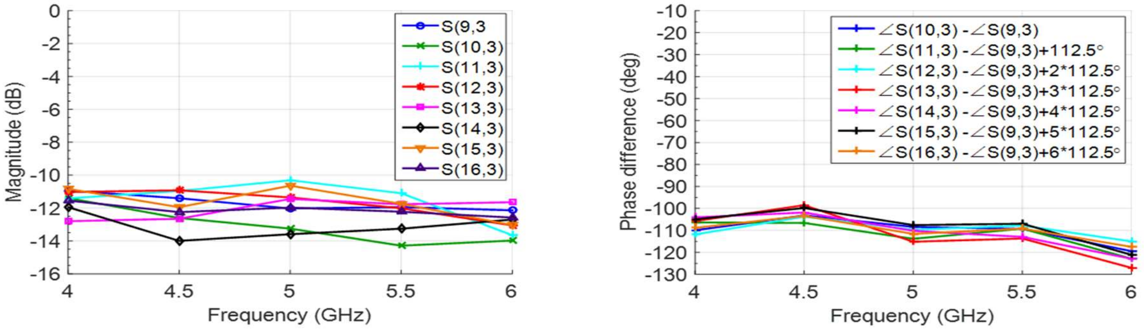

(a) (b)

Figure 3.20. 8×8 Butler matrix simulation results: (a) Insertion loss of port 3. (b) Phase shift in the output ports while exciting port 3.

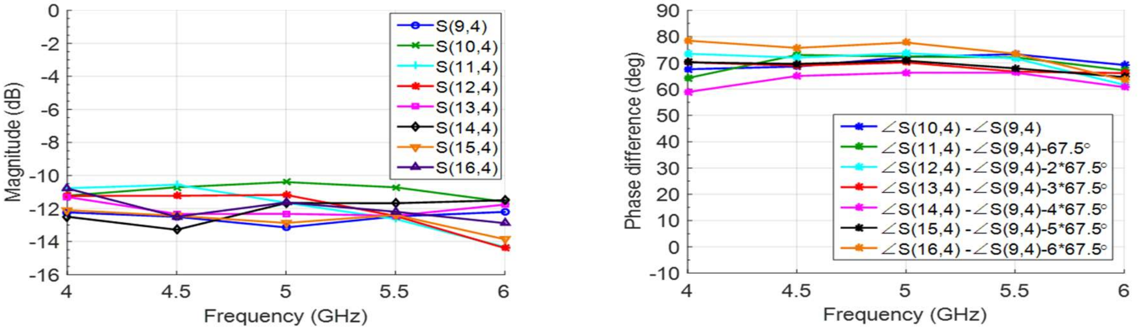

(a) (b)

Figure 3.21. 8×8 Butler matrix simulation results: (a) Insertion loss of port 4. (b) Phase shift in the output ports while exciting port 4.

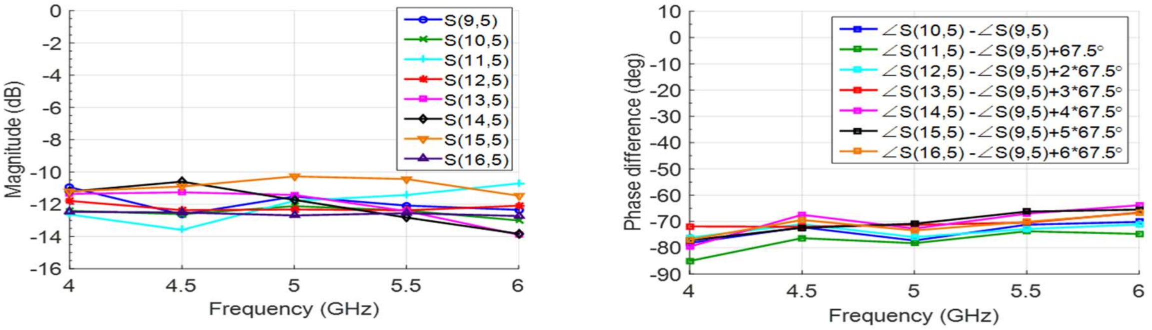

(a) (b)

Figure 3.22. 8×8 Butler matrix simulation results: (a) Insertion loss of port 5. (b) Phase shift in the output ports while exciting port 5.

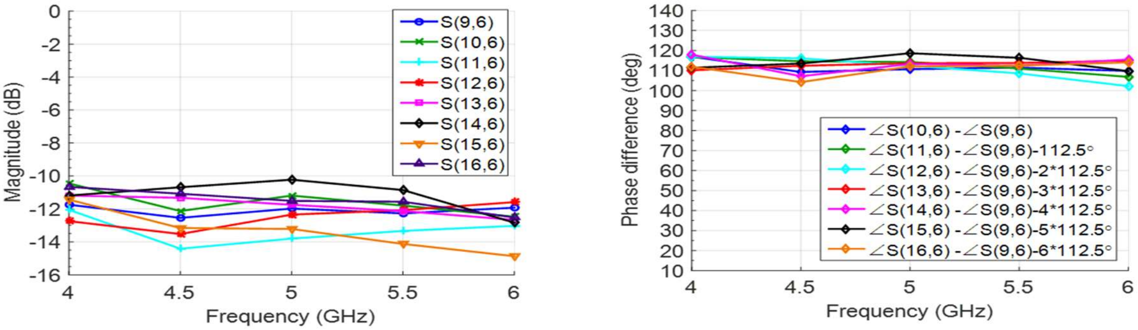

(a) (b)

Figure 3.23. 8×8 Butler matrix simulation results: (a) Insertion loss of port 6. (b) Phase shift in the output ports while exciting port 6.

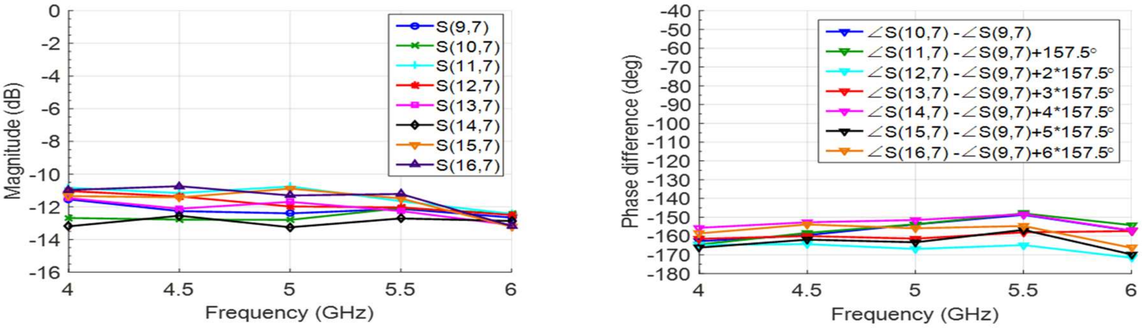

(a) (b)

Figure 3.24. 8×8 Butler matrix simulation results: (a) Insertion loss of port 7. (b) Phase shift in the output ports while exciting port 7.

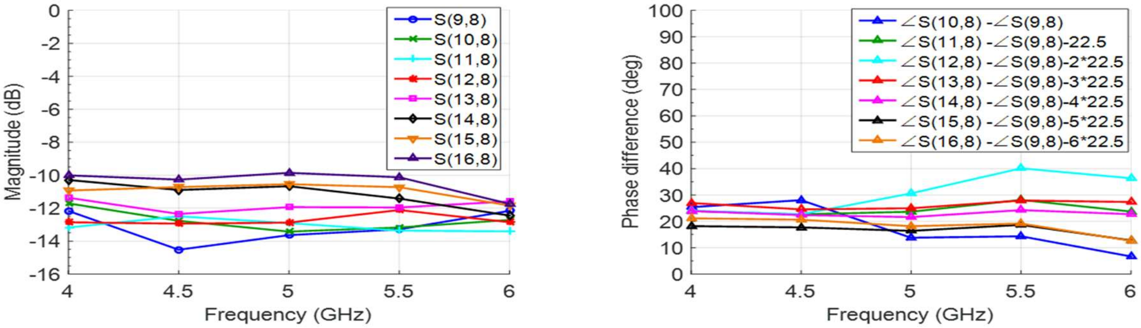

(a) (b)

Figure 3.25. 8×8 Butler matrix simulation results: (a) Insertion loss of port 8. (b) Phase shift in the output ports while exciting port 8.

The 8×8 Butler matrix design was fabricated using the milling machine in our lab and experimentally characterized. The fabricated Butler matrix prototype and its measured results are shown in Figure 3.26 to Figure 3.35. Overall, the measured results agree with the simulated results. The measured return loss of the input and output ports are below -10 dB. The measured insertion loss is around 3±2 dB. The measured phase shift on the output ports are close to the simulated results. However, the measured phase shift has slightly larger variations compares to the simulated results: the measured results have variations of ±20° and the simulated results have variations of ±15°. The measured phase shift results are also summarized in Table 3.2 for comparison with the simulated phase shift results as well as the theoretical values for each input port of the 8×8 Butler matrix.

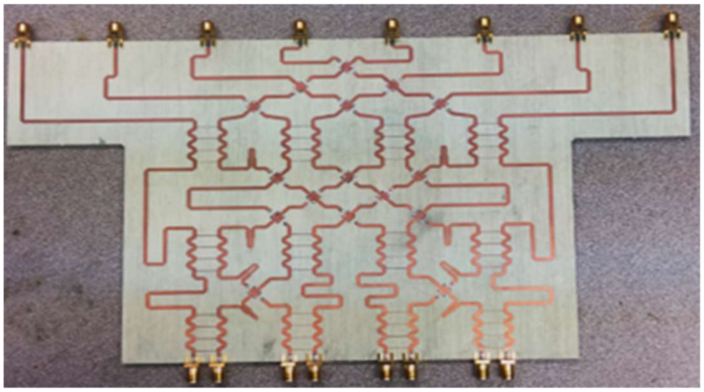

Figure 3.26. Fabricated prototype of the 8×8 Butler matrix.

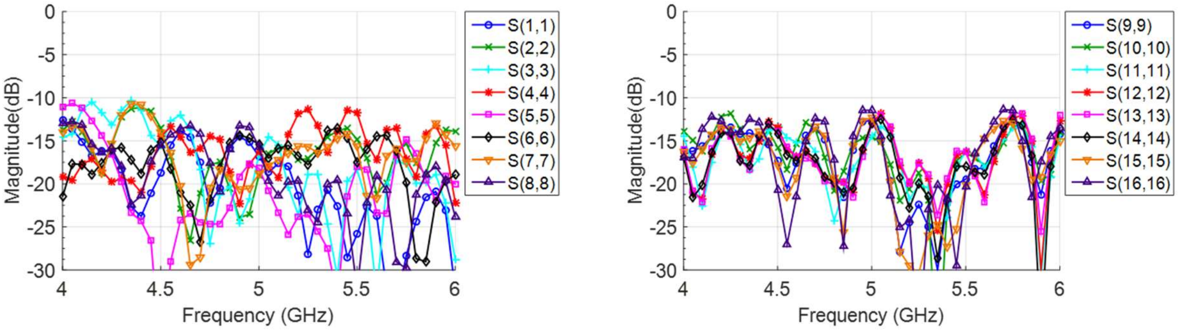

(a) (b)

Figure 3.27. 8×8 Butler matrix measurement results: (a) Return loss on the input ports. (b) Return loss on the output ports.

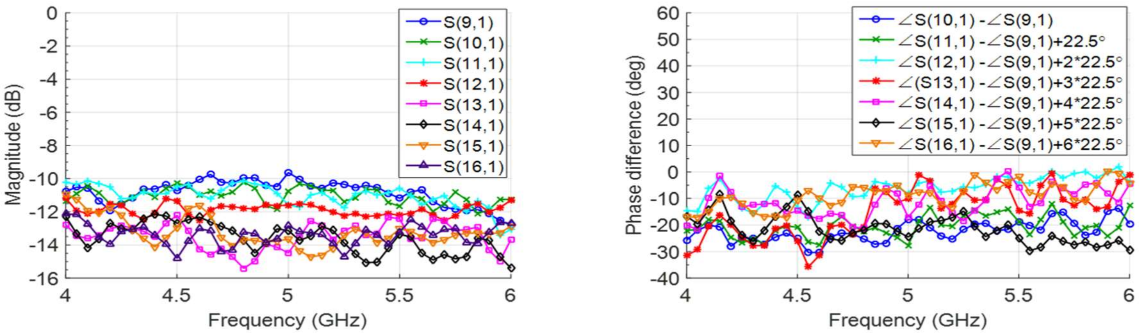

(a) (b)

Figure 3.28. 8×8 Butler matrix measurement results: (a) Insertion loss of port 1. (b) Phase shift in the output ports while exciting port 1.

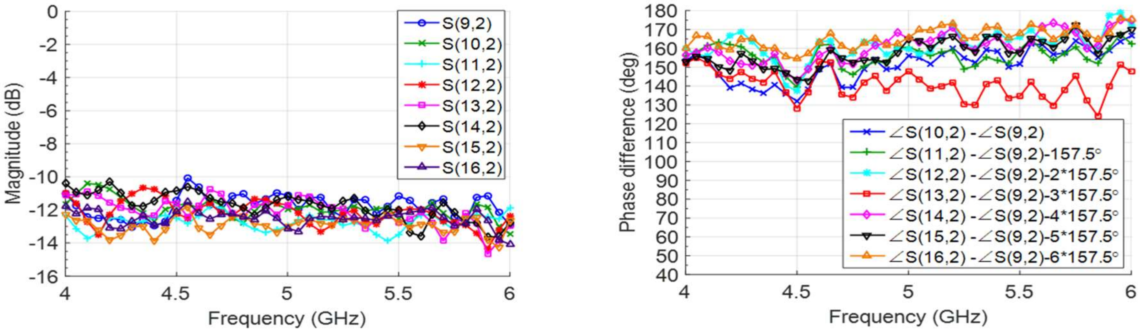

(a) (b)

Figure 3.29. 8×8 Butler matrix measurement results: (a) Insertion loss of port 2. (b) Phase shift in the output ports while exciting port 2.

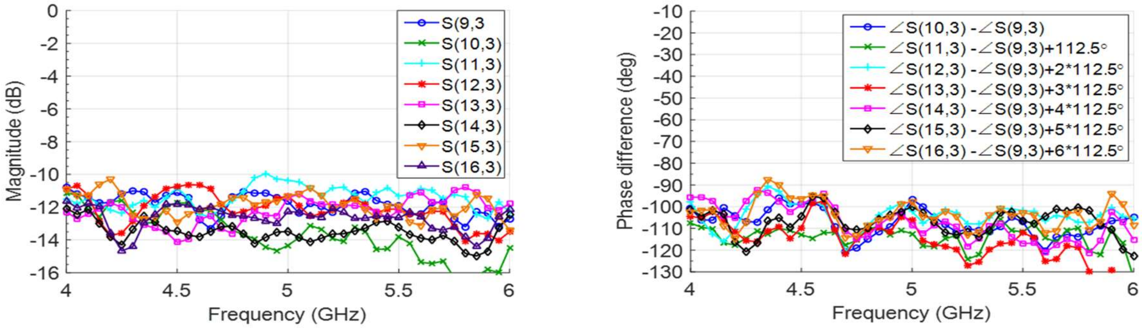

(a) (b)

Figure 3.30. 8×8 Butler matrix measurement results: (a) Insertion loss of port 3. (b) Phase shift in the output ports while exciting port 3.

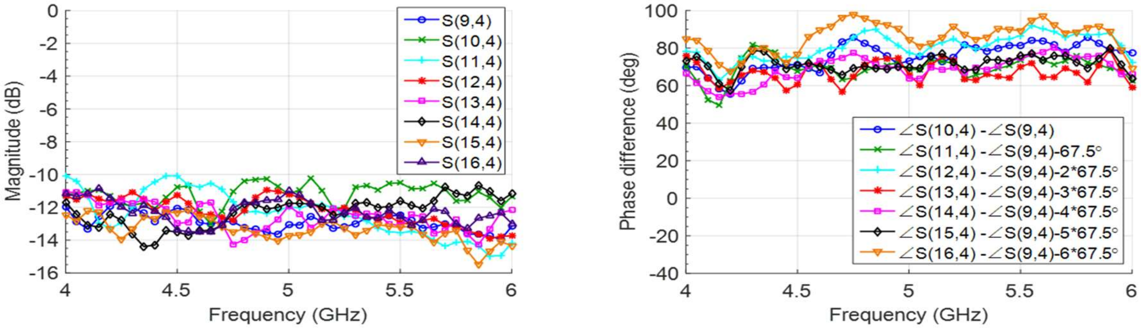

(a) (b)

Figure 3.31. 8×8 Butler matrix measurement results: (a) Insertion loss of port 4. (b) Phase shift in the output ports while exciting port 4.

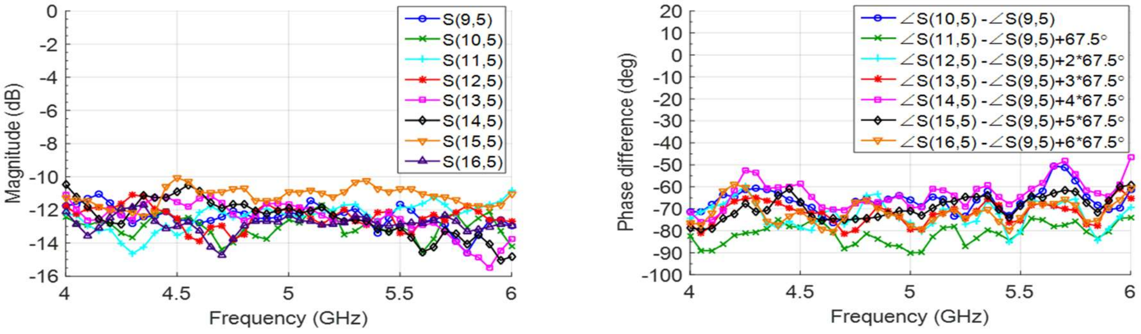

(a) (b)

Figure 3.32. 8×8 Butler matrix measurement results: (a) Insertion loss of port 5. (b) Phase shift in the output ports while exciting port 5.

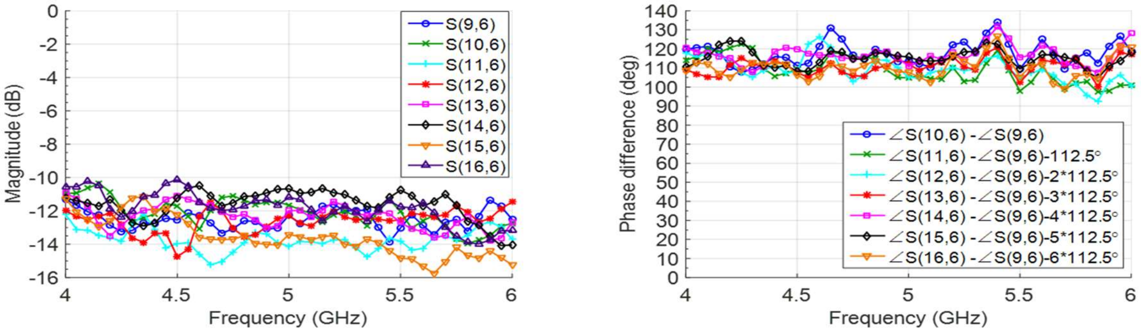

(a) (b)

Figure 3.33. 8×8 Butler matrix measurement results: (a) Insertion loss of port 6. (b) Phase shift in the output ports while exciting port 6.

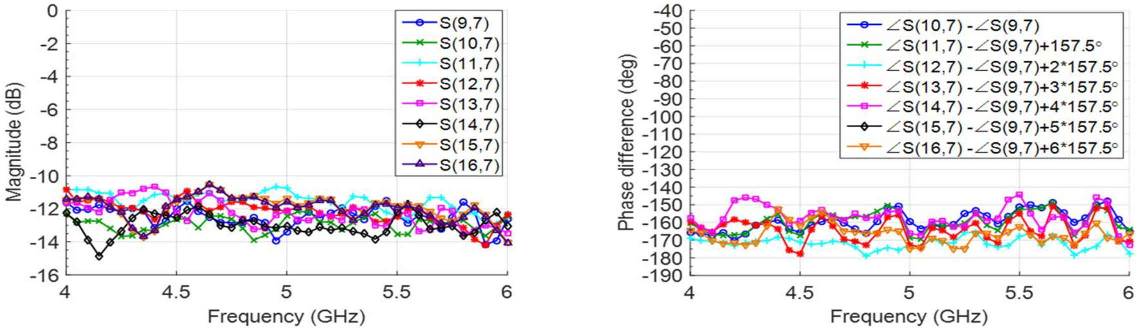

(a) (b)

Figure 3.34. 8×8 Butler matrix measurement results: (a) Insertion loss of port 7. (b) Phase shift in the output ports while exciting port 7.

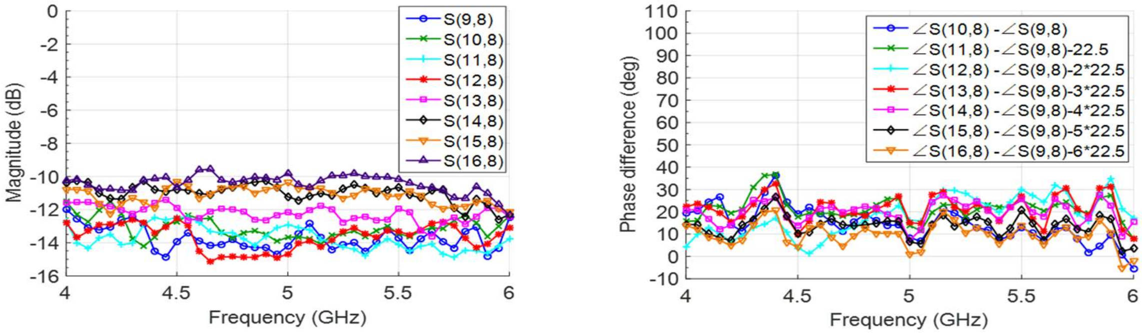

(a) (b)

Figure 3.35. 8×8 Butler matrix measurement results: (a) Insertion loss of port 8. (b) Phase shift in the output ports while exciting port 8.

Table 3.2. Comparison Table Between the Theoretical, Simulated, and Measured Linear Phase Shift in the Output Ports for Each Input Port of the Butler Matrix.

Input Port	1	2	3	4	5	6	7	8
Theoretical	-22.5°	157.5°	-112.5°	67.5°	-67.5°	112.5°	-157.5°	22.5°
Simulated	-16° ±15°	160° ±15°	-112° ±15°	69° ±10°	-73° ±10°	-110° ±10°	-160° ±12°	22° ±15°
Measured	-15° ±15°	155° ±20°	-110° ±20°	72° ±20°	-70° ±20°	-115° ±15°	-160° ±20°	20° ±20°

3.3 Digital Beamforming

In digital beamforming, the operations of phase shifting and amplitude scaling for each antenna element are done digitally in the baseband or intermediate frequency (IF) level by multiplying the signal with a complex weight. Due to the signals and complex weight are represented in digital format, digital beamforming provides more freedoms in controlling the phase and amplitude of the signals, which allows desired and complicated radiation patterns to be synthesis easily, such as radiation patterns with lower sidelobe level, patterns with multiple beams, and patterns with a null in the direction of interference sources. The computation resources in digital beamforming system also allows realization of other advanced features, such as angle of arrival (AoA) estimation and adaptive beamforming algorithm implementation. Figure 3.36 shows the block diagram of a 4-channel digital beamforming receiver. The RF signal from each antenna is down-converted to baseband level (or IF level) and sampled by an analog to digital converter. Each sampled signal is multiplied by a complex weight. The results from the channels are summed to produce one baseband signal (or IF signal) with directional properties. The output of a digital beamforming receiver can be expressed as:

$$y(k) = \sum_{n=1}^{N=4} S_n(k) W_n \tag{3.14}$$

where $S_n(k)$ is the sampled down-converted signal from each channel, W_n is the complex weight for each channel and N is the total number of channels.

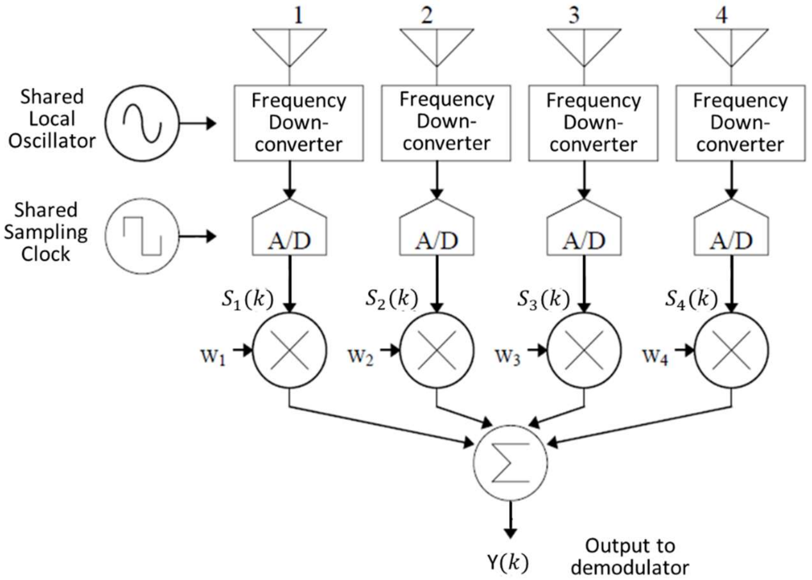

Figure 3.36. Digital beamforming receiver block diagram.

3.3.1 Pattern Synthesis for Linear Arrays

There are many methods available to synthesize a radiation pattern or determine the complex weight values for a desired radiation pattern, such as Fourier transform method, Woodward synthesis method, and Dolph-Chebyshev synthesis method [72], [73]. Among these methods, Fourier transform is the simplest method. For a linear antenna array with uniform element spacing, the radiation pattern can be expressed as [72]:

$$F(u) = \sum W_n e^{j\frac{2\pi}{\lambda}*u*n*d_x} \tag{3.15}$$

where

$$-\frac{N-1}{2} \leq n \leq \frac{N-1}{2}, n = \pm\frac{1}{2}, \pm\frac{3}{2}, \pm\frac{5}{2}, \ldots$$

N is the total number of elements or channels, d_x is the antenna element spacing, W_n is the Fourier series coefficient or weight, and u represents the radiation pattern in u-space.

Thus, given a desired radiation pattern $F(u)$, its corresponding weight values or Fourier series coefficient can be calculated as:

$$W_n = \frac{d_x}{\lambda}\int_{-\frac{\lambda}{2d_x}}^{\frac{\lambda}{2d_x}} F(u)e^{-j\frac{2\pi}{\lambda}*u*n*d_x}\,du \tag{3.16}$$

The calculated weight for the synthesized pattern can be verified by using the array factor equation (3.3). Examples of radiation pattern synthesis using Fourier series approximation are shown in Figure 3.37. The ideal pulse-shape patterns with different beamwidth and beam number were synthesized in an eight-element linear array using Fourier series approximation. The calculated weights were plugged into (3.3) to generate the synthesized patterns. The synthesized patterns match well with the pulse-shape patterns in terms of beamwidth and beam directions.

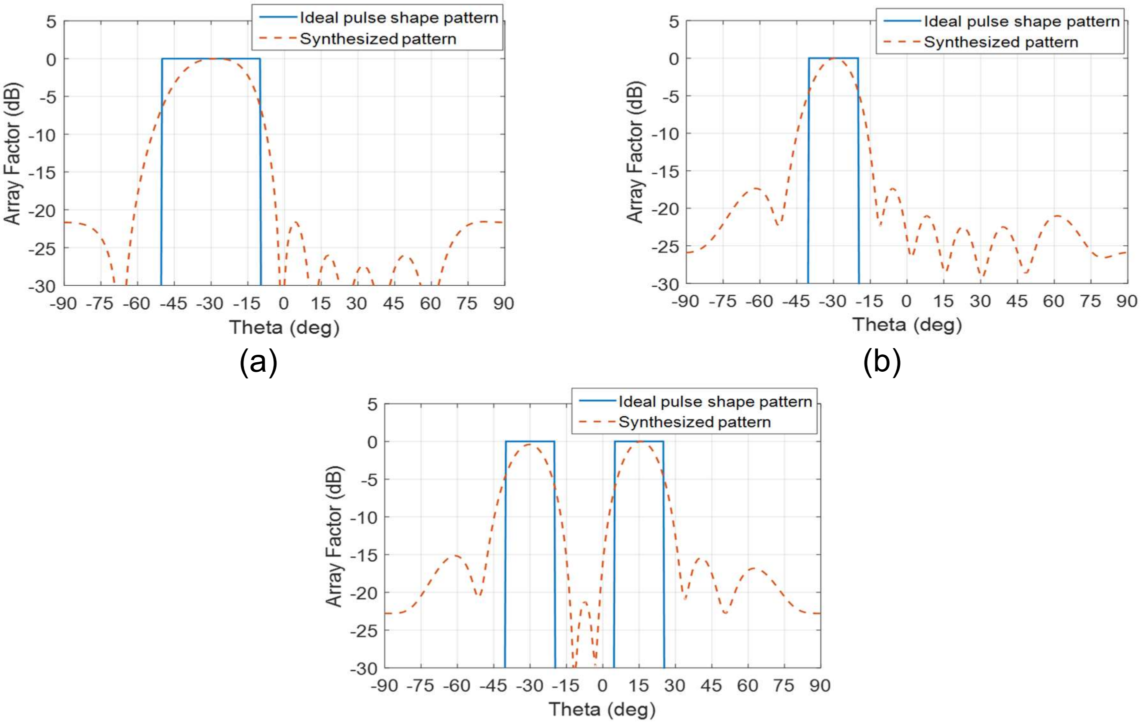

(a)

(b)

(c)

Figure 3.37. Fourier series synthesized representation of pulse-shaped patterns in an eight-element array.

3.3.2 Angle of Arrival

Angle of arrival for a radio signal can be estimated using various of methods and algorithms, such as adaptive beamforming algorithms, multiple signal classification (MUSIC) algorithm, and Capon’s minimum variance method [74], [75]. Adaptive beamforming algorithms adjust the complex weights on-the-fly to maximize the quality of the communication channel and generally require less computational resources compared to other methods based on singular value decomposition or eigenvalue decomposition. Least mean squares (LMS) algorithm is one of the commonly used adaptive beamforming algorithm. Figure 3.38 shows the block diagram of a digital beamforming receiver with LMS algorithm. A feedback loop is used to update the weights accordingly. The output signal of the beamforming receiver is compared with a desired signal, the weights are updated based on the difference between the two signals recursively to minimize the difference. The LMS weight updating equation is given by

$$W(k+1) = W(k) + \mu S^*(k)e(k) \tag{3.17}$$

where

$$e(k) = d(k) - S^T(k)W(k) \tag{3.18}$$

μ is the step size.

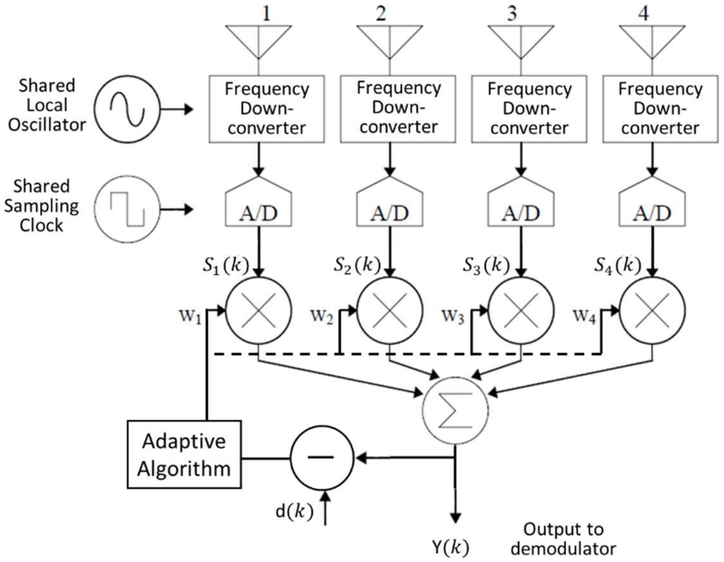

Figure 3.38. Digital beamforming receiver block diagram with LMS adaptive algorithm.

3.3.3 Digital Beamforming Transceiver

While the Butler matrix can be used to switch the main beam of the antennas for the proposed directional networking system, the advanced features in digital beamforming are attractive for tracking the mobile users and providing optimal radiation pattern that changes adaptively based on the location and movement of the mobile users. In the study of hybrid smart antenna array using highly directional antenna elements [74] by our colleague, an eight-channel digital beamforming receiver was built. For the purpose of testing the beamforming algorithms, a four-channel digital beamforming transmitter was added to the system so that it can support both transmitting and receiving. Figure 3.39a shows the block diagram of the transceiver design in which the transmitter chain contains the newly added components and the receiver chain has the components from [74]. In the transceiver system, a 4-channel 14-bit DAC and an 8-channel 12-bit ADC cards are installed on a PC and controlled by Matlab. The maximum sample rate of the DAC and ADC card are 60 MS/s and 25 MS/s, respectively. The PC is responsible for signal processing, AoA estimation, and generating signals for the DAC card. The RF front end in the transmitter and receiver chains is responsible for frequency down convert and up convert. In the current system setup, the RF front end of the system support frequency up convert and down convert at 2.4 GHz. Figure 3.39b shows the photo of the digital transceiver system with monopole antenna arrays.

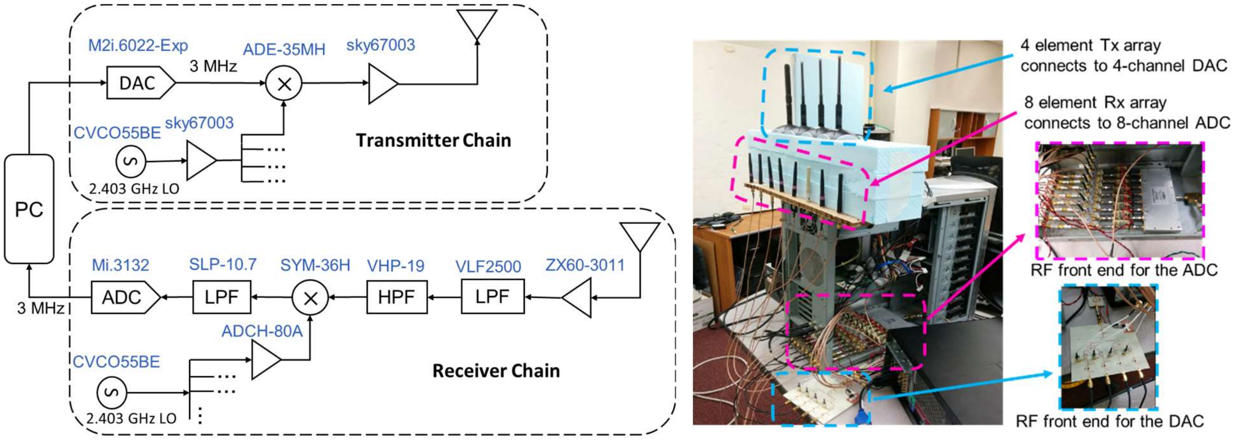

(a) (b)

Figure 3.39. Digital beamforming transceiver. (a) Block diagram. (b) Picture of the system with antenna setup.

The digital transceiver system can be used for testing the AoA estimation and beamforming algorithms, as well as their compatibility with the communication protocols. Currently the LMS algorithm is implemented in the transceiver system so that it can track and send the signal back to the direction of the communicating source. The operation procedure for the transceiver system is described below:

1. Acquire data from each channel of the ADC card.
2. Estimate the AoA information using LMS algorithm.
3. Generate continuous wave signal for each channel of the DAC based on the estimated AoA, so that the transmitter beamform to the AoA direction.

4. Send data to DAC for transmission.
5. Repeat the procedures for every half second.

Preliminary measurements were performed to verify the performance of the transceiver system and the LMS algorithm. In the measurement, two horn antennas were used, one of the horn antenna (Tx) was connected to a signal generator that output a continuous wave signal at 2.406 GHz, while the other horn antenna (Rx) was connected to a spectrum analyzer to measure the received signal power level. Figure 3.40 shows one of the measurement setup and the measured result, which the Tx horn was fixed at 30° while the Rx horn is moving in a constant radius with step size of 10°. The measured result shows the transceiver was able to correctly estimated the AoA information of the source and beamform the radiation pattern to 30° angle. Figure 3.41 show another measurement setup and its corresponding result, which the Tx horn and Rx horn were fixed at 0° while rotating the antenna arrays connected to the digital transceiver. Stable signal level was obtained at around ±30°. It indicates that the transceiver was able to track the source at different angles and beamform to the direction of the source.

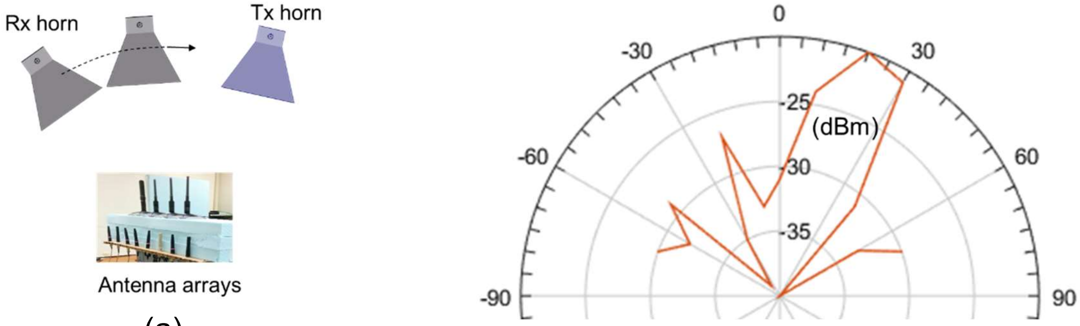

(a) (b)

Figure 3.40. Digital transceiver measurement with Tx horn fixed at 30° while the Rx horn is moving in a constant radius. (a) Measurement setup. (b) Measured result.

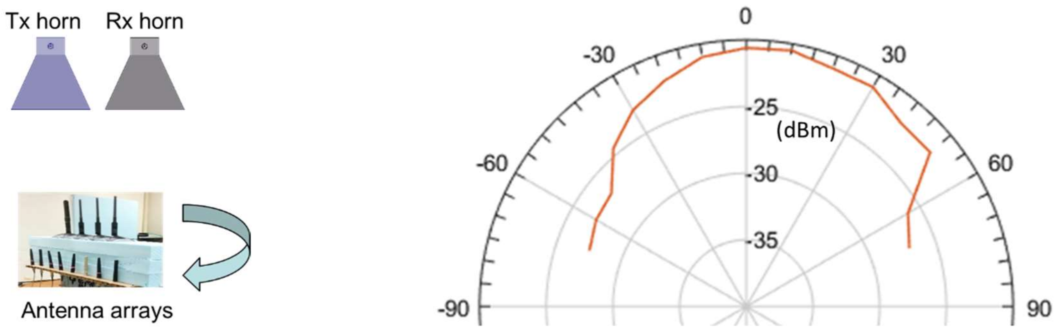

(a) (b)

Figure 3.41. Digital transceiver measurement with Tx horn and Rx horn fixed at 0° while rotating the antenna arrays connected to the digital transceiver. (a) Measurement setup. (b) Measured result.

CHAPTER 4

ANTENNA ARRAY PROTOTYPES AND EXPERIMENTAL MEASUREMENTS

In the previous chapters, three antenna arrays and an 8×8 Butler matrix were designed. This chapter covers the measured results of the antenna arrays in the broadside direction as well as the beam-switching results while the antenna array is connected to the Butler matrix. The antenna arrays were fabricated in our lab using milling machine and the measurements were done in the anechoic chamber at University of Hawaii at Manoa.

In the measurement setup, the antenna under test (AUT) was set as a receiver and a linearly polarized horn antenna was set as a transmitter. To measure the radiation characteristics (gain and axial ratio) of a circularly polarized antenna, phase-amplitude method [23], [76] was used with two measurements performed using the horn antenna in the orientation angle of 0° (for E_θ) and 90° (for E_ϕ). The E_{RHCP}, E_{LHCP} and the axial ratio (AR) can be calculated as:

$$E_{RHCP} = \frac{1}{\sqrt{2}}(E_\theta + jE_\phi) \tag{4.1}$$

$$E_{LHCP} = \frac{1}{\sqrt{2}}(E_\theta - jE_\phi) \tag{4.2}$$

$$AR = \left|\frac{|E_{RHCP}| + |E_{LHCP}|}{|E_{RHCP}| - |E_{LHCP}|}\right| \tag{4.3}$$

where $j^2 = -1$.

4.1 Broadside Radiation Pattern Measurement

In measuring the broadside radiation pattern, an 8-way power divider was used to feed the antenna arrays so that all the subarrays were fed in the same phase. Figure 4.1 shows the fabricated circularly polarized 4×8 LSA array. The measured results are shown in Figure 4.2Figure 4.4 together with the simulated results.

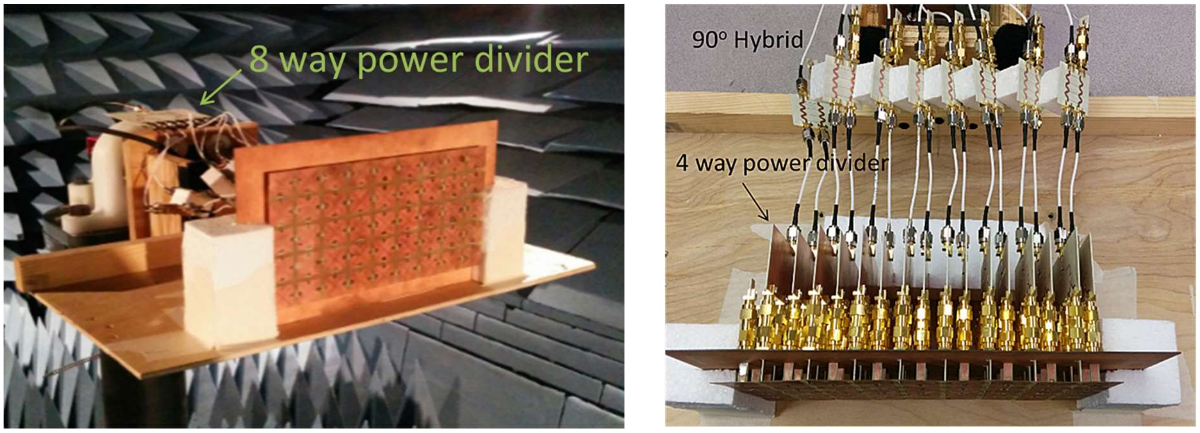

(a) (b)

Figure 4.1. Fabricated 4×8 LSA array. (a) Isometric view. (b) Top view.

Figure 4.2 shows the measured results of the return loss and RHCP gain of the 4×8 LSA array. The measured return loss is below -10 dB across the 4-6 GHz band, which agrees well with the simulated result. There are additional resonances in the measured data which are due to additional cable length in the feeding network as coaxial cables were used to connect the power dividers and the 90° hybrid couplers. The measured RHCP gain agrees well with the simulated gain: the measured gain ranges from 15.5 to 18 dBic and the simulated gain ranges from 15.5 to 19 dBic. The measured axial ratio of the LSA array is shown in Figure 4.3. Decent axial ratios on the broadside direction are obtained in both measurement and simulation. In both cases, the axial ratios are below 1.8 dB across the frequency band of interest. The measured RHCP and the cross-polarization radiation patterns in x-z plane and y-z plane at different frequencies are shown in Figure 4.4. In the x-z plane, the 3-dB beamwidth ranges from 19° to 13° from 4 to 6 GHz. In the y-z plane, the 3-dB beamwidth ranges from 34° to 26°. The side lobe level of the radiation patterns is less than -14 dB. Good cross-polarization level is obtained, which is more than 20 dB in the broadside direction.

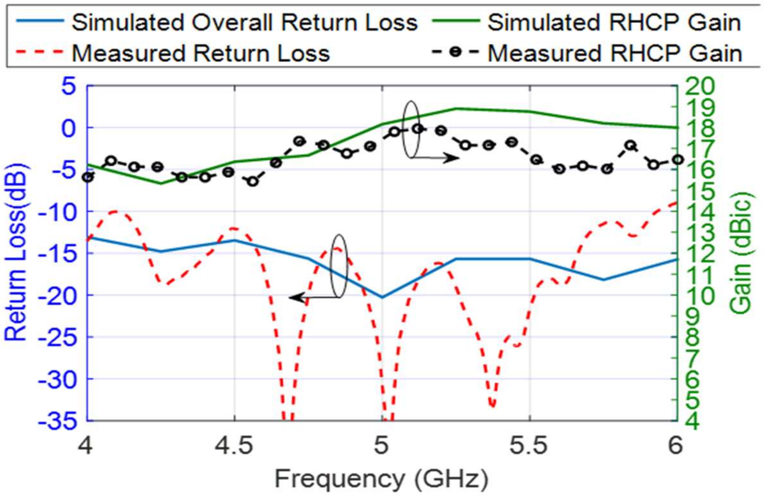

Figure 4.2. Measured and simulated return loss and RHCP gain of the 4×8 LSA array.

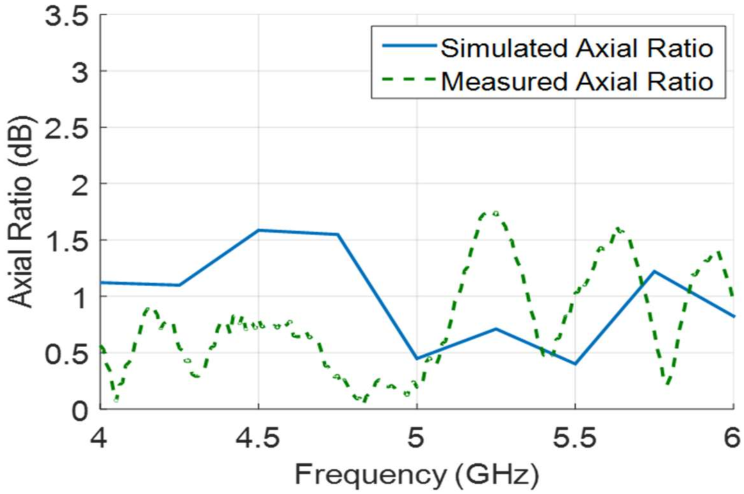

Figure 4.3. Measured and simulated axial ratio of the 4×8 LSA array.

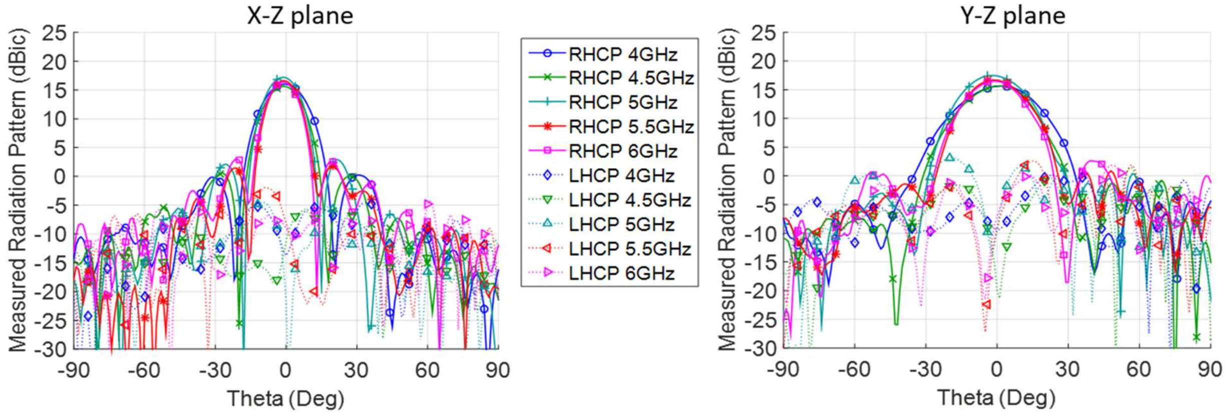

Figure 4.4. Measured radiation pattern of the 4×8 LSA array in x-z plane and y-z plane.

Figure 4.5 shows the fabricated 4×8 dual-fed stacked patch antenna array. The measured return loss and RHCP gain of the stacked patch antenna array are shown in Figure 4.6. Both measured and simulated return losses are less than 10 dB from 4.5 to 5 GHz. The measured RHCP gain ranges from 17 to 19 dBic while the simulated RHCP gain ranges from 20 to 21.5 dBic. There are several dB decreases in the measured gain at upper frequency end compare to the simulated gain as illustrated in Figure 4.6. The decrease in gain at the upper frequency end could be due to fabrication errors. Specifically, the antenna array, had a very small gap (order of 0.2 mm) in between the stacked substrates (due to the solder on top of the driven patches), which resulted in the aforementioned errors. The measured axial ratio shown in Figure 4.7 is below 1 dB and agrees with the simulated values. The measured RHCP and LHCP radiation patterns in the x-z and y-z planes are shown in Figure 4.8. The RHCP radiation patterns have 3-dB beamwidth range from 10° to 9° from 4.5 to 5 GHz in the x-z plane. In the y-z plane, the 3-dB beamwidth of the radiation patterns ranges from 20° to 18°. The side lobe level of the measured patterns in both planes are less than -10 dB with cross-polarization level of more than 20 dB.

(a) (b)

Figure 4.5. Fabricated 4×8 dual-fed stacked patch antenna array. (a) Isometric view. (b) Back view.

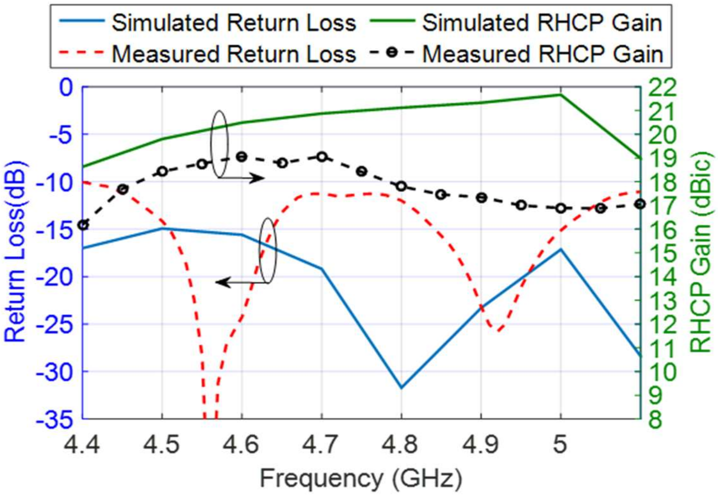

Figure 4.6. Measured and simulated return loss and RHCP gain of the 4×8 dual-fed stacked patch antenna array.

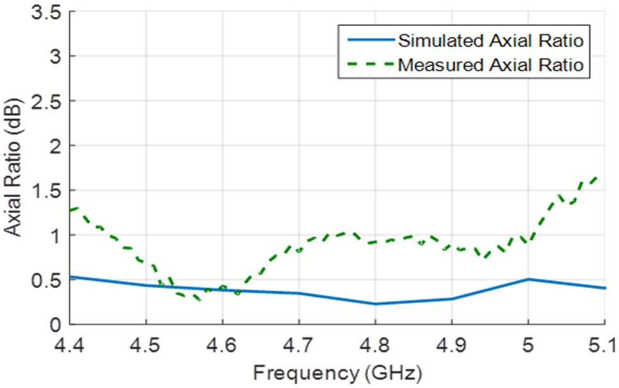

Figure 4.7. Measured and simulated axial ratio of the 4×8 dual-fed stacked patch antenna array.

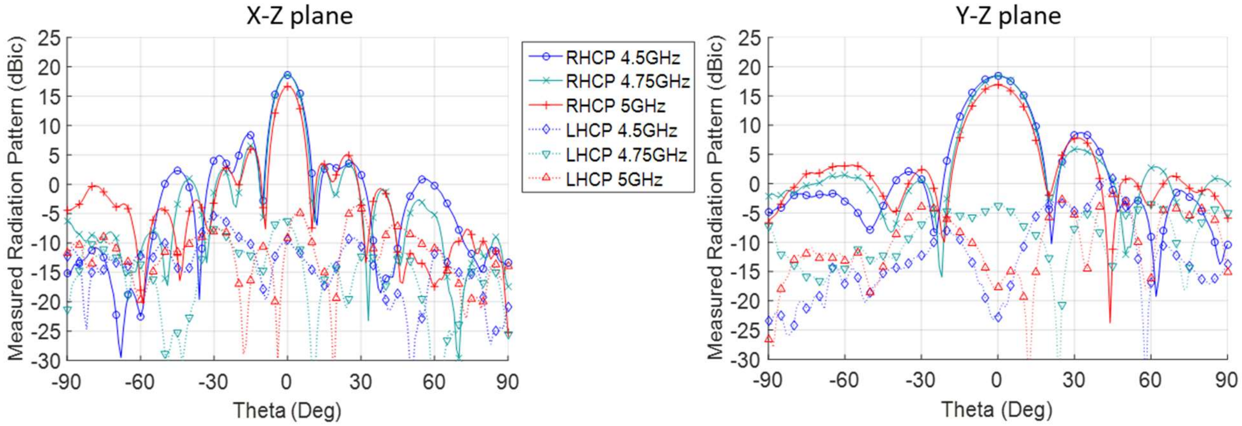

Figure 4.8. Measured radiation pattern of the 4×8 dual fed stacked patch antenna array in the x-z plane and y-z plane.

The fabricated 8×8 dual-fed stacked patch antenna array with annular gaps is shown in Figure 4.9. The broadside radiation measurement results of the antenna array are shown in Figure 4.10–Figure 4.12. In the frequency range of 4.4–5.2 GHz, the measured return loss is less than -10 dB. The measured RHCP gain ranges from 21 to 23.7 dBic which is slightly lower than the simulated gain due to the losses from the cable and power divider feeds. After the post-processing of measured data and removing of additional insertion losses due to cable and power divider feeds, the measured gain matched very well with the simulated gain, as shown in Figure 4.6. The measured axial ratio is less than 1.6 dB over the 4.4–5.2 GHz band and it agrees well with the simulated axial ratio. The measured RHCP and LHCP radiation patterns in the x-z and y-z planes are shown in Figure 4.12. The RHCP radiation patterns have 3-dB beamwidth range from 10° to 9° from 4.4 to 5.2 GHz in both planes. The side lobe levels of the measured patterns in both planes are less than -10 dB with cross-polarization level of more than 20 dB. Table 4.1 summarizes the radiation characteristic of the three antenna arrays in the broadside direction.

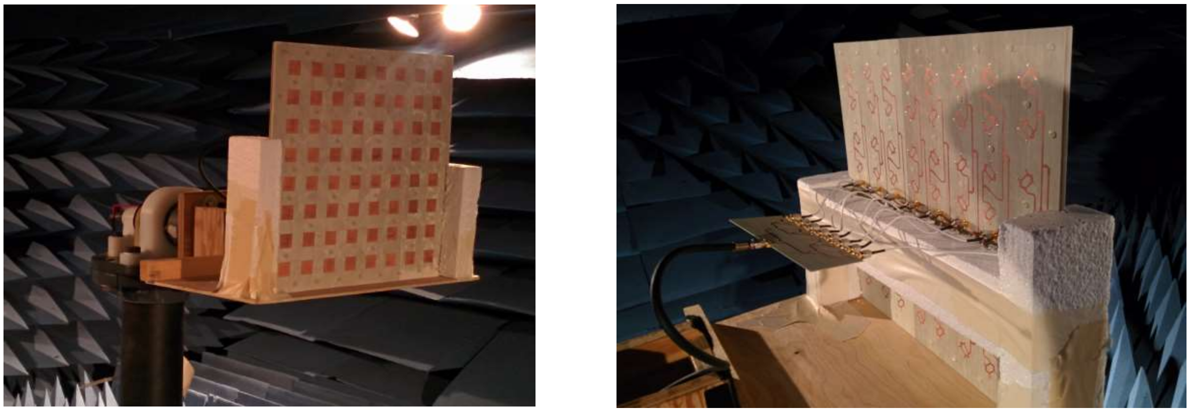
(a) (b)

Figure 4.9. 8×8 stacked patch antenna array with annular gaps. (a) Front view. (b) Back view.

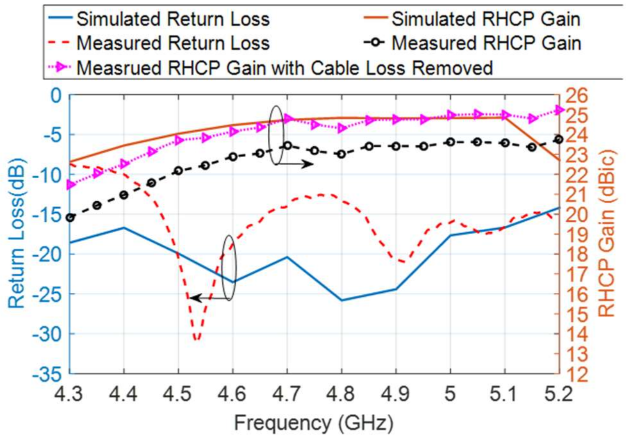

Figure 4.10. Measured and simulated return loss and RHCP gain of the 8×8 dual fed stacked patch antenna array with annular gaps.

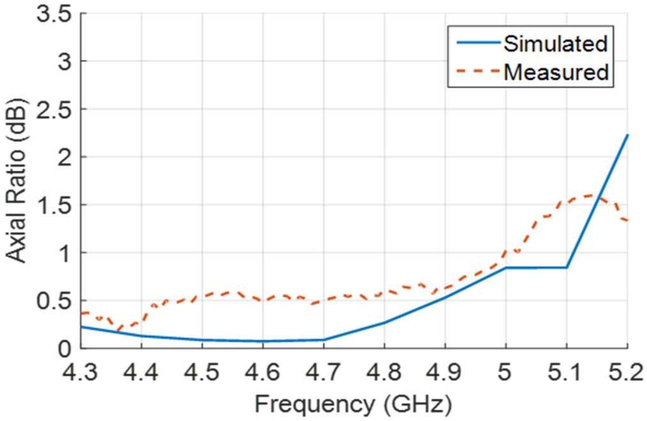

Figure 4.11. Measured and simulated axial ratio of the 8×8 dual fed stacked patch antenna array with annular gaps.

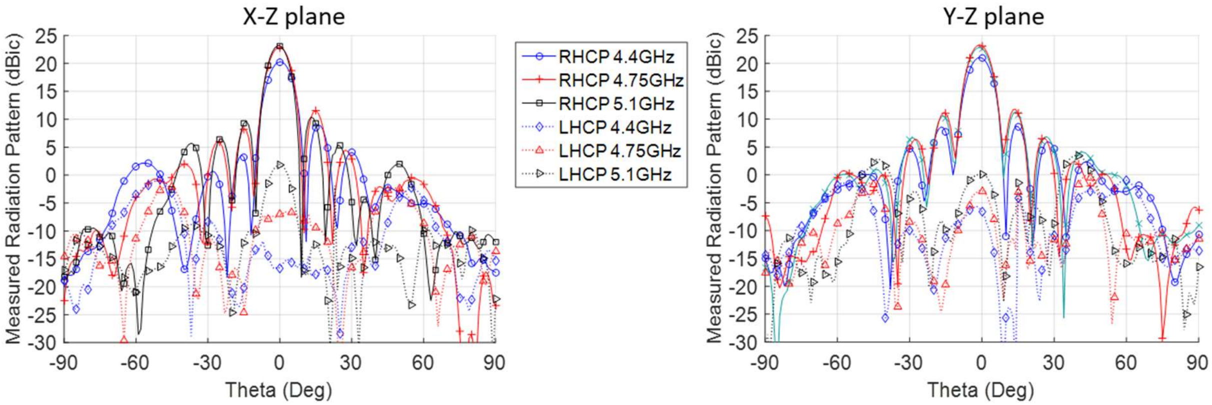

Figure 4.12. Measured radiation pattern of the 8×8 dual-fed stacked patch antenna array with annular gaps in the x-z plane and y-z plane.

Table 4.1. Comparison table of the measured radiation characteristics of the three antenna arrays in the broadside direction.

	4×8 LSA array	4×8 stacked patch antenna array	8×8 stacked patch antenna array
Frequency (GHz)	4–6	4.5–5	4.4–5.2
Bandwidth	40%	10.5%	16.7%
Gain (dBic)	15.5–18	17–19	21–23.7
Axial ratio (dB)	<1.8	<1	<1.6
3-dB beamwidth (x-z plane)	19°–13°	10°– 9°	10°– 9°
Side lobe level (dB)	<-14	<-10	<-10
Cross-polarization level (dB)	>20	>25	>25

4.2 Beam-Switching Radiation Characteristics

To characterize the beam-switching or beamforming performance of the antenna arrays, measurements were also conducted on the antenna arrays when fed by the 8×8 Butler matrix. Figure 4.13 shows the measured radiation patterns of the 4×8 LSA array in the x-z plane at 5 GHz. As shown in Figure 4.13a, at different input port of the Butler matrix, the main beam of the antenna array successfully steers to a different direction. The peak gain of the main beam decreases as it steers away from the broadside direction due to the nature of the antenna element. Stable beam patterns are obtained when the main beam direction is within ±30°, and the change in the peak gain is within 2.2 dB. For main beams within ±30° angle, the average peak gain is about 13.5 dBic with 3-dB beamwidth about 15°, side lobe level less than -13 dB and cross polarization level more than 10 dB. There is about 3 dB decrease in gain compare to the measured result in the broadside direction. The decreases in gain is due to the insertion loss of the Butler matrix. The corresponding axial ratio on the direction of each main beam is shown in Figure 4.13b. As it may be seen the axial ratio degrades as the main beam steers away from the broadside direction. For the beam patterns at ports 1 and 8, the axial ratio is less than 3 dB in the direction of the main beam. For the beam patterns at ports 4 and 5, the axial ratio increases to more than 3 dB as the angle increases. Overall the axial ratio is less than 6 dB within ±30° angle. The axial ratio for ports 2 and 7 is not shown in the figure as the axial ratio degrades to more than 10 dB.

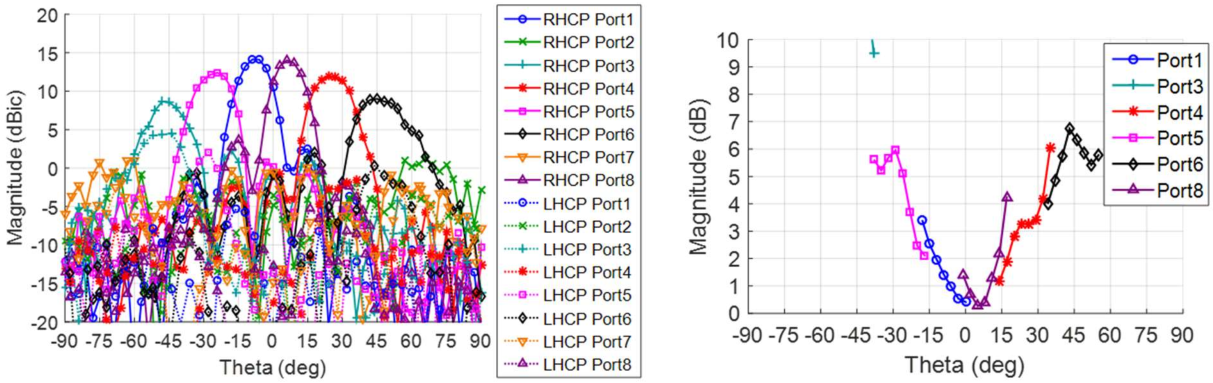

(a) (b)

Figure 4.13. Measured radiation characteristics of the 4×8 LSA array fed by the Butler matrix in the x-z plane at 5 GHz: (a) Radiation pattern. (b) Axial ratio.

The measured results at the lower and upper frequencies (4 and 6 GHz) of the 4×8 LSA array fed by the Butler matrix are shown in Figure 4.14 and Figure 4.15. At 4 GHz, each corresponding main beam steers to a slightly larger angle direction and has wider beamwidth, compared to the results at 5 GHz. This is because the feeding port spacing is smaller at 4 GHz in terms of wavelength. In this case, stable beam patterns are obtained when the main beam directions are within ±40°. The 3-dB beamwidth is about 17°. The average peak gain is about 12.5 dBic with cross polarization level more than 10 dB. The axial ratio is less than 4.5 dB when the main beam directions are within ±40°. Similarly, at 6 GHz, stable beam patterns are obtained when the main beam directions are within ±30°. The 3-dB beamwidth is about 13°. The average peak gain is about 13.5 dBic with cross polarization level more than 10 dB. The axial ratio is less than 6 dB when the main beam directions are within ±30°.

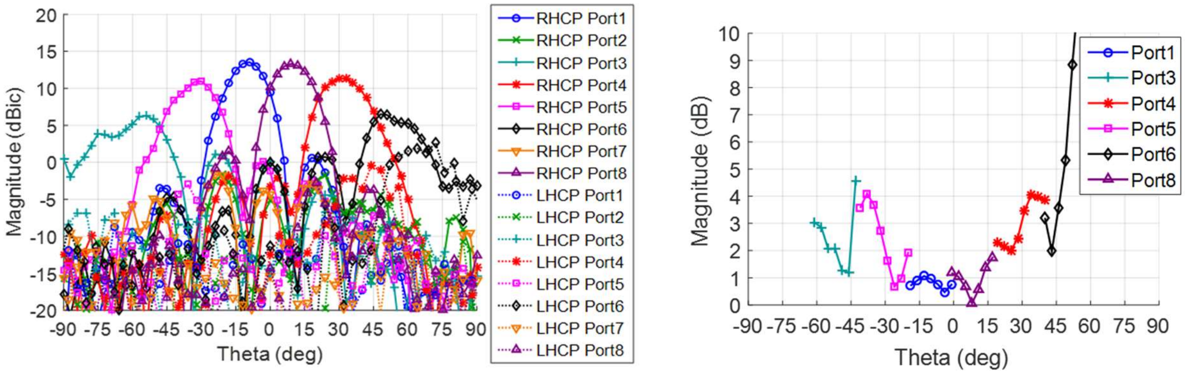

(a) (b)

Figure 4.14. Measured radiation characteristics of the 4×8 LSA array fed by the Butler matrix in the x-z plane at 4 GHz: (a) Radiation pattern. (b) Axial ratio.

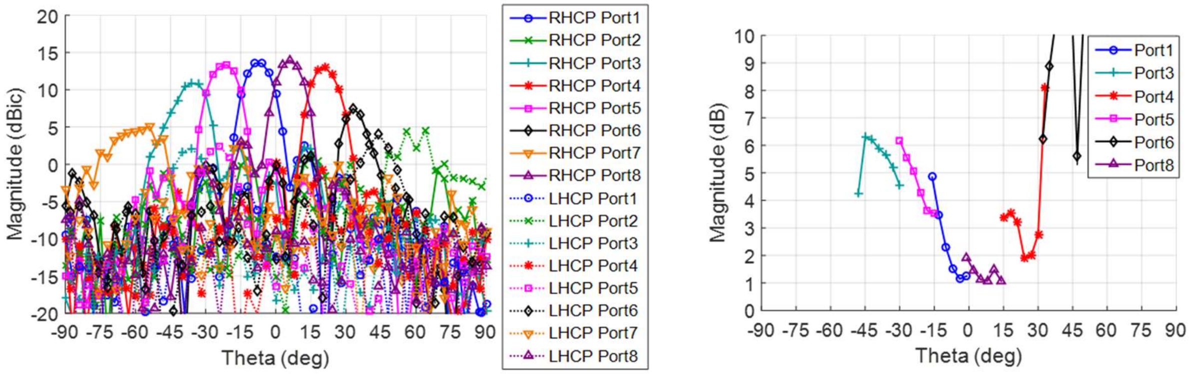

(a) (b)

Figure 4.15. Measured radiation characteristics of the 4×8 LSA array fed by the Butler matrix in the x-z plane at 6 GHz: (a) Radiation pattern. (b) Axial ratio.

Figure 4.16Figure 4.18 illustrate the measured radiation patterns and axial ratio of the 4×8 dual-fed stacked patch antenna array fed by the Butler matrix at different frequencies (center, lower and upper frequencies of the 4.5–5 GHz band). As the 4.5–5 GHz frequency span is not large, the radiation patterns at 4.5 GHz and 5 GHz are very similar and have 3-dB beamwidth of about 10° to 9°. Similar to the LSA array, stable beam patterns are also obtained in the angle range of ±30°. The patch antenna array has antenna element spacing of 0.66λ at 4.75 GHz. Hence, narrower beamwidth (10°) and closer main beam directions are obtained as expected. Grating lobes are also observed in the radiation patterns of ports 2 and 7 which the main beam of these patterns is outside of the ±30° angle range. The average peak gain of the measured radiation patterns is about 14.5 dBic with sidelobe level less than -10 dB and cross polarization level more than 13 dB. Similar to the LSA array, the axial ratio degrades as the main beam steers away from the broadside direction. Overall the axial ratio is less than 4.5 dB within ±30° angle, which is slightly better than the LSA array.

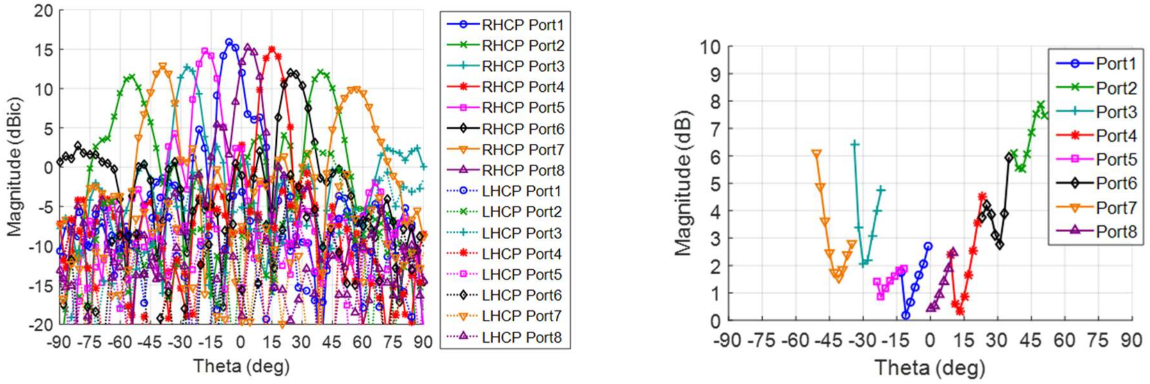

(a) (b)

Figure 4.16. Measured radiation characteristics of the 4×8 patch antenna array fed by the Butler matrix in the x-z plane at 4.75 GHz: (a) Radiation patterns. (b) Axial ratio.

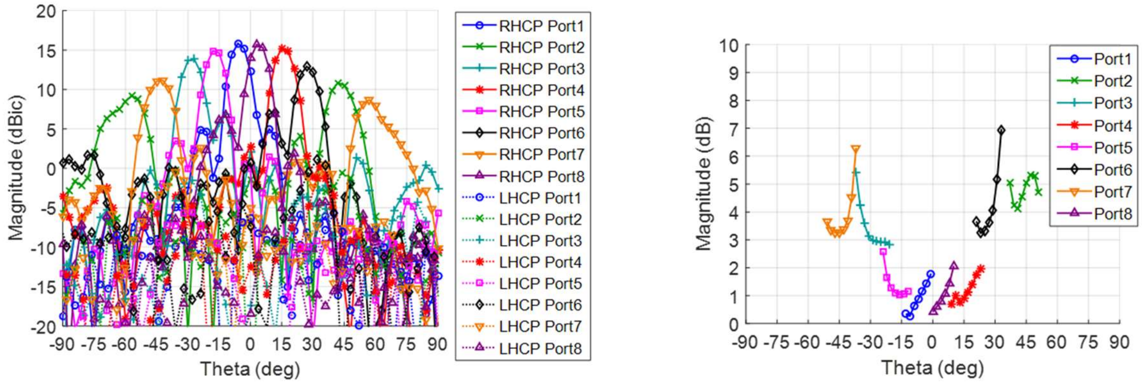

(a) (b)

Figure 4.17. Measured radiation characteristics of the 4×8 patch antenna array fed by the Butler matrix in the x-z plane at 4.5 GHz: (a) Radiation patterns. (b) Axial ratio.

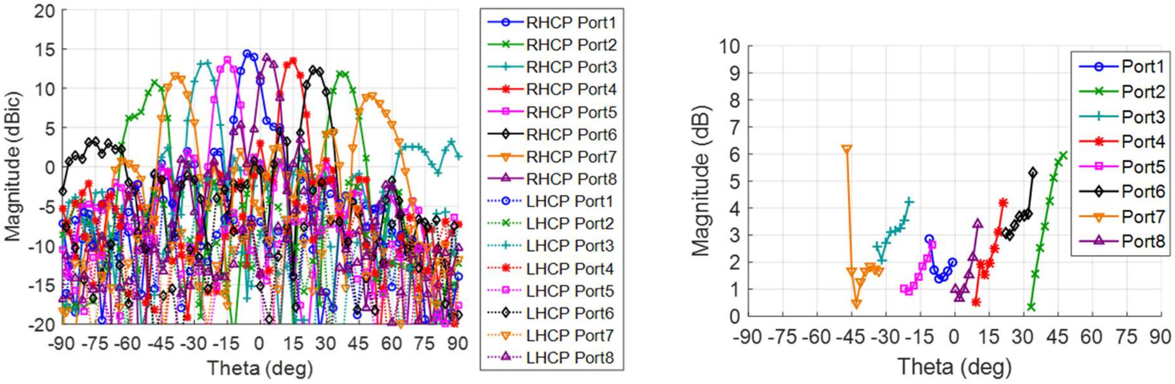

(a) (b)

Figure 4.18. Measured radiation characteristics of the 4×8 patch antenna array fed by the Butler matrix in the x-z plane at 5 GHz: (a) Radiation patterns. (b) Axial ratio.

The measured radiation patterns and axial ratio of the 8×8 patch antenna array with annular gaps fed by the Butler matrix at different frequencies are shown in Figure 4.19Figure 4.18. The beamwidth and beam directions of the 8×8 patch antenna array are the same as the 4×8 patch antenna array as their element spacing are the same. The 8×8 patch antenna array has higher average peak gain which is about 20 dBic. Grating lobes are also observed in the radiation patterns of ports 2 and 7. Similarly, stable beam patterns without grating lobes are obtained in the angle range of ±30°. The radiation patterns have sidelobe level less than -10 dB and cross polarization level more than 15 dB. Good axial ratio values are obtained for the radiation patterns within the ±30° angle range, where the axial ratio values are below 3 dB.

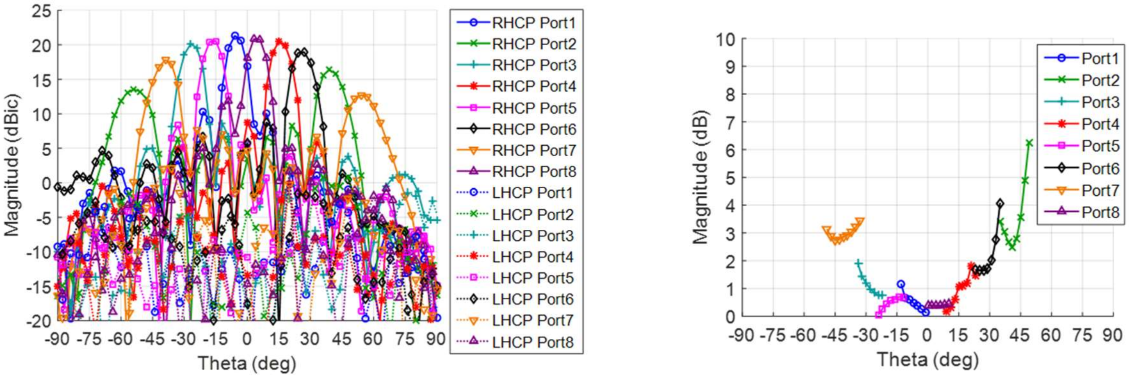

(a) (b)

Figure 4.19. Measured radiation characteristics of the 8×8 patch antenna array with annular gaps fed by the Butler matrix in the x-z plane at 4.75 GHz: (a) Radiation patterns. (b) Axial ratio.

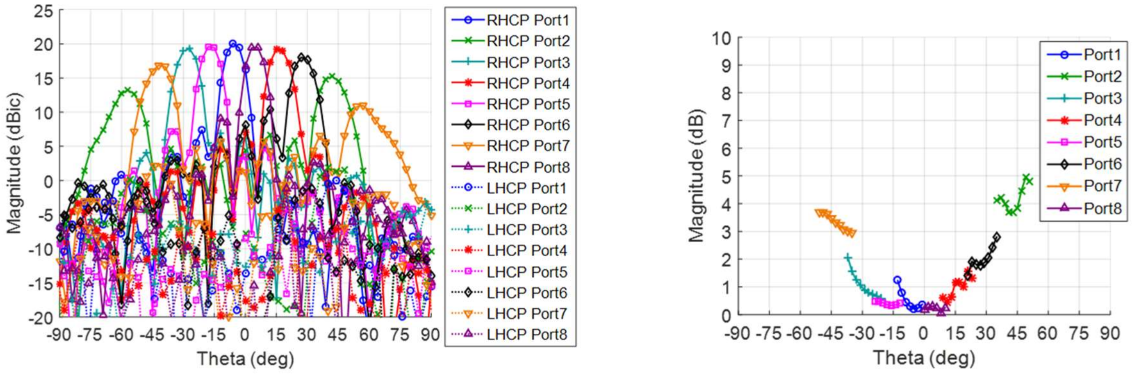

(a) (b)

Figure 4.20. Measured radiation characteristics of the 8×8 patch antenna array with annular gaps fed by the Butler matrix in the x-z plane at 4.5 GHz: (a) Radiation patterns. (b) Axial ratio.

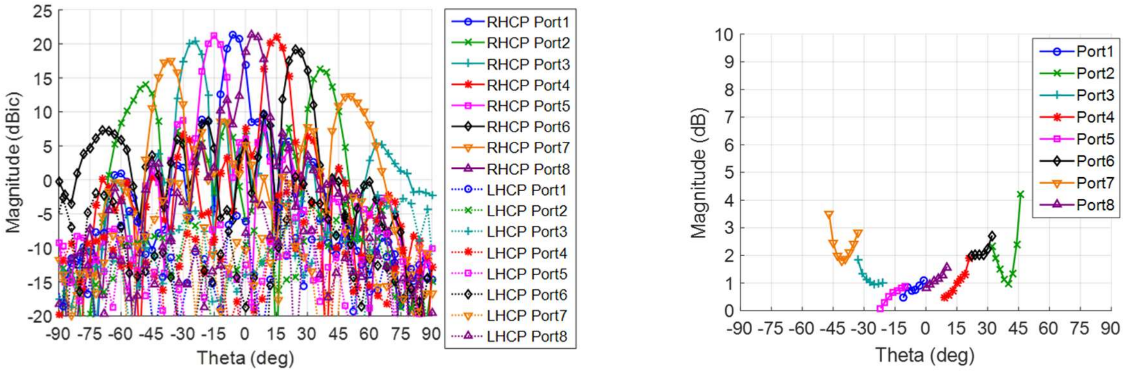

(a) (b)

Figure 4.21. Measured radiation characteristics of the 8×8 patch antenna array with annular gaps fed by the Butler matrix in the x-z plane at 5 GHz: (a) Radiation patterns. (b) Axial ratio.

Stable RHCP radiation patterns are obtained in the scanning range of ±30° on the three antenna arrays when fed by the Butler matrix. At the angles outside the ±30° range, the radiation patterns either degrade very fast or have grating lobes. With limited feeding port spacing, the 4×8 LSA array has wider beamwidth and only four stable main beams are observed covering the ±30° angle range. On the other hand, the patch antenna arrays have larger element spacing, which results in narrower beamwidth and six main beams are observed in the ±30° angle range. The 4×8 LSA array has average peak gain about 13.5 dBic when fed by the Butler matrix, while the 4×8 patch antenna array and the 8×8 patch antenna array have average peak gain about 14.5 dBic and 20 dBic, respectively. The axial ratio of the antenna arrays degrades while the main beam direction of the radiation pattern steer away from the broadside direction. Overall, in the scanning range of ±30°, the 4×8 LSA array has axial ratio of less than 6 dB while the 4×8 patch antenna array and the 8×8 patch antenna array have axial ratio of less than 4.5 dB and 3 dB, respectively. The patch antenna arrays have better axial ratio is due to the implementation of sequential rotation technique on the antenna elements in the antenna array design.

Table 4.2 shows the comparison of the three antenna arrays with other state-of-the-art publications on circularly polarized antenna array. Since most of the published works on circularly polarized antenna array are only focus on the radiation characteristics of the antenna array in the broadside direction and do not support beam-steering, Table 4.2 compares the radiation characteristics of the antenna arrays in the broadside direction. As the other published works have different number of antenna elements and sizes, the antenna arrays are also compared in terms of realized aperture usage rate (RAUR).

Table 4.2. Comparison table of the circularly polarized antenna arrays and other published designs.

Antenna array	Number of elements	Frequency (GHz)	Bandwidth	Gain (dBic)	Dimension	RAUR	Beam-steering
LSA array	4×8	4–6	40%	17	$4.2\lambda_c \times 2.6\lambda_c \times 0.2\lambda_c$	$5.15/\lambda_c^2$	Y
stacked patch antenna array	4×8	4.5–5	10.5%	18	$5.3\lambda_c \times 2.99\lambda_c \times 0.0475\lambda_c$	$4.47/\lambda_c^2$	Y
stacked patch antenna array with annular gaps	8×8	4.4–5.2	16.7%	23	$5.77\lambda_c \times 5.77\lambda_c \times 0.08\lambda_c$	$5.99/\lambda_c^2$	Y
[77]	1×4	2.434–2.474 3.13–3.17	1.6% 1.3%	10	$2.8\lambda_c \times 0.7\lambda_c \times 0.044\lambda_c$	$5.1/\lambda_c^2$	Y
[17]	1×4	4.4–5.75	26.7%	9	$2.45\lambda_c \times 0.85\lambda_c \times 0.118\lambda_c$	$3.8/\lambda_c^2$	Y
[78]	1×4	3.57–6.3	55.3%	13	$2.71\lambda_c \times 1.48\lambda_c \times 0.304\lambda_c$	$4.97/\lambda_c^2$	N
[19]	1×8	5.46–5.7	2.2%	13.5	$8.8\lambda_c \times 5.8\lambda_c \times 0.1\lambda_c$	$0.44/\lambda_c^2$	Y
[79]	2×2	1.1–1.77	46%	12	$1.91\lambda_c \times 1.91\lambda_c \times 0.31\lambda_c$	$4.34/\lambda_c^2$	N
[80]	4×4	6.585–6.65	1%	20	$4.08\lambda_c \times 3.8\lambda_c \times 0.035\lambda_c$	$6.45/\lambda_c^2$	N
[81]	4×4	56.55–65.13	14.1%	19	$5\lambda_c \times 5\lambda_c \times 0.32\lambda_c$	$3.18/\lambda_c^2$	N
[82]	8×8	28.1–29.8	5.9%	24	$6.15\lambda_c \times 6.15\lambda_c \times 0.024\lambda_c$	$6.64/\lambda_c^2$	N
[83]	8×8	10.7–12.3	14%	24	$7\lambda_c \times 7\lambda_c \times 0.082\lambda_c$	$5.13/\lambda_c^2$	N
[84]	8×16	12.01–12.14	1.1%	26	$6.04\lambda_c \times 11.96\lambda_c \times 0.1\lambda_c$	$5.51/\lambda_c^2$	N
[85]	12×12	7.25–8.4	14.7%	26	$10.4\lambda_c \times 10.4\lambda_c \times 0.159\lambda_c$	$3.68/\lambda_c^2$	N

RAUR is defined as antenna gain per wavelength square area. As shown in Table 4.2 the 4×8 LSA array and the 8×8 stacked patch antenna array have relatively wide bandwidth and high RAUR in comparison with other antenna arrays. For antenna arrays have similar RAUR as the LSA array and the patch antenna array, they are either have narrower bandwidth or lower gain. Such as the array designs in [77], [80], [82], and [84], the bandwidth of the antenna arrays are less than 6%. The antenna array in [78] has a bandwidth of 55% and a RAUR of about $5/\lambda_c^2$, which is comparable with the 4×8 LSA array, however, its gain is about 13 dB and does not support beam-steering. For other antenna array designs, which have relatively wide bandwidth, their RAUR tend to be low, such as the designs in [17] and [79]. Overall, the 4×8 LSA array and the 8×8 stacked patch antenna array have relatively high RAUR and low-profile in comparison with other antenna arrays have similar bandwidth. Note that the ground plane dimensions are not optimized when designing the LSA and the patch array, thus, the RAUR of the arrays can be further improved by reducing the size of the antenna ground plane.

CHAPTER 5

CONCLUSIONS AND FUTURE WORK

Two novel right hand circularly polarized antenna arrays were developed for directional networking application and the antenna arrays are designed to meet sponsor requirement for the US Army CERDEC. For the 4×8 LSA array, small diagonal slots were created on the metallic patches of the antenna array to reduce the input impedance of the antenna array. The small diagonal slots were able to reduce the input impedance of the LSA array to 60 Ω, thus the complicated impedance transformers are no longer required to feed the LSA array and it can be fed by simple tapered microstrip transmission lines. The new 4×8 LSA array design covers the frequency band of 4–6 GHz with gain of 17 dBic, axial ratio of <1.8 dB and 3-dB beamwidth of 19°–13°. For systems require extremely low-profile antenna installation, two patch antenna arrays were designed. The 4×8 stacked patch antenna array was designed using substrate material with dielectric constant of 3.55 and thickness of 1.523 mm, it covers the frequency band of 4.5–5 GHz with gain of 18 dBic, axial ratio of < 1dB and 3-dB beamwidth of 10°. To improve the gain of the patch antenna array, a substrate with low dielectric constant (ε_r=2.64) was used and air gaps in between the substrate and the ground plane were introduced to lower the effective dielectric constant. However, the extra height from the air gap introduce extra inductance on the feeding probes of the antenna. Thus, annular gaps were used to compensate the extra inductance. With doubling of the antenna elements, the new 8×8 stacked patch antenna array has a gain of 23 dBic, an axial ratio of < 1.6 dB and a 3-dB beamwidth of 10°, and it covers the frequency band of 4.4–5.2 GHz.

To steer the main beam of the antennas, an 8×8 compact broadband single layer Butler matrix was designed. A compact coplanar waveguide crossover design was implemented in the Butler matrix design to reduce the size of the Butler matrix. The developed Butler matrix operates at the frequency band of 4–6 GHz; it has insertion loss of 3±2 dB and phase shift error of ±20°. Measurements were performed on the antenna arrays when fed by the Butler matrix to characterize the beam steering performance of the antenna arrays. The Butler matrix was able to steer the main beam of the antenna array to different directions in the azimuth plane. Stable RHCP radiation patterns are obtained in the scanning range of ±30° on the three antenna arrays when fed by the Butler matrix. The axial ratio of the antenna arrays degrades while the main beam direction of the radiation pattern steer away from the broadside direction. In the measured results, the 4×8 LSA array has wider beamwidth and four stable main beams are observed covering the ±30° scanning angle with average peak gain of about 13.5 dBic and axial ratio of less than 6 dB. On the other hand, the patch antenna arrays have narrower beamwidth and six main beams are observed in the ±30° scanning angle due to the patch arrays have larger element spacing. The 4×8 patch antenna array has average peak gain about 14.5 dBic and axial ratio less than 4.5 dB. The 8×8 patch antenna array has average peak gain about 20 dBic and axial ratio less than 3 dB.

Future work will include development of user discovery and tracking schemes that support multiple users and are compatible with the communication protocol (WiFi or LTE) that will be used in the proposed directional networking system. The tracking schemes and codes will be implemented in a FPGA or microprocessor control unit. As for the beamforming, we will continue to explore the tradeoffs involved in either analog implementation (e.g. using Butler matrix) vs digital implementations. Butler matrix based implementation is a low-cost option, hence attractive for rural area implementation and also requires only one feed and a set of switches for controlling the beam direction. Digital beamforming implementation, on the other hand requires multiple feeds but has the advantage of flexibility in beamforming options such as the generation of multiple simultaneous beams and adaptive beamforming. The final stage for the whole project will be field testing of the proposed directional networking system in rural areas.

Reference

[1] T. Wheeler, M. Clyburn, J. Rosenworcel, A. Pai, and M. O'Rielly, "2015 Broadband Progress Report and Notice of Inquiry on Immediate Action to Accelerate Deployment," Federal Communications Commission, pp. 14–126, Feb. 2015.

[2] E. Dahlman, S. Parkvall, and J. Skold, *4G: LTE/LTE-Advanced for Mobile Broadband*. Waltham, Massachusetts: Academic press, 2014.

[3] Z. H. Talukder, S. S. Islam, D. Mahjabeen, A. Ahmed, S. Rafique, and M. A. Rashid, "Cell coverage evaluation for LTE and WiMAX in wireless communication system," *World Applied Sciences Journal*, vol. 22, no. 10, pp. 1486–1491, 2013.

[4] "Telstra mobile phone tower". Internet: https://commons.wikimedia.org/wiki/File:Telstra_Mobile_Phone_Tower.jpg, Feb. 18, 2006 [Oct. 29, 2017].

[5] C. Meagher, R. Olsen, C. Cirullo, R.C. Ferro, N. Stevens, and J. Yu, "Directional Ad Hoc Networking Technology (DANTE) Performance at Sea," *IEEE Military Communications Conf*erence, 2011, pp. 951–955.

[6] M. F. Iskander, Z. Yun, F. A. Qazi, G. Sasaki, A. Das, "Physical layer based approach for advanced directional networking," *IEEE Military Communications (MILCOM) Conference*, 2016, pp. 224–229.

[7] J. Niu, R. Zhang, L. Cai, and J. Yuan, "A fully-distributed directional-to-directional MAC protocol for mobile ad hoc network," *2015 International Conference on Computing, Networking and Communications (ICNC),* Garden Grove, CA, 2015, pp. 766–770.

[8] R. Ramanathan, J. Redi, C. Santivanez, D. Wiggins, and S. Polit, "Ad hoc networking with directional antennas complete system solution," *IEEE Journal on Selected Areas in Communications,* vol. 23, no. 3, Mar 2005.

[9] P. Li, H. Zhai, and Y. Fang, "SDMAC: selective directional MAC protocol for wireless mobile ad hoc network," *Wireless Network*, vol. 15, no. 6, pp. 805–820, Oct, 2009.

[10] C. Cirullo, "A prototype system for using multiple radios in directional MANET (Mobile Ad Hoc Networks): a NISE funded applied research project," No. SPAWAR-SCP-TD-3276, 2013.

[11] G. C. Huang, M. F. Iskander, and M. Hoque, "Advanced antenna array designs for directional networks," *IEEE Military Communication (MILCOM) Conference*, 2016, pp. 204–207.

[12] “IEEE Standard Definitions of Terms for Antennas,” IEEE Std 145-1993, July 18 1993.

[13] C. A. Balanis, Antenna Theory Analysis and Design, 3rd ed. Hoboken, NJ: John Wiley & Sons, Inc., 2005.

[14] Internet: https://i.ytimg.com/vi/Q0qrU4nprB0/maxresdefault.jpg, [Jan. 25, 2018].

[15] Internet: http://www.antennamagus.com/database/antennas/antenna_page.php?id=259, [Feb. 1, 2018].

[16] “Horn Antennas.” Internet: https://www.everythingrf.com/search/waveguide-horn-antennas, [Feb. 1, 2018].

[17] C. Liu, S. Xiao, Y. Guo, Y. Bai, and B. Wang, “Broadband circularly polarized beam-steering antenna array,” *IEEE Transactions on Antennas and Propagation*, vol. 61, no. 3, pp. 1475–1479, Mar. 2013.

[18] J. Ouyang, “A circularly polarized switched-beam antenna array,” *IEEE Antennas and Wireless Propagation Letters*, vol. 10, pp. 1325–1328, 2001.

[19] Y. Wen, B. Wang, and X. Ding, “Wide-beam circularly polarized microstrip magnetic-electric dipole antenna for wide-angle scanning phased array,” *IEEE Antennas and Wireless Propagation Letters*, vol. 16, pp. 428–431, 2017.

[20] J. Baik, T. Lee, S. Pyo, S. Han, J. Jeong, and Y. Kim, "Broadband circularly polarized crossed dipole with parasitic loop resonators and its arrays," *IEEE Transactions on Antennas and Propagation*, vol. 59, no. 1, pp. 80–88, 2011.

[21] Y. Hu, W. Ding, and W. Cao, “Broadband circularly polarized microstrip antenna array using sequentially rotated technique,” *IEEE Antennas and Wireless Propagation Letters*, vol. 10, pp. 1358–1361, 2011.

[22] V. Rafii, J. Nourinia, C. Ghobadi, J. Pourahmadazar, and B. S. Virdee, “Broadband circularly polarized slot antenna array using sequentially rotated technique for C-band applications,” *IEEE Antennas and Wireless Propagation Letters*, vol. 12, pp. 128–131, 2013.

[23] S. Yang, R. Chair, A. Kishk, K. Lee, and K. Luk, “Study on sequential feeding networks for subarrays of circularly polarized elliptical dielectric resonator antenna,” *IEEE Transactions on Antennas and Propagation*, vol. 55, no. 2, pp. 321–333, Feb. 2007.

[24] Y. Hu, Z. Qiu, B. Yang, S. Shi, and J. Yang, “Design of novel wideband circularly polarized antenna based on Vivaldi antenna structure,” *IEEE Antennas and Wireless Propagation Lett*ers, vol. 14, pp. 1662–1665, 2015.

[25] J. Yan, S. Gogineni, B. Camps-Raga, and J. Brozena, “A dual-polarized 2–18 GHz Vivaldi array for airborne radar measurements of snow,” *IEEE Transactions on Antennas and Propagation*, vol. 64, no. 2, pp. 781–785, Feb. 2016.

[26] C. Liu, Y. Lu, C. Du, J. Cui, and X. Shen, “The broadband spiral antenna design based on hybrid backed-cavity,” *IEEE Transactions on Antennas and Propagation*, vol. 58, no. 6, pp. 1876–1882, Jun. 2010.

[27] M. Serhir and R. Guinvarc, “Low-profile cavity-backed dual-polarized spiral antenna array,” *IEEE Antennas and Wireless Propagation Letters*, vol. 12, pp. 524–527, 2013.

[28] H.S. Youn, L. Lee, N. Celik, and M. Iskander, “Dual-polarization cylindrical long-slot array antenna integrated with hybrid groundplane,” in *IEEE Antennas Propagation Society International Symposium*., Chicago, IL, 2012.

[29] J. Rayno, N. Celik, M.F. Iskander, "Dual-polarization cylindrical long-slot array (CLSA) antenna integrated with compact broadband baluns and slot impedance transformers," *IEEE Antennas and Wireless Propagation Letters*, vol.12, pp.1384–1387, 2013.

[30] H.S. Youn, Y.L. Lee, N. Celik, and M.F. Iskander, “Design of a cylindrical long-slot array antenna integrated with hybrid EBG/ferrite ground plane,” *IEEE Antennas and Wireless Propagation Letters*, vol. 11, pp. 180–183, 2012.

[31] L. Y. Lee, H. Youn, and M. F. Iskander, “Long slot array (LSA) antenna integrated with compact broadband coupled microstrip impedance transformer,” in *IEEE Antennas and Propagation Society International Symposium,* Chicago, IL, 2012.

[32] A. Neto and J. J. Lee, “Ultrawide-band properties of long-slot arrays,” *IEEE Trans. Antennas Propag*., vol. 54, no. 2, pp. 534–543, Feb. 2006.

[33] J. J. Lee, S. Livingston, and D. Nagata, “A low profile 10:1 (200-2000 MHz) wide band long slot array,” *IEEE Antennas and Propagation Society International Symposium*, San Diego, CA, 2008.

[34] G. C. Huang, M. F. Iskander, M. Hoque, S. Goodall, T. Bocskor, “Antenna array design and system for directional networking,” *IEEE Antennas and Wireless Propagation Letters,* vol. 14, PP. 1141–1144, Feb. 2015.

[35] G. C. Huang, M. F. Iskander, Z. Zhang, “Circularly polarized beam-switching antenna array design for directional networks,” *IEEE Antennas and Wireless Propagation Letters*, vol. 17, no. 4, pp. 604-607, Apr. 2018.

[36] G. C. Huang, M. F. Iskander, F. A. Qazi, Z. Yun and G. H. Sasaki, “Antenna arrays for physical layer-based directional networking technology,” in The World of Applied Electromagnetics, A. Lakhtakia and C. M. Furse Ed. Springer International Publishing, 2017, pp. 107-132.

[37] D. M. Pozar. *Microwave Engineering, 4th ed*. John Wiley & Sons, Inc., 2011.

[38] C. Lin, S. Chang, C. Chang, Y. Shu, "Design of a reflection-type phase shifter with wide relative phase shift and constant insertion loss," *IEEE Transactions on Microwave Theory and Techniques*, vol. 55, no. 9, pp. 1862-1868, Sep. 2007.

[39] J. Huang. "Microstrip antennas: analysis, design, and application" in *Modern Antenna Handbook*, C. A. Balanis, Ed. John Wiley & Sons, Inc., 2008, pp. 157–200.

[40] K. Yang and K. Wong, "Dual-band circularly-polarized square microstrip antenna *IEEE Transactions on Antennas and Propagation*, vol. 49, no. 3, pp. 377–382, Mar. 2001.

[41] H. Kim, B. M. Lee, and Y. J. Yoon, "A single-feeding circularly polarized microstrip antenna with the effect of hybrid feeding," *IEEE Antennas and Wireless Propagation Letters*, vol. 2, pp. 74-77, 2003.

[42] K. F. Tong and T. P. Wong, "Circularly polarized U-Slot antenna," *IEEE Transactions on Antennas and Propagation*, vol. 55, no. 8, pp. 2382–85, Aug. 2007.

[43] H. L. Chung, X. Qing, and Z. Ning, "Broadband circularly polarized stacked patch antenna for UHF RFID applications," *IEEE Antennas and Propagation Society International Symposium*, Hon. HI, Jun, 2007, pp. 1189–1192.

[44] Z. N. Chen, X. Qing, and H. L. Chung, "A universal UHF RFID reader antenna," *IEEE Transactions on Microwave Theory and Techniques*, vol. 57, no. 5, pp. 1275–1282, May 2009.

[45] G. C. Huang, M. F. Iskander, and M. Hoque, "A wideband circularly polarized stacked patch antenna array and feed system," *IEEE International Conference on Wireless Information Technology and Systems (ICWITS) and Applied Computational Electromagnetics* (ACES), Honolulu, HI, 2016.

[46] J. S. Colburn and Y. Rahmat-Samii, "Patch antennas on externally perforated high dielectric constant substrates," *IEEE Transactions on Antennas and Propagation*, vol. 47, no. 12, pp. 1785–1794, Dec. 1999.

[47] H. Boutayeb and T. A. Denidni, "Gain enhancement of a microstrip patch antenna using a cylindrical electromagnetic crystal substrate," *IEEE Transactions on Antennas and Propagation*, vol. 55, no. 11, pp. 3140–3145, Nov. 2007.

[48] R. Gonzalo, P. De Maagt, and M. Sorolla, "Enhanced patch-antenna performance by suppressing surface waves using photonic-bandgap substrates," *IEEE Transactions on Microwave Theory and Techniques*, vol. 47, no. 11, pp. 2131–2138, Nov. 1999.

[49] H.S. Lee, J.-G. Kim, S. Hong, and J.-B. Yoon, “Micromachined CPW-fed suspended patch antenna for 77 GHz automotive radar applications,” *The European Conference on Wireless Technology,* pp. 269–272, 2005.

[50] J. M. Kovitz and Y. Rahmat-Samii, “Using thick substrates and capacitive probe compensation to enhance the bandwidth of traditional CP patch antennas,” *IEEE Transactions on Antennas and Propagation*, vol. 62, no. 10, pp. 4970–4979, Oct. 2014.

[51] Z. Wang, S. Fang, S. Fu, and S. Jia, “Single-fed broadband circularly polarized stacked patch antenna with horizontally meandered strip for universal UHF RFID applications,” *IEEE Transactions on Microwave Theory and Techniques*, vol. 59, no. 4, pp. 1066–1073, Apr. 2011.

[52] C. Zhang, X. Liang, X. Bai, J. Geng, and R. Jin, “A broadband dual circularly polarized patch antenna with wide beamwidth,” *IEEE Antennas and Wireless Propagation Letters*, vol. 13, pp. 1457–1460, Jul. 2014.

[53] S. Fu, Q. Kong, S. Fang, and Z. Wang, “Broadband circularly polarized microstrip antenna with coplanar parasitic ring slot patch for L-band satellite system application,” *IEEE Antennas and Wireless Propagation Letters*, vol. 13, pp. 943–946, May 2014.

[54] M. He, X. Ye, P. Zhou, G. Zhao, C. Zhang, and H. Sun, “A small-size dual-feed broadband circularly polarized U-slot patch antenna,” *IEEE Antennas and Wireless Propagation Letters*, vol. 14, pp. 898–901, Dec. 2014.

[55] J. Zhuang, Y. Zhang, W. Hong, and Z. Hao, “A broadband circularly polarized patch antenna with improved axial ratio,” *IEEE Antennas and Wireless Propagation Letters*, vol. 14, pp. 1180–1183, Jan. 2015.

[56] K. L. Lau and K. M. Luk, “A novel wide-band circularly polarized patch antenna based on L-probe and aperture-coupling techniques,” *IEEE Transactions on Antennas and Propagation*, vol. 53, no. 1, pp. 577–580, Jan. 2005.

[57] W. Yang, J. Zhou, Z. Yu, and L. Li, “Single-fed low profile broadband circularly polarized stacked patch antenna,” *IEEE Transactions on Antennas and Propagation*, vol. 62, no. 10, pp. 5406–5410, Jul. 2014.

[58] J. Wu, Y. Yin, Z. Wang, and R. Lian, “Broadband circularly polarized patch antenna with parasitic strips,” *IEEE Antennas and Wireless Propagation Letters*, vol. 14, pp. 559–562, Nov. 2014.

[59] M. F. Iskander. *Electromagnetic Fields and Waves, 2nd ed.* Waveland Press, Inc., 2012.

[60] P. K. Singhal, P. C. Sharma, R. D. Gupta, “Rotman lens with equal height of array and feed contours,” *IEEE Transactions on Antennas and Propagation*, vol. 51, no. 8, Aug. 2003.

[61] C. C. Chang, R. H. Lee, and T. Y. Shih, “Design of a beam switching/steering Butler matrix for phased array system,” *IEEE Transactions on Antennas and Propagation*, vol. 58, no. 2, Fed. 2010.

[62] H. Nachouane, A. Najid, A. Tribak, and F. Riouch, “Broadband 4×4 Butler matrix using wideband 90° hybrid couplers and crossovers for beamforming networks,” *International Conference on Multimedia Computing and Systems (ICMCS)*, Marrakech, 2014, pp. 1444-1448.

[63] C. Guclu, J. Perruisseau-Carrier, and O. Civi, “Proof of concept of a dual-band circularly-polarized RF MEMS beam-switching reflectarray,” *IEEE Transactions on Antennas and Propagation,* vol. 60, no. 11, pp. 5451-5455, Nov. 2012.

[64] L. Palma, A. Clemente, L. Dussopt, R. Sauleau, P Potier, and P. Pouliguen, “Circularly-polarized reconfigurable transmitarray in Ka-band with beam scanning and polarization switching capabilities,” *IEEE Transactions on Antennas and Propagation*, vol. 65, no. 2, pp. 529-540, Feb. 2017.

[65] G. C. Huang, M. F. Iskander, M. Hoque, S. R. Goodal, and T. Bocskor, “Implementation of high performance and broadband crossover junction in butler matrix design,” *IEEE Antennas and Propagation Society International Symposium (APSURSI),* pp. 1052–1053, July 2015.

[66] M. Muraguchi, T. Yukitake, and Y. Naito, “Optimum design of 3-dB branch-line couplers using microstrip lines,” *IEEE Transactions on Microwave Theory and Techniques*, vol. 31, no. 8, pp. 674–678, Aug. 1983.

[67] W. Liu, Z. Zhang, Z. Feng, and M. F. Iskander, “A compact wideband microstrip crossover,” *IEEE Microwave and Wireless Components Letters,* vol. 22, no. 5, pp. 254–256, May 2012.

[68] B. C. Wadell. *Transmission Line Design Handbook*. Artech House, Inc., 1991.

[69] I. Wolff. *Coplanar Microwave Integrated Circuits*. NJ: John Wiley & Sons, Inc., 2006.

[70] Z. Zhang, Y.-C. Jiao, S.-F. Cao, X.-M. Wang, and F.-S. Zhang, “Modified broadband Schiffman phase shifter using dentate microstrip and patterned ground plane,” *Progress in Electromagnetics Research Letters*, vol. 24, pp. 9–16, 2011.

[71] B. Schiek and J. Kohler, “A method for broad-band matching of microstrip differential phase shifters,” *IEEE Transactions on Microwave Theory and Techniques*, vol. 25, no. 8, pp. 666–671, Aug. 1977.

[72] R. J. Mailloux. *Phased Array Antenna Handbook, 2nd ed*. Artech House, Inc., 2005.

[73] G. T. Abreu and R. Kohno, “A modified Dolph-Chebyshev approach for the synthesis of low sidelobe beampatterns with adjustable beamwidth,” *IEEE Transactions on Antennas and Propagation*, vol. 51, no. 10, pp. 3014–3017, Oct. 2003.

[74] N. Celik. “High performance hybrid smart antenna array for advanced wireless communication applications.” PhD. Dissertation, University of Hawaii at Manoa, USA, 2009.

[75] R. S. Yeduri, R. R. Kumari, and C. K. Kumari, “Robust direction of arrival estimation using multiple signal analysis,” *International Journal of Computer Applications*, vol. 101, no. 11, pp. 17–21, 2014.

[76] C. T. Rodenbeck, K. Chang, and J. Aubin, “Automated pattern measurement for circularly-polarized antennas using the phase-amplitude method,” *Microwave Journal*, vol. 47, no. 7, pp. 68–78, 2004.

[77] M. Maqsood, S. Gao, T. W. C. Brown, M. Unwin, R. de vos Van Steenwijk, J. D. Xu, and C. I. Underwood, “Low-cost dual-band circularly polarized switched-beam array for global navigation satellite system,” *IEEE Transactions on Antennas and Propagation*, vol. 62, no. 4, pp. 1975–1982, April 2014.

[78] L. Zhang, S. Gao, Q. Luo, P. R. Young, W. Li, and Q. Li, “Inverted-S antenna with wideband circular polarization and wide axial ratio beamwidth,” *IEEE Transactions on Antennas and Propagation*, vol. 65, no. 4, pp. 1740–1748, April 2017.

[79] Z. Zhang, S. Zuo, Y. Zhao, L. Ji, and G. Fu, “Broadband circularly polarized bowtie antenna array using sequentially rotated technique,” *IEEE Access*, vol. 6, pp. 12769–12774, Feb. 2018.

[80] Z. C. Hao, X. Liu, X. Huo, and K. K. Fan, “Planar high-gain circularly polarized element antenna for array applications,” *IEEE Transactions on Antennas and Propagation*, vol. 63, no. 5, pp. 1937–1948, May 2015.

[81] Q. Zhu, K. B. Ng and C. H. Chan, “Printed circularly polarized spiral antenna array for millimeter-wave applications,” *IEEE Transactions on Antennas and Propagation,* vol. 65, no. 2, pp. 636–643, Feb. 2017.

[82] Y. Zhang, A. Chen, S. Cao, and D. Su, “Design of a circularly polarized 8×8 patch antenna array using a new series-parallel feed,” *IEEE International Symposium on Microwave, Antenna, Propagation and EMC Technologies for Wireless Communications*, Beijing, 2009, pp. 411–414.

[83] K. H. Lu and T. Chang, “Circularly polarized array antenna with corporate-feed network and series-feed elements,” *IEEE Transactions on Antennas and Propagation,* vol. 53, no. 10, pp. 3288–3292, Oct. 2005.

[84] J. Huang, F. Qiu, W. Lin, Z. Tang, D. Lei, M. Yao, Q. Chu, and Y. Guo, “A new compact and high gain circularly-polarized slot antenna array for Ku-band mobile satellite TV reception,” *IEEE Access*, vol. 5, pp. 6707–6714, 2017.

[85] A. Garcia-Aguilar, J. M. Inclan-Alonso, L. Vigil-Herrero, J. M. Fernandez-Gonzalez, and M. Sierra-Perez, “Low-profile dual circularly polarized antenna array for satellite communications in the X band,” *IEEE Transactions on Antennas and Propagation*, vol. 60, no. 5, pp. 2276–2284, May 2012.